
Deflection of wind turbine wakes by yaw misalignment - Simulation and field testing

Marc Bromm

Bei der Fakultät für Mathematik und Naturwissenschaften
der Carl von Ossietzky Universität Oldenburg
zur Erlangung des Grades und Titels eines

DOKTORS DER INGENIEURWISSENSCHAFTEN

DR.-ING.

angenommene Dissertation

von Herrn Marc Bromm

geboren in Cottbus



Gutachter: Prof. Dr. Martin Kühn
Zweitgutachter: Prof. Lucy Y. Pao, Ph.D.
Tag der Disputation: 04.07.2019

Abstract

In recent years, wind farm control has gained more and more attention in the wind energy community. Its primary objective is to mitigate the negative effects of the aerodynamic interactions between turbines, which can lead to reduced power yields and to increased structural loadings. Typically, the investigated control concepts are based on an integrated approach in which the operation of multiple wind turbines is optimised altogether instead of each turbine individually.

One promising method is the deflection of the wake of an upstream wind turbine by deliberately introducing an offset between the inflow direction and its yaw orientation, aiming at generating more favourable inflow conditions for the downstream turbines. In the scope of this thesis, field experiments at a multi-megawatt wind turbine and numerical simulations were performed to improve the understanding of the potential of wake deflection through yaw misalignment and to determine the requirements for a successful and robust application of the method at utility-scale wind turbines.

Based on the measurement data from the field campaigns we prove that in neutrally stratified boundary layers, wake trajectories can be systematically deflected with respect to the 10-minute-average of the overall hub height inflow direction. Due to the complex and highly dynamic ambient conditions in the field, the development of a state-of-the-art methodology for the experimental validation was required.

In the further course of this thesis, numerical simulations are used to analyse how the application of wake deflection affects the power yield and loading of turbines in two exemplary wind farms. As large-eddy simulations are not yet feasible for comprehensive investigations that involve a large number of individual simulations due to high computational demands, a sequential approach of large-eddy simulations and aeroelastic simulations was developed. For the given setups, it is shown that the application of wake deflection increases the power output of the wind farms. With regard to the fatigue loads, a more complex picture emerges as different load sensors partly exhibit opposing behaviour. Additional investigations are therefore recommended in order to better understand the consequences for an optimisation of the wind farm operation

and the trade-off between power yield and loads.

Further large-eddy simulations were used to determine how directionally sheared inflow influences the wake development of a wind turbine. Such conditions typically occur in stably stratified boundary layers, which are highly interesting for the application of wake deflection because of strong, persistent wakes and a low directional variability of the inflow. It is shown that directional shear results in non-symmetrical skewed wakes with an ellipse-like cross section. In most of the existing wake models, wakes are still considered to be rotationally symmetrical. Depending on the ambient conditions, inaccurate predictions might be the result.

With this study on various aspects of wake deflection, including its successful demonstration in the field, important steps towards a future utilisation of the method were taken. In further investigations, it is now important to assess to what extent wake deflection can be used economically viably in real wind farms to increase the overall power yield while keeping the induced fatigue loads within the design envelope.

Kurzfassung

In den letzten Jahren hat die Windparkregelung in der Windenergiegemeinschaft immer mehr an Bedeutung gewonnen. Vorrangiges Ziel ist es, die negativen Auswirkungen der aerodynamischen Wechselwirkungen zwischen den Windenergieanlagen, welche zu geringen Erträgen und zu erhöhten Lasten führen können, zu reduzieren. Typischerweise basieren die untersuchten Regelungskonzepte auf einem integrierten Ansatz, bei dem der Betrieb mehrerer Windenergieanlagen insgesamt optimiert wird, anstatt für jede Anlage einzeln.

Eine vielversprechende Methode ist die Ablenkung des Nachlaufs von Windenergieanlagen durch das bewusste Herbeiführen eines Versatzes zwischen der Anströmrichtung und der Gierausrichtung, wodurch günstigere Anströmbedingungen für stromabwärts positionierte Anlagen erzielt werden sollen.

Im Rahmen dieser Arbeit wurden Feldversuche an einer Multi-Megawatt-Windenergieanlage und numerische Simulationen durchgeführt, um ein besseres Verständnis für das Potential der Nachlaufablenkung zu entwickeln und um die Anforderungen für eine erfolgreiche und zuverlässige Anwendung der Methode an realen Windenergieanlagen zu verstehen.

Basierend auf den Messdaten aus den Freifeldkampagnen wird gezeigt, dass in neutral geschichteten Grenzschichten, Nachlauftrajektorien in Bezug auf das 10-Minuten-Mittel der Anströmrichtung auf Nabenhöhe systematisch abgelenkt werden können. Aufgrund der komplexen und hochdynamischen Umgebungsbedingungen im Feld war die Entwicklung einer modernen Methodik für die experimentelle Validierung erforderlich.

Im weiteren Verlauf dieser Arbeit werden numerische Simulationen verwendet, um zu analysieren, wie sich die Anwendung der Nachlaufablenkung auf den Leistungsertrag und die Belastung von Anlagen in zwei exemplarischen Windparks auswirkt. Da Large Eddy Simulationen, aufgrund hoher Rechenanforderungen, für eine umfassende Untersuchung einer Vielzahl von Bedingungen noch nicht geeignet sind, wurde ein sequentieller Ansatz von Large Eddy Simulationen und aeroelastischen Simulationen entwickelt. Für die untersuchten Fälle konnte durch die Anwendung der Nachlaufablenkung eine Erhöhung des Energieertrages der Windparks erzielt werden.

Bei den Ermüdungslasten ergibt sich ein komplexeres Bild, da verschiedene Lastsensoren teilweise entgegengesetzte Charakteristiken aufweisen. Um die Auswirkungen auf die Optimierung des Windparkbetriebs und den Trade-off zwischen Energieertrag und Lasten besser zu verstehen, werden zusätzliche Untersuchungen empfohlen.

In einer weiteren Untersuchung wurde anhand von Large Eddy Simulationen ermittelt, wie sich eine Anströmung mit Richtungsscherung auf die Nachlaufentwicklung einer Windenergieanlage auswirkt. Solche Bedingungen treten typischerweise in stabil geschichteter Atmosphäre auf, die für die Anwendung der Nachlaufablenkung von besonderem Interesse ist, da sie zu starken, stabilen Nachläufen führt und Schwankungen der Anströmrichtung gering sind. Es wird gezeigt, dass Richtungsscherung die Ausbildung von asymmetrischen Nachläufen mit ellipsenförmigen Querschnitten bewirkt. In den meisten der existierenden Nachlaufmodellen werden Nachläufe jedoch immer noch als rotationssymmetrisch angenommen. Abhängig von den Umgebungsbedingungen können ungenaue Vorhersagen die Folge sein.

Mit dieser Studie zu verschiedenen Aspekten der Nachlaufablenkung, einschließlich ihrer erfolgreichen Demonstration im Freifeld, wurden wichtige Schritte auf dem Weg zu einer zukünftigen Nutzung der Methode unternommen. In entsprechenden Untersuchungen ist es nun wichtig zu beurteilen, inwieweit die Nachlaufablenkung in realen Windparks wirtschaftlich genutzt werden kann, um den Gesamtertrag zu erhöhen und gleichzeitig die induzierten Ermüdungslasten innerhalb des Auslegungsrahmens zu halten.

Contents

- Abstract** **iii**

- List of Figures** **xi**

- List of Tables** **xix**

- List of Abbreviations** **xxi**

- List of Symbols** **xxiii**

- 1 Introduction** **1**
 - 1.1 Motivation 1
 - 1.2 Current state of science and technology 2
 - 1.2.1 Wind farm control and wake deflection 2
 - 1.2.2 Field experiments at full-scale wind turbines 7
 - 1.2.3 Simulation of wind turbines and wind farms with large-eddy simulations 13
 - 1.3 Open research questions and objectives of this thesis 18
 - 1.4 Structure of the thesis 19

- 2 Field investigation on the influence of yaw misalignment on the propagation of wind turbine wakes** **21**
 - 2.1 Introduction 22
 - 2.2 Methods 25
 - 2.2.1 Measurement campaign and test site description 25
 - 2.2.2 Experimental setup and data processing 26
 - 2.3 Results and Discussion 41
 - 2.3.1 Effect of turbine yaw misalignment on wake development 42
 - 2.3.2 Evaluation of the selected experimental setup and data processing methods 45

2.4	Conclusion	50
3	Numerical investigation on the influence of wake deflection control on the power yield and loading of wind turbines in a wind farm	53
3.1	Introduction	53
3.2	Methods	54
3.2.1	Simulation approach - wake mapping	54
3.2.2	Flow solver	56
3.2.3	Turbine modelling	57
3.2.4	Inflow conditions	58
3.2.5	Power output	69
3.2.6	Structural turbine loading	71
3.2.7	Test case scenario	74
3.3	Results and Discussion	76
3.3.1	Wind field characteristics	77
3.3.2	Wake mapping - power	78
3.3.3	Wake mapping - loading	83
3.3.4	Test case scenario - Impact of wake deflection on power and loading	89
3.4	Conclusion	103
Appendices		
3.A	Appendix A - Parameter files	108
3.B	Appendix B - Normalised load maps (normal operation)	116
3.C	Appendix C - Normalised load maps (yaw misalignment)	120
4	Numerical investigation of wind turbine wake development in direction-ally sheared inflow	123
4.1	Introduction	124
4.2	Methods	125
4.2.1	Flow solver and aeroelastic modelling	125
4.2.2	Coupling procedure	126
4.2.3	Turbine parameters	127
4.2.4	Computational domain	128
4.2.5	Inflow and boundary conditions	129
4.3	Results and Discussion	130
4.3.1	Wake development of a single turbine	131
4.3.2	Wake impact on a downstream turbine	135

4.4 Conclusion	143
5 Conclusions and Outlook	145
5.1 Conclusions	145
5.2 Suggestions for future research	149
References	151
List of publications	167
Acknowledgements	169
Curriculum vitae	171

List of Figures

- 2.1 Map of the test site including the position of the two *eno114* wind turbines (WT-N, WT-S) and the met mast (M) 27
- 2.2 Wind rose from the period of the measurement campaign based on the met mast measurements of wind speed u_M at 91.5 m height and inflow direction β_M at 89.4 m height. The sector highlighted in green marks the inflow directions (195° to 300°) considered in the study. 27
- 2.3 Conceptual visualisation of WT-N and its wake for the clarification of the utilized nomenclature, variables, and orientation of the coordinate systems. The longitudinal wind speed is illustrated by different colour levels. 28
- 2.4 (a) Comparison of 10-min-averaged wind speed measurements of *StreamLine Pro* and met mast cup anemometer at heights of 91.8 m and 91.5 m, respectively (b) Image (colour) and reflection intensity (b/w) of the *StreamLine Pro* trailer, met mast and surrounding recorded using the Z+F IMAGER[®] 5010c laser scanner 32
- 2.5 (a) *StreamLine Pro* hard target measurements of the western and northern met mast edges and measurements predicted for a spatial lidar orientation of $\epsilon_{roll} = -0.4^\circ$, $\epsilon_{pitch} = 0.8^\circ$, and $\epsilon_{yaw} = 1.3^\circ$ (b) Comparison of the 10-min-averaged inflow direction at hub height measured using the *StreamLine Pro* lidar (β_L) installed next to the met mast and the met mast itself (β_M) 33
- 2.6 Time series of the 10-minute-averaged inflow directions determined using the short-range *SpinnerLidar*, the *StreamLine Pro*, and the met mast wind vane on October 29, 2016. 34
- 2.7 Histogram of (a) the standard deviation σ_{β_M} of the inflow direction measurements $\beta_M(89.4\text{m})$ and (b) the turbulence intensity of the met mast wind speed measurements $u_M(91.5\text{m})$ for all analysed 10 min data sets of the yaw experiments, all of which were recorded under neutral conditions. 35

2.8	Average wind veer across the rotor range of WT-N measured using the <i>StreamLine Pro</i> lidar for all 10 min intervals included in the wake analysis. A positive veer value indicates a clockwise change of the inflow direction with increasing height.	36
2.9	Time series of turbine orientation obtained using the supervisory control and data acquisition (SCADA) signal and the global positioning system (GPS) over a 24-hour time period starting at noon on July 5, 2016. Additionally, the corrected GPS signal GPS_{corr} adjusted for disturbances is included.	37
2.10	Plan position indicator scan patterns of the nacelle-based <i>StreamLine XR</i> lidar device (a) top view and (b) side view. The elevation angle φ of the scan is shown in the right graph. The reference scan marks the orientation of the so-called hub height scan considering the average nacelle movement and lidar mounting imperfections.	39
2.11	Schematic representation of rotor equivalent wind speed \bar{u} -based wake tracking algorithm for one downstream distance x_d and three different lateral positions of a virtual downstream turbine. The wake centre is indicated by w_c . For the sake of clarity, $u(x_d, y)$ and $\bar{u}(x_d, y)$ are normalized in the graph.	40
2.12	(a-e) Normalized averaged longitudinal wake flow velocities \hat{u} for all five yaw misalignments test cases under neutral atmospheric conditions. The average wake flow velocities were determined based on the cubic mean of the individual scans to account for the relationship of wind speed and power yield. White dots mark the wake centre at each corresponding downstream distance. Wake tracking based on the rotor equivalent wind speed approach was applied.	43
2.13	Normalized averaged longitudinal wake flow velocities \hat{u} based on the results shown in Figure 2.12 for the three yaw offset bins $\gamma = -20^\circ$, $\gamma = 0^\circ$, and $\gamma = 20^\circ$ and downstream distances of 1.5D, 2D, 3D, 4D, and 5D. The positions of the wake centres are indicated by circles and the wake trajectories by dashed lines.	44

2.14	(a-c) Lateral offsets and corresponding standard deviations of wake trajectories for different degrees of turbine yaw misalignment γ under neutral atmospheric conditions up to downstream distances of 7D and including inflow wind speed bins of 8 ms^{-1} to 10 ms^{-1} . In all three graphs, the shaded area beyond a distance of 2.6D marks the range in which the forest is situated downstream of the wind turbine.	46
2.15	Wake trajectories determined from large-eddy simulations of the <i>NREL 5-MW</i> wind turbine with a rotor diameter of 126 m and different degrees of turbine yaw misalignment γ under neutrally stratified atmospheric conditions. The dashed trajectories are determined for downward tilts ϕ of the measurement plane of 2° and 4°	48
2.16	Mean 10-minute-averaged longitudinal flow 3D and 6D downstream of the <i>NREL 5-MW</i> wind turbine for yaw misalignments of $\pm 20^\circ$ in a neutrally stratified boundary layer. The wake sections measured for the inclination angles ϕ of 0° , 2° , and 4° of the measurement plane are indicated by black horizontal lines of different styles. The corresponding wake centres which are determined by the rotor equivalent wind speed approach, are marked by white dots.	49
3.1	Flow chart of the wake mapping procedure to outline the individual steps	55
3.2	Conceptual visualisation of the investigated turbine layout for the clarification of the utilized nomenclature, variables, and orientation of the coordinate systems	57
3.3	Undisturbed mean longitudinal inflow velocity \hat{u}_c^P (left), longitudinal turbulence intensity TI_{u_c} (centre) and mean inflow direction β_c (right) of the five large-eddy atmospheric boundary layer reference cases <i>N06-N14</i> . The rotor range and hub height of the <i>NREL 5-MW</i> turbine model used in the simulations are emphasized by horizontal dashed and solid lines, respectively.	63
3.4	Distribution of the inflow direction of the large-eddy reference wind fields at hub height, obtained from the 8 Hz time series of a point centred in the reference plane R_{xR} upstream of the wind turbine. The bin width is 1°	64

3.5	Comparison of the (a) average undisturbed longitudinal inflow velocity profile \hat{u}^P and (b) average turbulence intensity profiles TI_u of the first seed of the large-eddy reference simulation <i>N08-1</i> and the corresponding stochastic baseline and filtered <i>TurbSim</i> wind fields <i>S08-1</i> . The rotor range and hub height of the turbine model used in the simulations are emphasized by horizontal dashed and solid lines, respectively.	67
3.6	Comparison of the average spectrum of the longitudinal velocity components $u_{21}(x_R, Y_F, h_H, t)$ of reference wind field <i>N08-1</i> and the corresponding baseline and filtered stochastic wind fields <i>S08-1</i> . In addition, the averaged rotationally sampled spectrum of a point at 2/3 of the blade radius is shown which was obtained for the same turbine positions as the spectrum for the fixed point. The Kolmogorov -5/3 power law for the scaling of turbulence in the inertial subrange is shown for reference.	68
3.7	Average power spectral density of the EB, FB, TS and TF load series of a turbine operating in the undisturbed inflow of <i>N08</i> and a turbine located 6D downstream in the full wake of the upstream turbine.	73
3.8	Layouts of the two reference wind farms WF1 and WF2.	75
3.9	Exemplary inflow case of the reference wind farm <i>WF1</i> for an inflow direction of 145° . The limit of the wake mapping regions of all four turbines <i>WT1</i> , <i>WT2</i> , <i>WT3</i> and <i>WT4</i> are marked by black lines. In the given case, <i>WT4</i> is within the wake map limits of <i>WT2</i> and <i>WT3</i>	76
3.10	Average power values $P_{cs}^{REWS}(x_R, Y_F)$ and $P_{cs}^{FAST}(x_R, Y_F, \gamma)$ at the seven lateral positions Y_F in the reference plane R_{x_R} with undisturbed inflow for all six seeds of the reference wind fields <i>N06</i> to <i>N12</i> . P_{cs}^{STO} indicates the average power of the six stochastic seeds of each large-eddy seed and the corresponding standard deviation.	78
3.11	Normalised power maps $\rho_c^{FAST}(x, y, 0^\circ)$ for the four reference wind fields <i>N06</i> to <i>N12</i>	79
3.12	Standard deviation of the average power values $\rho_c^{FAST}(x, y, 0^\circ)$ of the power maps of the six seeds of each reference case.	80
3.13	Wake mappings of $\eta_c(x, y, 0^\circ)$ which represents the ratio of the normalised REWS-based power maps and the normalised <i>FAST</i> -based power maps for the four reference wind fields <i>N06</i> to <i>N12</i>	82

3.14	Normalised power maps $\rho_c^{\text{FAST}}(x, y, \gamma)$ for the reference wind field <i>N08</i> and turbine yaw misalignments γ of (a) 20° , (b) 10° , (c) -20° and (d) -10°	83
3.15	Power output $\rho_c^{\text{FAST}}(x, 0, \gamma)$ for the reference cases <i>N06</i> to <i>N12</i> and the yaw misalignment cases of <i>N08</i>	84
3.16	Average DELs of the (a) edgewise and (b) flapwise blade root bending moments and the tower base (c) side-to-side and (d) fore-aft moments generated by the undisturbed large-eddy inflow, the stochastic baseline cases (32 Hz) and the filtered stochastic wind fields. The error bars indicate one standard deviation of uncertainty. The results of the five reference cases are plotted slightly shifted with respect to the x-axis for each wind field case to avoid any overlapping of the graphs.	85
3.17	Normalised load maps $\Lambda_c^{\text{FAST}}(x, y, 0^\circ)$ for the reference wind field <i>N08</i> and the load sensors (a) edgewise blade root bending moment, (b) flapwise blade root bending moment, (c) tower base side-to-side moment and (d) tower base fore-aft moment.	88
3.18	Normalised load maps $\Lambda_c^{\text{FAST}}(x, y, \gamma)$ for the reference wind field <i>N08</i> with yaw misalignments γ of the upstream turbine of -20° and 20° and the load sensors for the edgewise and flapwise blade root bending moments.	90
3.19	Normalised load maps $\Lambda_c^{\text{FAST}}(x, y, \gamma)$ for the reference wind field <i>N08</i> with yaw misalignments γ of the upstream turbine of -20° and 20° and the load sensors for the tower base side-to-side moment and tower base fore-aft moment.	91
3.20	Power output P_{WT1} and P_{WT4} for a turbine spacing of 4D and 6D without yaw misalignment of <i>WT1</i> (greedy) and with an optimal yaw misalignment γ of <i>WT1</i> (wake deflection). P_G indicates the overall power gain of <i>WT1</i> and <i>WT4</i> for the case with wake deflection in comparison to the greedy control. The gain is determined with respect to the combined power of both turbines in free inflow conditions (two times 1834 kW).	93
3.21	Edgewise EB_{WT1} , EB_{WT4} and flapwise FB_{WT1} , FB_{WT4} damage equivalent blade loads of <i>WT1</i> and <i>WT4</i> for the configurations presented in Figure 3.20.	97

3.22	Tower base side-to-side TS_{WT1} , TS_{WT4} and tower base fore-aft TF_{WT1} , TF_{WT4} damage equivalent loads of <i>WT1</i> and <i>WT4</i> for the configurations presented in Figure 3.20.	98
3.23	Power outputs of <i>WT1</i> (P_{WT1}) and the entire wind farms <i>WF1</i> and <i>WF2</i> with and without the application of yaw misalignment. The optimal yaw angle of <i>WT1</i> is indicated by γ_{WT1} . P_G indicates the overall power gain of the wind farm if wake deflection is applied. The gain is determined with respect to the combined power of both turbines in free inflow conditions (four times 1834 kW).	100
3.24	Edgewise EB_{WT1} , flapwise FB_{WT1} , tower base side-to-side TS_{WT1} and tower base fore-aft TF_{WT1} damage equivalent loads of <i>WT1</i> for the investigation described in Figure 3.23.	102
3.25	Normalised load maps $\Lambda_c^{FAST}(x,y,0^\circ)$ for the reference wind field <i>N06</i> and the load sensors (a) edgewise blade root bending moment, (b) flapwise blade root bending moment, (c) tower base side-to-side moment and (d) tower base fore-aft moment.	116
3.26	Normalised load maps $\Lambda_c^{FAST}(x,y,0^\circ)$ for the reference wind field <i>N10</i> and the load sensors (a) edgewise blade root bending moment, (b) flapwise blade root bending moment, (c) tower base side-to-side moment and (d) tower base fore-aft moment.	117
3.27	Normalised load maps $\Lambda_c^{FAST}(x,y,0^\circ)$ for the reference wind field <i>N12</i> and the load sensors (a) edgewise blade root bending moment, (b) flapwise blade root bending moment, (c) tower base side-to-side moment and (d) tower base fore-aft moment.	118
3.28	Normalised load maps $\Lambda_c^{FAST}(x,y,0^\circ)$ for the reference wind field <i>N14</i> and the load sensors (a) edgewise blade root bending moment, (b) flapwise blade root bending moment, (c) tower base side-to-side moment and (d) tower base fore-aft moment.	119
3.29	Normalised load maps $\Lambda_c^{FAST}(x,y,\gamma)$ for the reference wind field <i>N08</i> with yaw misalignments γ of the upstream turbine of -10° and 10° and the load sensors for the edgewise and flapwise blade root bending moments.	120
3.30	Normalised load maps $\Lambda_c^{FAST}(x,y,\gamma)$ for the reference wind field <i>N08</i> with yaw misalignments γ of the upstream turbine of -10° and 10° and the load sensors for the tower base side-to-side moment and tower base fore-aft moment.	121

4.1 Coupling scheme of the PALM-FAST framework. 127

4.2 Schematic view of the domain used for the simulations in the fully developed atmospheric boundary layer. 128

4.3 Undisturbed mean longitudinal inflow velocity, inflow direction and distribution of potential temperature of the two investigated stably stratified atmospheric boundary layers conditions S-L and S-H. The rotor range and hub height of the turbine model used in the simulations are emphasized by horizontal dashed and solid lines, respectively. . . . 132

4.4 Mean quasi-equilibrium longitudinal flow behind a turbine at different downstream distances in laminar L-1 and L-0 inflow conditions as seen from upstream. The outer rotor dimensions of the turbine are included as black circle. 133

4.5 Velocity contours of the 600 s averaged longitudinal wake flow of a single turbine for different downstream distances in turbulent S-H inflow conditions as seen from upstream. The outer rotor dimensions are shown as black circle. 133

4.6 Velocity contours of the 600 s averaged longitudinal wake flow of a single turbine in turbulent S-H inflow conditions at hub height (b) and one quarter of a rotor diameter above (a) and below (c). The inflow direction is represented by the arrow ((a) 3.2° (b) -0.3° (c) -2.0°. . . . 134

4.7 Velocity contours of the 600 s averaged longitudinal wake flow (a) and averaged longitudinal wake flow normalized at each height by the undisturbed mean velocity of the inflow profile (b) 4D downstream of a turbine in turbulent S-L and S-H inflow conditions as seen from upstream. The outer rotor dimensions are included as black circles. . . 136

4.8 Velocity contours of the 600 s averaged longitudinal difference of wake flow and undisturbed inflow and the cross-wind (arrows) for two downstream distances in turbulent S-H inflow conditions. The outer rotor dimensions are included as black circles. 136

4.9 Mean 600 s averaged turbulence intensity of the flow behind a turbine at different downstream distances in turbulent S-H inflow conditions as seen from upstream. The outer rotor dimensions are included as black circle. 137

4.10 Schematic view of the turbine layouts used in the performed simulations as seen from above, all distances given in multiples of D. 137

4.11 Mean 600 s averaged longitudinal flow behind two turbines with a downstream distance of 6D for different lateral offsets in turbulent S-H inflow conditions as seen from upstream. The outer rotor dimensions of the upstream and downstream turbine are included as black and white circles, respectively. 139

4.12 Mean 600 s averaged longitudinal inflow velocity at a reference point at two thirds of the blade length for the upstream and the downstream turbine in turbulent S-H inflow conditions for different lateral offsets and a downstream distance of 6D. An angle of 0° corresponds to a straight upward blade orientation. 140

4.13 Averaged maximum and minimum longitudinal velocity in S-H inflow conditions that is experienced by a reference point located at two thirds of the blade length during each revolution of the rotor for different lateral offsets of the downstream turbine. The horizontal dotted lines mark the level obtained in free inflow. 141

4.14 Mean longitudinal flow around two turbines in horizontal planes at hub height (HH) and quarter of a rotor diameter below and above as seen from above for different lateral offsets in S-H inflow condition. . . 142

4.15 Averaged generated power of downstream turbine (P_{ds}) normalized by the power of the upstream turbine (P_{us}) for different lateral offsets and turbulent S-L and S-H inflow conditions. 142

4.16 Sigma interval ($\mu \pm \sigma$) of the 600 s averaged flapwise moment at the blade root shown for the upstream and downstream turbine in turbulent S-H inflow conditions for different lateral offsets and a downstream distance of 6D. The moments were determined for 5° azimuth intervals and normalized with the mean value of the upstream turbine in this interval. An angle of 0° corresponds to a straight upward blade orientation. 143

List of Tables

2.1	Location of the two <i>eno114</i> 3.5 MW prototype wind turbines and the met mast at the Brusow test site	26
2.2	Technical data of the three-bladed pitch-regulated <i>eno114</i> wind turbine .	27
2.3	Percentage distribution of the measured atmospheric stratification at the test site during the full field campaign (1 st July to 9 th November 2016) and the yaw misalignment campaign (26 th October to 7 th November 2016)	30
2.4	Main characteristics and settings of the <i>StreamLine Pro</i> and <i>StreamLine XR</i> lidars	32
2.5	Number of 10-minute-averaged data sets per 1 ms^{-1} wind speed bin for each case of yaw misalignment under neutrally stratified atmospheric conditions. The first column (intended) indicates the intended average yaw offsets for the experiments whereas the second column (measured) shows the average of all measurements for each yaw offset case.	41
3.1	Imposed velocity boundary conditions for the performed simulations . .	60
3.2	Overview of the assignment of the two indices c and s to wind field case and seed. Index c refers to the wind field case $N06$ to $N14$ and runs from 1 to 5. Index s refers to the specific seed (10 min interval) of each reference case and runs from 1 to 6. In addition, a single index c is used to refer to the total 3600 s of an entire reference field.	60
3.3	Characteristics of the five neutrally stratified atmospheric reference offshore boundary layers	62
3.4	Reference power curve obtained through <i>FAST</i> simulations with homogeneous and uniform inflow conditions.	70
3.5	Reference power $\tilde{P}_c^{\text{FAST}}(\gamma)$ and loading information $\tilde{L}_c^{\text{FAST}}(\gamma)$ of the sensors EB, FB, TS and TF of a wind turbines operating in free inflow of the reference wind fields $N06$ to $N14$ without yaw misalignment ($\gamma = 0^\circ$). . .	71

3.6	Reference power ratio $\tilde{\rho}_c^{\text{FAST}}(\gamma)$ and load ratio $\tilde{\Lambda}_c^{\text{FAST}}(\gamma)$ of the load sensors EB, FB, TS and TF of a wind turbines operating under yaw misalignment ($\gamma \neq 0^\circ$) relative to the case without yaw misalignment ($\gamma = 0^\circ$) in free inflow conditions for the reference wind field <i>N08</i>	72
3.7	Overview of the setups of the four test case scenarios. Each scenario was investigated with and without wake deflection being used.	75
3.8	Comparison of the power outputs of the two-turbine test case of this investigation and the results that were published by Gebraad et al. (2016) - Figure 2b. The power outputs of the individual turbines ($P_{1B}(\gamma)$, $P_{2B}(\gamma)$, $P_{1G}(\gamma)$, $P_{2G}(\gamma)$) are normalised with the power output of the upstream turbine without the application of wake deflection. The overall gain of both wind turbines if wake deflection is applied in comparison to conventional greedy operation is indicated by P_{GB} and P_{GG} and was normalised with the combined power of both turbines in undisturbed inflow.	95
3.9	Average DELs of <i>WT1</i> throughout all inflow directions in <i>WF1</i> and <i>WF2</i> configurations with respect to a turbine in free inflow only. The control column indicates whether conventional greedy control or wake deflection was applied.	104
4.1	Characteristics of the atmospheric boundary layers and the derived laminar inflow conditions.	129
4.2	Imposed velocity boundary conditions for the performed simulations.	131
4.3	Normalized 1 Hz damage equivalent loads (DEL) of the flapwise moment (kNm) at the blade root of the downstream turbine (DEL_{ds}) with respect to the upstream turbine (DEL_{us}) for different lateral offsets in S-H inflow conditions.	142

List of Abbreviations

Abbreviation	Definition
AD	actuator disc
ADM	actuator disc model
ADM-R	actuator disc model with rotation
ALM	actuator line model
ACL	actuator line model
BEM	blade element momentum theory
BMWi	German Federal Ministry for Economic Affairs and Energy
BMU	German Federal Ministry for the Environment, Nature Conservation and Nuclear Safety
CNR	carrier-to-noise ratio
D	rotor diameter
DEL	damage equivalent load
EB	edgewise blade root bending moment (FAST - RootMxb1)
ECN	Energy research Centre of the Netherlands
FAST	Fatigue, Aerodynamics, Structures and Turbulence
FB	flapwise blade root bending moment (FAST - RootMyb1)
FLOW	Facility for Large-Scale Computations in Wind Energy Research
GPS	global positioning system
HH	hub height
HLRN	North German Supercomputing Alliance

IEC	International Electrotechnical Commission
IRGASON	integrated CO ₂ /H ₂ O open-path gas analyzer and 3D sonic anemometer
LES	large-eddy simulation
lidar	light detection and ranging
LLNL	Lawrence Livermore National Laboratory
LOS	line-of-sight
M	met mast
N	north
NREL	National Renewable Energy Laboratory
NWTC	National Wind Technology Center
PALM	Parallelized Atmospheric Large-eddy Model
PPI	plan position indicator
PSD	power spectral density
RHI	range height indicator
REWS	rotor equivalent wind speed
RMS	root-mean-square
SABL	stably stratified atmospheric boundary layer
SAR	synthetic aperture radar
SCADA	supervisory control and data acquisition
SOWFA	Simulator fOr Wind Farm Applications
STO	stochastic wind field
SWiFT	Scaled Wind Farm Technology
TF	tower base fore-aft moment (FAST - TwrBsMyt)
TS	tower base side-to-side moment (FAST - TwrBsMxt)
VAD	velocity–azimuth display
W	west

List of Symbols

Common

γ	angle of yaw misalignment
D	rotor diameter
L_x	domain size in longitudinal direction
L_y	domain size in lateral direction
L_z	domain size in vertical direction
u	velocity component in longitudinal direction
v	velocity component in lateral direction
w	velocity component in vertical direction
x	lateral direction of the simulation domain
y	longitudinal direction of the simulation domain
z	vertical direction of the simulation domain

Chapter 2 - Field investigation on the influence of yaw misalignment on the propagation of wind turbine wakes

β_L	<i>StreamLine Pro</i> lidar inflow direction measurement at 91.8 m height
β_M	met mast inflow direction measurement at 89.4 m height
δ	wind veer across the approximate rotor range of the wind turbine between h_1 and h_2
ϵ_{pitch}	orientation angle of the <i>StreamLine Pro</i> lidar

$\varepsilon_{\text{roll}}$	orientation angle of the <i>StreamLine Pro</i> lidar
ε_{yaw}	orientation angle of the <i>StreamLine Pro</i> lidar
θ_s	sonic temperature
σ_{β_M}	standard deviation of the inflow direction measurements β_M
φ	tilt angle of nacelle and the measurement plane of the nacelle-based <i>StreamLine XR</i> lidar
c_T	rotor thrust coefficient
g	gravitational acceleration
GPS	unfiltered turbine azimuth angle signal obtained with GPS
GPS _{corr}	filtered turbine azimuth angle signal obtained with GPS
h_1	approximated lower rotor limit at 41.3 m height
h_2	approximated upper rotor limit at 150.7 m height
h_H	hub height
k	van Karman constant
L	Obukhov length
$\bar{u}(x, y)$	power-based rotor equivalent wind speed
$\hat{u}(x, y)$	normalized averaged longitudinal wake flow velocities
u_*	friction velocity
$u_i(x, y)$	wind speeds of individual <i>StreamLine XR</i> lidar measurements
u_L	<i>StreamLine Pro</i> lidar wind speed measurement at 91.8 m height
u_M	met mast wind speed measurement at 91.5 m height
$u_{M,i}$	undisturbed wind speed measurements of the met mast that correspond to $u_i(x, y)$
$\overline{w'\theta'_s}$	buoyancy flux

$w_c(x)$ wake center (lateral position with the strongest wake effect)

x_d investigated downstream distance

Chapter 3 - Numerical investigation on the influence of wake deflection control on the power yield and loading of wind turbines in a windfarm

α power law exponent

β inflow direction at hub height h_H

$\beta_c(z)$ mean inflow direction of the undisturbed inflow of the five LES reference wind fields at a certain height

$\Delta\beta_c$ change of mean inflow direction of the five LES reference wind fields across the approximate rotor range of the simulated *NREL 5-MW* wind turbine between between 30 m and 150 m height

$\eta_c(x, y, \gamma)$ ratio of the normalized REWS-based power output and the normalized *FAST*-based power output of a waked wind turbine at the position x, y in the wake map of the large-eddy reference wind field with the index c and a yaw misalignment of the upstream turbine of γ

$\Lambda_c^{\text{FAST}}(x, y, \gamma)$ average *FAST*-based DELs (EB, FB, TS, TF) of a wind turbine located at the position x, y in the wake map of the large-eddy reference wind field with the index c and a yaw misalignment of the upstream turbine of γ (normalised with the DEL of a turbine with no yaw misalignment in free inflow)

$\tilde{\Lambda}_c^{\text{FAST}}(\gamma)$ ratio of the *FAST*-based DEL (EB, FB, TS, TF) of a wind turbine in free inflow with a yaw misalignment γ and without yaw misalignment

$\rho_c^{\text{FAST}}(x, y, \gamma)$ average *FAST*-based power output of a wind turbine located at the position x, y in the wake map of the large-eddy reference wind field with the index c and a yaw misalignment of the upstream turbine of γ (normalised with the power output of a turbine with no yaw misalignment in free inflow)

$\tilde{\rho}_c^{\text{FAST}}(\gamma)$ ratio of the *FAST*-based power outputs of a wind turbine in free inflow with a yaw misalignment γ and without yaw misalignment

$\rho_c^{\text{REWS}}(x, y, \gamma)$	average power output based on the rotor equivalent wind speed approach of a wind turbine located at the position x, y in the wake map of the large-eddy reference wind field with the index c and a yaw misalignment of the upstream turbine of γ (normalised with the power output of a turbine with no yaw misalignment in free inflow)
$\sigma_{u_{cs}}(z)$	standard deviation of the longitudinal inflow velocity at a certain height
$A_{x,y}$	all grid points within the rotor area of a wind turbine at a specific location within the domain
c	index ranging from 1-5, referring to a specific reference wind field $N06$ to $N14$
D_{WT}	spacing between upstream and downstream turbine
EB	reference damage equivalent loads for the edgewise blade root bending moment of a wind turbine without yaw misalignment in free inflow
EB _{WT1}	damage equivalent loads for the edgewise blade root bending moment of wind turbine $WT1$ in the investigated wind farm
EB _{WT4}	damage equivalent loads for the edgewise blade root bending moment of wind turbine $WT4$ in the investigated wind farm
FB	reference damage equivalent loads for the flapwise blade root bending moment of a wind turbine without yaw misalignment in free inflow
FB _{WT1}	damage equivalent loads for the flapwise blade root bending moment of wind turbine $WT1$ in the investigated wind farm
FB _{WT4}	damage equivalent loads for the flapwise blade root bending moment of wind turbine $WT4$ in the investigated wind farm
h_{H}	hub height
$h_{\text{M,ref}}$	power law reference height

$L_c^{\text{FAST}}(x, y, \gamma)$	DEL of a load sensor (EB, FB, TS, TF) of a wind turbine with a yaw misalignment γ (or in the wake of a turbine with a yaw misalignment γ) that is obtained from a <i>FAST</i> simulation based on extracted wind fields from the large-eddy simulation with the indices cs at the position x, y
$\tilde{L}_c^{\text{FAST}}(\gamma)$	reference DEL of a load sensor (EB, FB, TS, TF) of a turbine with a yaw misalignment γ in free inflow conditions of the large-eddy reference wind field with the index c
m	Wöhler exponents
$N06$	large-eddy reference wind field of a neutrally stratified atmospheric boundary layer with a mean hub height wind speed of 6 ms^{-1}
$N08$	large-eddy reference wind field of a neutrally stratified atmospheric boundary layer with a mean hub height wind speed of 8 ms^{-1}
$N10$	large-eddy reference wind field of a neutrally stratified atmospheric boundary layer with a mean hub height wind speed of 10 ms^{-1}
$N12$	large-eddy reference wind field of a neutrally stratified atmospheric boundary layer with a mean hub height wind speed of 12 ms^{-1}
$N14$	large-eddy reference wind field of a neutrally stratified atmospheric boundary layer with a mean hub height wind speed of 14 ms^{-1}
$P_{1B}(\gamma)$	power output of the upstream turbine with a yaw misalignment γ normalised with the power output of the upstream turbine without yaw misalignment (our investigation)
$P_{1G}(\gamma)$	power output of the upstream turbine with a yaw misalignment γ normalised with the power output of the upstream turbine without yaw misalignment (investigation by Gebraad et al. (2016))
$P_{2B}(\gamma)$	power output of the downstream turbine normalised with the power output of the upstream turbine without yaw misalignment (our investigation)
$P_{2G}(\gamma)$	power output of the downstream turbine normalised with the power output of the upstream turbine without yaw misalignment (investigation by Gebraad et al. (2016))

$\tilde{P}_c^{\text{FAST}}(\gamma)$	reference power output of a turbine with a yaw misalignment γ in free inflow conditions of the large-eddy reference wind field with the index c
$P_{cs}^{\text{FAST}}(x, y, \gamma)$	10 min averaged power output of a wind turbine with a yaw misalignment γ (or in the wake of a turbine with a yaw misalignment γ) that is obtained from a <i>FAST</i> simulation (<i>RotPwr</i>) based on extracted wind fields from the large-eddy simulation with the indices cs at the position x, y
$P_{cs}^{\text{REWS}}(x, y, \gamma)$	10 min averaged power output of a downstream wind turbine that is obtained based on the power-based rotor equivalent wind speed approach from the large-eddy simulation with the indices cs at the position x, y . If γ is stated, there is an upstream turbine with a corresponding yaw misalignment.
P_{cs}^{STO}	10 min averaged power output of a wind turbine that is obtained from stochastic wind fields which were derived from the large-eddy wind field with the indices cs
P_G	overall power gain (%) of a wind farm achieved by the use of wake deflection in comparison to conventional greedy control
$P_{\text{GB}}(\gamma)$	P_G value for a pair of wind turbines based on our investigation for a comparison with the results of Gebraad et al. (2016)
$P_{\text{GG}}(\gamma)$	P_G value for a pair of wind turbines based on the data of Gebraad et al. (2016) for a comparison with our results
$P_{\text{WT1}}(\gamma)$	power output of turbine <i>WT1</i> with a yaw misalignment of γ in undisturbed inflow
$P_{\text{WT4}}(D_{\text{WT}}, \beta, \gamma)$	power output of turbine <i>WT4</i> that is in the wake of turbine <i>WT1</i> which has a yaw misalignment of γ . The inflow direction is given by β and the spacing of both turbines by D_{WT} .
R_{XR}	reference plane for determining the undisturbed inflow
s	index ranging from 1-6, referring to a specific 10 min time period (seed) within each reference wind field <i>N06</i> to <i>N14</i>

$S08-1$	stochastic baseline wind field corresponding to each large-eddy reference case seed
T	set that includes all time steps of the simulation
TF	reference damage equivalent loads for the tower base fore-aft moment of a wind turbine without yaw misalignment in free inflow
TF_{WT1}	damage equivalent loads for the tower base fore-aft moment of wind turbine $WT1$ in the investigated wind farm
TF_{WT4}	damage equivalent loads for the tower base fore-aft moment of wind turbine $WT4$ in the investigated wind farm
$TI_{u_c}(z)$	longitudinal turbulence intensity
TS	reference damage equivalent loads for the tower base side-to-side moment of a wind turbine without yaw misalignment in free inflow
TS_{WT1}	damage equivalent loads for the tower base side-to-side moment of wind turbine $WT1$ in the investigated wind farm
TS_{WT4}	damage equivalent loads for the tower base side-to-side moment of wind turbine $WT4$ in the investigated wind farm
$\hat{u}_c^P(z)$	mean undisturbed longitudinal inflow velocity (power-based)
$u_{cs}(x, y, z, t)$	longitudinal wind speed of a certain large-eddy wind field seed at a specific location and point in time
$\bar{u}_{cs}(x, y)$	power-based rotor equivalent wind speed (REWS) at a specific position within the simulated domain
$\hat{u}_{cs}(z)$	longitudinal inflow velocity at a certain height
u_g	velocity component of the geostrophic wind
$u_{M,ref}$	power law reference wind speed
$v_{cs}(x, y, z, t)$	lateral wind speed of a certain large-eddy wind field seed at a specific location and point in time
$\hat{v}_{cs}(z)$	lateral inflow velocity at a certain height

v_g	velocity component of the geostrophic wind
x_R	longitudinal position of the reference plane R_{x_R} for undisturbed inflow
Y	set that includes all distinct positions of the grid points along the y -axis within the range of the R_{x_R} reference plane
Y_F	set of seven lateral positions in the R_{x_R} plane from which wind speed information is extracted that serves as a reference for undisturbed inflow conditions
Z	set that includes all distinct positions of the grid points along the z -axis within the rotor range of the reference wind turbine

Chapter 4 - Numerical investigation of wind turbine wake development in directionally sheared inflow

β_{30}	inflow direction at 30 m height
β_{150}	inflow direction at 150 m height
β_{hub}	inflow direction at 90 m hub height
$\Delta\beta$	change in inflow direction across the approximate rotor range of the turbine between 30 m and 150 m height
$\mu_{u,v}$	mean of the two-dimensional velocity vector in the $x - y$ plan at hub height based on 900 s of undisturbed inflow sampled at 2 Hz
$\sigma_{u,v}$	standard deviation of the two-dimensional velocity vector in the $x - y$ plan at hub height based on 900 s of undisturbed inflow sampled at 2 Hz
DEL_{ds}	1 Hz damage equivalent loads (DEL) of the downstream turbine's flapwise blade root bending moment
DEL_{us}	1 Hz damage equivalent loads (DEL) of the upstream turbine's flapwise blade root bending moment
HH	hub height
L-0	inflow conditions based on the mean conditions of S – H without directional shear

L-1	inflow conditions based on the mean conditions of S – H including directional shear
P_{us}	average power output of the upstream
S-H	investigated atmospheric boundary layer with higher directional shear
S-L	investigated atmospheric boundary layer with lower directional shear
TI_{hub}	turbulence intensity at hub height
u_g	velocity component of the geostrophic wind
u_{hub}	wind speed at hub height
v_g	velocity component of the geostrophic wind

Chapter 1

Introduction

1.1 Motivation

By the end of 2018, wind turbines with an overall capacity of approximately 591 GW were installed worldwide (GWEC, 2018). For an economic utilization of the limited number of sites where the highest energy yields can be expected, wind turbines are often grouped in wind farms. In addition to the topographical and legal framework conditions, the mutual aerodynamic influence of the wind turbines is an important factor in the planning of the wind farm layouts. So-called wakes develop downstream of wind turbines and are characterized by lower average wind speeds and higher turbulence intensity in comparison to free flow conditions. Downstream turbines suffer from such unfavourable inflow conditions, which lead to a reduced energy yield and result in higher structural loads. In recent years, different wind farm control procedures were investigated by the scientific community and manufacturers to mitigate these negative effects.

One method that has proven its potential, in wind tunnel experiments and simulations, for increasing the energy yield of a wind farm is wake deflection through yaw misalignment. Sometimes this approach is also referred to as wake steering or yaw control. With this approach, an offset between inflow direction and wind turbine orientation is deliberately introduced. This can lead to more favourable inflow conditions at downstream turbines due to an altered wake trajectory.

Unfortunately, for a reliable, successful and economic application of wake deflection in the field, several further challenges still need to be solved. In particular, the influence of different atmospheric conditions, the effects of wake deflection on the structural loads of the affected wind turbines and the practical implementation in the field have not yet been fully assessed. As part of this thesis, several of those challenges are addressed

and investigated. At first, the current state of knowledge is summarised in Section 1.2 and the specific research questions are derived in Section 1.3.

1.2 Current state of science and technology

In Section 1.2.1, the current state of research on wake deflection is summarized. In the two subsequent Sections 1.2.2 and 1.2.3, the research opportunities given by field experiments and large-eddy simulations (LES) are reviewed. Both methods are important tools in the research of wake development of wind turbines and form the basis for the investigations carried out within the scope of this thesis.

Whereas a quite realistic representation of the atmospheric boundary layer can be achieved in large-eddy simulations, field campaigns in particular are significant for demonstration and validation purposes. In the field, the complex and highly dynamic inflow conditions of the atmospheric boundary layer have to be faced to full extent and only limited information about the ambient conditions is available at any given time. Successful test results under such conditions are therefore an essential step towards an industrial utilization of wake deflection.

1.2.1 Wind farm control and wake deflection

The development of wakes downstream of wind turbines often leads to a mutual aerodynamic influence of wind turbines in a wind farm (Crespo et al. (1999), Vermeer et al. (2003), Sandefer (2009), Bastine (2017), Trujillo (2018)). In research, wind farm control refers to control approaches that take into account multiple turbines or even the whole wind farm and aim at minimising the negative effects of such aerodynamic interactions. Potential objectives of such control strategies include, for example, maximizing the overall power yield of the wind farm, extending the lifetime of turbines by reducing the structural loading, mitigating power fluctuations or tracking a reference wind farm power signal.

Axial induction control and wake deflection control are two main methods of wind farm control that researchers have been investigating for two decades. Axial induction control is driven by the idea that downrating an upstream turbines causes a faster wake recovery and an increased energy yield at the downstream turbine and the wind farm as a whole (Corten and Schaak (2003b), Corten and Schaak (2003a), Machiels et al. (2008)). Unfortunately, the latest investigations with high fidelity LES and wind tunnel experiments have shown that the benefits of this static induction control are marginal at best (Annoni et al. (2016), Bartl and Sætran (2017)). Just recently, a new method called dynamic induction control has been proposed by Yilmaz and Meyers

(2018) and it shows promising results in high fidelity simulations. The approach was implemented as open-loop control and achieved a faster wake recovery by causing a periodic shedding of vortex rings in the wake of the upstream turbine. To estimate the full potential of the approach, further investigations are now required.

Wake deflection is another approach with the primary goal being an increase of the overall performance of a wind farm. The basic idea is to influence the trajectory of a wake by performing systematic control actions at the wake-generating turbine to induce a lateral thrust force on the flow. Yaw control and individual pitch control were investigated with regard to their feasibility. Unfortunately, two studies with individual pitch control led to inconclusive results with only negligible deflections (Ahrens et al. (2016)) or noticeable deflections but additionally significant increases in loads (Gebraad (2014)). However, wake deflection through yaw misalignment has proven its potential in wind tunnel experiments and more recently in simulations. Therefore, when referring to wake deflection this approach is usually meant. Other terms that are sometimes used are wake steering and yaw control.

Yaw based wake deflection is achieved by deliberately introducing an offset between the inflow direction and the orientation of a turbine. As a result, the inflow conditions at downstream turbines might be improved. It is important to understand that the power yield of the misaligned wind turbines is usually reduced. A gain of the overall power yield of a wind farm will therefore only be achieved if the combined increase in power output at all downstream turbines is greater than the loss at the turbines operating under yaw misalignment.

First investigations on wake deflection were carried out in the wind tunnel by Clayton and Filby (1982). Succeeding experiments, focusing on power yield and the characteristics of the wake, were performed by Grant et al. (1997), Grant and Parkin (2000), and by Parkin et al. (2001). In recent studies, wake deflection has been examined in terms of its suitability for wind farm control. Dahlberg and Medici (2003) tested its application with a two-turbine setup. It was demonstrated that the total power of the two turbines can indeed be increased using this approach. In a study by Adaramola and Krogstad (2011) with two model turbines, the suitability of the method for the maximization of power output was reconfirmed.

Campagnolo et al. (2016) went one step further and used a configuration of three model turbines to investigate for which specific yaw settings the energy yield of the wind farm can be improved. Additionally, a closed loop model-free controller was employed with the objective to dynamically drive the three turbines to optimal operational conditions. For the given conditions, a substantial increase in wind farm power output

was achieved.

An analytical model, which aims at predicting the wake deflection and far-wake velocity distribution of a yawed turbine, was presented by Bastankhah and Porté-Agel (2016). Detailed wind tunnel studies with high-resolution stereoscopic particle image velocimetry and a budget study of the steady-state continuity and the Reynolds-averaged Navier-Stokes equations formed the basis of the analysis and for the development of the model.

With regard to the wind tunnel experiments, one should bear in mind that in the listed investigations, various types of inflow conditions and different horizontal axis wind turbine models with two- or three-bladed designs were used. However, the promising results throughout the studies confirm the potential of the method, at least for the conditions found in a wind tunnel environment.

In addition to the wind tunnel experiments, the steady growth of the computational power of computer clusters and the improvement of numerical simulations has led to an increasing number of investigations by numerical simulations. Large-eddy simulations in particular are popular because they allow to examine the influence of different atmospheric boundary layers on the wake development (Section 1.2.3). Something that is difficult or even impossible to reproduce in a wind tunnel. Despite the decisive advantage of large-eddy simulation to consider different atmospheric conditions, simulations are often carried out for neutral boundary layers.

In 2010, Jiménez et al. (2010) performed large-eddy simulations and presented an analytical model to evaluate wake deflection under flow conditions similar to those of neutral atmospheric stratification. The main input variables were the yaw misalignment and the thrust of the rotor. The strong effects of atmospheric stability on the general ability of performing wake deflection was investigated in large-eddy simulations by Vollmer et al. (2016). The stably stratified conditions were found to be the most appropriate conditions for the application of yaw control, whereas under convective conditions, the applicability is questionable because of the lack of an apparent correlation between the yaw misalignment of a turbine and its wake position. This is an important discovery for estimating the possible gain through wake deflection at a certain site.

Based on simulations with a combination of a large-eddy code and an aeroelastic code, Fleming et al. (2015) investigated in detail the application of yaw deflection in a two-turbine case and its impact on the power yield and loading of the turbines. Gebraad et al. (2014, 2016, 2017) used the same approach to derive a data-driven parametric model that can be used to optimise the yaw orientation of wind turbines in a wind farm to im-

prove the overall power generation. Boersma et al. (2018) developed a control-oriented dynamical wind farm model. Derived from the three-dimensional Navier-Stokes equations, simplification and estimations led to a computationally inexpensive model suitable for closed-loop wind farm control algorithms.

However, it is rather problematic that so far only a limited number of simulations in a neutral boundary layer have been used to derive and tune the models. Stable boundary layers, which have the most promising prerequisites for the application of wake deflection, have hardly been considered so far. In addition, the inflow direction variability of the simulations is usually limited to a few degrees. Depending on the wind farm location, frequently occurring larger changes throughout the day might be common. This issue is addressed by Rott et al. (2018) who suggested a robust control algorithm that considers dynamic wind direction changes of the inflow and inaccuracies in determining the wind direction to optimise the power yield in a wind farm through wake deflection.

In order to increase confidence in the models and to improve their applicability, it is therefore essential that they cover a broader range of conditions just as they occur in the field. Despite the advances in model development, highly dynamic and complex inflow conditions, different boundary layer characteristics, turbine interactions, and turbine properties continue to pose challenges.

Since the potential of wake deflection has been proven in wind tunnel experiments and simulations, it is reasonable to extend the investigations to full-scale experiments and to evaluate the approach in the field. Only then are all factors that potentially affect the applicability of wake deflection faced to a full extent. In addition, only a limited number of sensors and measurement locations are available so that the information about the ambient conditions is reduced and uncertainties increase.

An overview of field campaigns focusing on the analysis of wake development, the latest developments, current state-of-the-art techniques, and possibilities and issues is given in Section 1.2.2.

With regard to wake deflection, very few investigations have been carried out in the field to date. Wagenaar and Schepers (2012) presented results from a first field experiment in which yaw misalignment was tested at utility-scale wind turbines. For their 4° and 8° test cases, the wake skew angle was larger than the yaw misalignment of the wind turbines. Furthermore, the most promising results were observed at low wind speeds. Unfortunately, they had a lot of scattering in their data and the results were very sensitive to the specific data filtering. In the end they concluded that no clear overall effect of wake control was seen. Trujillo et al. (2016) focused on the behaviour

of the near-wake under yaw misalignment of a wind turbine. Wake data was obtained with a nacelle-based short-range light detection and ranging device (lidar) at a 5 MW offshore turbine. Distinctive wake paths for various yaw offsets in the investigated range of up to $\pm 10.5^\circ$ were classified and an apparent asymmetry in the wake paths was identified. However, because of the uncertainties in the employed measurement setup, they could not draw firm conclusions regarding its origin. In 2016, the author was coordinating a full-scale field experiment (Chapter 2 (Bromm et al. (2018))). The aim was to demonstrate the applicability of yaw control for deflecting wind turbine wakes in a full-scale field experiment. For this purpose, we conducted a measurement campaign at a multi-megawatt onshore wind turbine. Inflow and wake flow were recorded using ground- and nacelle-based long-range lidar. Turbine yaw misalignments of up to 20° were investigated. For neutrally stratified atmospheric conditions, a lateral deflection of the wake was observed. Larger yaw misalignments resulted in greater wake deflection. Because of the inherent struggle in capturing complex and highly dynamic ambient conditions in the field using a limited number of sensors, we particularly focused on providing a comprehensive and comprehensible description of the measurement setup, including the identification of potential uncertainties. Fleming et al. (2017a) performed a first field test in which wake deflection was applied to increase the power capture of an array of turbines within a commercial wind farm. They concluded that the analysis of the collected supervisory control and data acquisition (SCADA) measurements indicate a successful application within the certainty afforded by the available data. Unfortunately, no statements about the wake characteristics could be made because no remote sensing devices were used. Two further field campaigns were performed by researchers at the National Wind Technology Center and the SWiFT facility of Sandia in the USA. Turbines that operated under yaw misalignment were investigated (Fleming et al. (2016, 2017b) and Naughton (2017)). Load assessments for the given conditions were presented by Ennis (2017) and Ennis et al. (2018) and Damiani et al. (2018). Ennis et al. pointed out that in the presence of shear, negative yaw offset values were seen to produce the highest level of flapwise blade damage while also reducing power. They refer to this as having the highest 'system costs'. According to their analysis, a slightly positive yaw offset of a wind turbine would be optimal. Unfortunately, the location of this optimal operation point is dependent on the level of shear. Obtaining detailed information about the inflow conditions at a site would therefore be valuable. Damiani et al. concluded that multiple factors are responsible for the damage equivalent loads (DELs) of the various components. Primary drivers are airfoil aerodynamics, elastic characteristics of the rotor, and

turbulence intensities. Furthermore, fatigue and extreme loads were observed to have relatively complex trends with yaw offsets, which can change depending on the wind speed regime.

1.2.2 Field experiments at full-scale wind turbines

Measurement campaigns in the field make a decisive contribution to acquiring knowledge about the operation and interaction of utility-scale wind turbines. Simulations and wind tunnel experiments have the advantages of being repeatable and reproducible. Unfortunately, realistic field conditions can only be approximated, but not fully reproduced (e.g. changes in inflow direction or atmospheric stratification). Therefore, high quality field measurements are of great interest for understanding the capabilities and limitations of simulation tools and are essential for their validation and improvement. In addition, specific constraints, uncertainties and challenges exist in the practical implementation in the field, which are not relevant in simulations and small-scale tests. Examples illustrating these issues are the exact positioning, reliability and accuracy of a certain sensor. What uncertainties are to be expected in the field in comparison to laboratory conditions and how will they affect the desired and predicted results? Manufacturer and wind farm operators are often hesitant regarding the implementation of new functionality due to possibly existing unforeseeable risks. Demonstrations in the field can help to dispel doubts.

Depending on the given research questions, the focus of measurement campaigns can be on very different aspects. In addition, the requirements also change with further research and advancing technological development. Of particular importance for the investigation of wake deflection are the possibilities to characterize the inflow and wake of wind turbines, the documentation of the status and operating points of a turbine and the occurring structural loads. For these aspects, the current state of technology and the development of field campaigns in recent years are presented in the following. Important characteristics of the inflow are the wind speed and the inflow direction at different heights, the turbulence intensity and the atmospheric stability. Conventional wind speed measurements are performed with cup anemometers or ultrasonic anemometers and the inflow direction is obtained with wind vanes. The turbulence intensity is derived from the wind speed measurements as it is determined by dividing the standard deviation of the wind speed during a certain time period by its average (IEC (2005)). Anemometers and wind vanes are typically installed on the nacelle of a turbine or at different heights at a met mast nearby. The latter measurements have the advantage that the wind speed and inflow direction can be captured mostly undis-

turbed whereas the inflow characteristics at the nacelle are affected by the rotor. At dedicated wind farm test sites (e.g. DTU (DTU (2018)), NWTC (NREL (2015)), SWiFT (Berg et al. (2014))) met masts measurements serve as references for the validation of more complex measurement systems due to the experience with the systems, the robustness of the sensors and a comparatively simple data analysis. However, the considerable costs of a met mast, which are significantly increasing with larger turbine heights, small spatial resolutions and the low flexibility in the choice of measuring locations, set limits. In particular, the installation of offshore met masts is expensive. Another drawback is that construction permits are usually required for the erection of met masts. If field campaigns are not performed at a dedicated test site, measurements in wind farms with prototype turbines are often a feasible option. In such cases a met masts is typically available as it is used for certification purposes.

However, when it comes to the analysis of wake flows, even this approach is not suitable for covering most research questions. If met masts are installed for certification purposes, their location is optimised for undisturbed inflow and wake situations barely occur. Even if the met mast is frequently located in the wake of a turbine, the usual low spatial resolution does not allow the dynamic wake effects to be captured.

With the introduction of the remote-sensing lidar technology to wind energy applications (Bingöl et al. (2008) and Käsler et al. (2010)), new opportunities have opened up, enabling more comprehensive and extensive investigations of the flow around individual wind turbines and entire wind farms.

Lidar devices transmit a laser beam into the atmosphere and detect the light that is backscattered by aerosol particles that are assumed to move with the wind speed. Because of the Doppler effect, a frequency shift between the received laser pulse and the outgoing one occurs. This information is used to determine the wind velocity in the line-of-sight (LOS) direction of the laser.

In contrast to conventional anemometers, remote sensing devices are much more versatile. Several types of lidar exist which can be positioned on the ground (Käsler et al. (2010)), on the nacelle of a wind turbine (Bingöl et al. (2008)) or even in its spinner (Angelou et al. (2010)). Depending on the type of equipment, even in several kilometres distance, wind speed measurements can be obtained at high spatial and temporal resolutions. Two very common scan strategies are the plan position indicator (PPI) scan and the range height indicator (RHI) scan. During PPI scans, the elevation angle of the scanner is kept constant but the azimuth angle varies. For a RHI scan, the azimuth angle is kept constant but the elevation angle varies. Two other typical scan strategies are the staring mode, which refers to a continuous measurement in a fixed direction

(Trabucchi et al. (2015)), and the complex trajectory setup during which several points in space are successively visited (Schlipf et al. (2010)).

Based on these possibilities, it seems obvious to perform wind speed measurements entirely with lidar devices. Unfortunately, this technology also has its limitations and different challenges do exist. Despite an increasing market penetration, the acquisition of most types of lidar devices is still very cost-intensive. Furthermore, due to the complexity of the devices they must be monitored regularly to ensure proper operation. The given flexibility when setting up the measurements in a campaign usually results in a more time-consuming data analysis. For these reasons, in the field of wind energy, the devices are mostly used in research applications. An example for the industrial application of lidar devices is the determination of vertical inflow profiles of wind speed and inflow direction with velocity–azimuth display (VAD) lidars. The mid-term goal is to replace the costly met masts that have been used so far. Nevertheless, there are challenges with this approach as well. Due to inherent spatial averaging, the turbulence intensity measured by lidar systems differs from the one obtained with anemometers (Mann et al. (2008) and Sathe et al. (2011)). Without a met mast, new rules on how to perform turbulence measurements need to be established.

Another important aspect to consider when performing a field campaign is the atmospheric stability at the site due to its significant influence on the wake development of wind turbines (Churchfield et al. (2012), Dörenkämper et al. (2014), Hansen et al. (2012) and Magnusson and Smedman (1994)). With the increase of the height and diameter of turbine rotors, atmospheric characteristics as for example wind veer, which were hardly in the focus in the past, gain more attention.

However, the classification of the stability requires precise measurements of several characteristics of the ambient atmospheric flow as for example pressure, temperature, humidity and wind speed (Arya and Holton (2001)). Using the eddy covariance technique, surface fluxes are determined and the atmospheric stratification can be categorized based on the Monin-Obukhov length (Monin and Obukhov (1954) and Obukhov (1971)).

In homogeneous terrain, ground-based measurements can be sufficient to estimate the conditions at hub height. In more complex terrain, the conditions at the ground can differ from those at greater heights and might require additional measurements. If a met mast is available at the site, in-situ measurements at different heights are one way of obtaining the necessary data. A further option is to use microwave radiometers. Friedrich et al. (2012) demonstrated that remote sensing measurements, which were recorded with such devices, can lead to comparable results as the ones obtained in-situ

with a met mast. For certain applications, however, a higher vertical resolution would be desirable.

Further remote sensing techniques that are being used for wind speed measurements include aircraft- or satellite-based synthetic aperture radar (SAR) (Christiansen and Hasager (2005, 2006)) and ground-based dual Doppler radars. So far, both methods are used very rarely. SAR is limited to offshore applications as it estimates the wind speed based on the small-scale roughness at the sea surface. Due to the limited temporal and spatial resolution of this approach, it is typically used for the estimation of the available wind resources and for the assessment of the far-reaching wakes of entire offshore wind farms to understand how they affect wind farms that are located downstream. Since the focus of this work is on the characteristics of wakes of individual wind turbines, this method is not discussed further. Dual Doppler radars have been used to measure wind speeds in onshore wind farms (Hirth et al. (2012, 2014, 2015) and Marathe et al. (2015)) and at offshore wind farms near the coast (Nygaard and Newcombe (2018)). In comparison to lidar devices, they allow to collect wind speed data for even larger areas with high spatial and temporal resolutions. This data can be used to verify wake models for larger groups of wind turbines. The published measurements that were recorded with radar offer interesting insights. However, due to the enormous costs, their availability is currently low, even in the scientific context.

For capturing the status and operating points of the investigated wind turbines and to correlate them with the conditions of the ambient flow and the operation of neighbouring turbines, supervisory control and data acquisition (SCADA) systems are typically used. Such systems are integrated in every turbine and allow its operation and monitoring by collecting data from different sensors. Common outputs include the power yield of the turbine, its operational status, and wind speed and relative wind direction measurements on top of the nacelle. Usually for each sensor, the 10 min averages and the minimum value, maximum value and standard deviation of the corresponding time interval are calculated and stored. In case of need, the systems are capable of collecting data with much higher temporal resolutions.

Due to the high prevalence of SCADA systems, long-term operational data of onshore and offshore wind farms is available and can be used for investigating the interaction of wind turbines in wind farms. As all measurements are carried out at the turbines themselves, there is no information about the flow conditions between the turbines and outside the wind farm. Furthermore, as already mentioned, wind speed and wind direction measurements are carried out on the nacelles of the turbines and are thus influenced by the rotor. Since the sensors have so far only been used to ensure the

functionality and safety of the systems, it must be kept in mind that the accuracy of the sensors does not necessarily meet the requirements of scientific investigations (e.g. SCADA yaw signal (Bromm et al. (2018))). Often SCADA signals are relied upon due to a lack of awareness of potential errors or a lack of comparative measurements. Another example is the alignment of sensors (Mittelmeier and Kühn (2018)). The alignment of inflow direction measurements and absolute turbine orientation seems to be a simple task. However, establishing a common coordinate system for all employed sensors requires a structured approach and a high degree of precision. This also applies to the positioning of lidar devices. Due to the high measuring distances, small inclinations of the devices can have a large effect on the measuring position (Bromm et al. (2018) and Vasiljević et al. (2017)).

Another crucial aspect of a field campaign and the assessment of new control concepts in general are load measurements. There are two main reasons for this. First, the installation of load monitoring systems in the field can be time-consuming and the sensors are susceptible to failures so that the measurement campaigns are interrupted. Secondly, load data needs to be recorded with a high resolution, which results in large amounts of data and a very cumbersome post-processing and data analysis.

Once the data is available there is the dilemma, that the application of new control concepts might lead to an increase in power yield but it is in many cases accompanied by higher structural loads as well. This requires a trade-off and raises the question of how loads and power yield should be weighted? The latter can be easily converted into monetary loss or revenue. Converting loads in the same way is one of the great challenges in wind energy research.

To record the load data of wind turbines, several options do exist. General requirements for certification purposes are described by the IEC (IEC (2015)). Regions of interest are at the blade root, the main shaft, the tower top and the tower bottom. Optical sensors such as fibre Bragg gratings seem promising due to the advantages of a long lifetime, stable performance (i.e. no re-calibration) and no interference with electrical devices (Verbruggen (2009)). Because the sensors are expensive and not yet as reliable as one would like them to be, they have not fully established themselves on the market up to now. Strain gauges are less expensive and commonly used. Unfortunately, they have the disadvantages of a greater sensitivity to temperature variations, a finite lifetime and the tendency to drift which requires re-calibration (Verbruggen (2009)).

If one compares current measurement campaigns for the validation of wind farm control concepts, one recognises that no recommended practices or suggestions for measurement procedures and post-processing routines exist. In publications, measurement

setups are sometimes just briefly described and details like sensor alignment and the verification of measurement data are not comprehensively addressed. This makes it difficult to assess the quality of the data, and increases the risk that relevant aspects are not taken into account. In addition, a wide range of different methods (e.g. filtering of data, definitions of the wake centre and the wake width) and an increasing complexity of current field campaigns reduces the comparability. The whole topic is not always given the appropriate significance but some recent publications have focused more on these important aspects and a more critical examination seems to have started.

In the following, a few exemplary publications are addressed which, from the author's point of view, illustrate the complexity and the state-of-the-art of wind turbine wake research in the field at utility-scale wind turbines within the last few years.

Aitken and Lundquist (2014), Iungo and Porté-Agel (2014) and Machefaux et al. (2016) all performed measurement campaigns to investigate the influence of different atmospheric conditions on the wake development. In all three cases, lidar devices were used to capture the surrounding flow of the investigated turbines. Aitken and Lundquist (2014) installed a long-range lidar device on the nacelle of a wind turbine as it allowed them to more consistently transect the centre part of the wake in comparison to setups with ground-based devices. By comparing daytime and nocturnal conditions, differences in wake growth rate and the amplitude of the wake meandering were observed and attributed to different ambient turbulence characteristics. Iungo and Porté-Agel (2014) presented field measurements with up to three lidars for a wind turbine located in a narrow valley in Switzerland. Due to the availability of multiple devices, one was entirely dedicated to inflow measurements whereas the two other devices were used to capture the complex wake flow of the turbine in detail under different atmospheric conditions. They evaluated the wake deficit at several downstream positions in neutral and convective boundary layers and emphasized a noticeable effect of the stability of the atmospheric boundary layer on the downstream evolution and recovery of wind turbine wakes. Machefaux et al. (2016) presented the results of wake measurements obtained at the Risø campus test site for stable and unstable atmospheric stratification. Also in this case, a nacelle-based long-range lidar device was used. By modifying a standard device, the capturing of cross sections of the wake was improved. In addition, different approaches for stability classification were tested in this campaign and all measurement results were compared with data from large-eddy simulations.

Investigations of wind turbines operating under yaw misalignment were performed in the USA at the National Wind Technology Center and the SWiFT facility of Sandia

(Fleming et al. (2016, 2017b)). For these tests, the turbine controllers were adjusted to investigate this unconventional operational mode. Met masts nearby captured the ambient conditions. Load assessments for both campaigns were presented by Damiani et al. (2018) and Ennis (2017).

Marathe et al. (2015) investigated the wake development of a wind turbine in yawed conditions with two mobile Ka-band radars and a met mast. They conclude that a yawed rotor can deflect the wake in the near-wake region. The far-wake is more dependent on atmospheric factors. In their publication, they explicitly highlight crucial aspects of their field campaign and state the requirements (e.g. definition of true north, atmospheric stability, inflow direction and turbine alignment). These pieces of information are very helpful for others as they allow to understand the process that led to the results and are valuable information for the setup of new campaigns. Due to their high costs, radars are currently only rarely used in wind energy research despite their benefits for wake measurements like the long range and suitable temporal resolution. Last but not least, Vasiljević et al. (2017) described the setup of the Perdigo experiment with a wind turbine being located on a mountain ridge in Portugal. Several short-range and long-range multi-Doppler lidar instruments were combined to map the flow around the wind turbine. The novelty of the setup and the complexity of the terrain required them to develop a methodology for achieving the best performance with their measurement setup. By presenting a detailed description of the campaign, the reader has the opportunity to fully understand how the data was gathered. Furthermore, this gives other researchers the opportunity to critically assess the proposed methods of analysis and compare them with the ones they use themselves, ensuring an advancement of scientific knowledge.

1.2.3 Simulation of wind turbines and wind farms with large-eddy simulations

As pointed out in the previous sections, the ambient atmospheric conditions at a site have a strong influence on the wake development of wind turbines. This aspect is also given more and more consideration in simulations. In comparison to wind tunnel and field experiments, they have the advantages of allowing more diverse investigations for a wide range of ambient conditions and turbine operating points in a controlled, well-known and reproducible full-scale environment. In addition, data with a very high spatial and temporal resolution can be obtained. A particularly realistic representation of the conditions in the atmospheric boundary layer is with current technical capabilities best achieved with large-eddy simulations. A wide range of turbulent length

scales is resolved and only turbulent scales below the grid size of the simulation domain are parameterized. Furthermore, not only the mean flow is determined but the major part of the turbulent fluctuations is obtained as well which are important for characterizing the wake dynamics and for estimating turbine loads. Despite the high computational demands, LES has become more and more common due to the increase of computational power of computer clusters and code development. Whereas LES was in the past mostly used for very specific individual reference cases, nowadays larger studies are performed in which a broader range of situations are investigated. Furthermore, even though LES itself does not fulfil the desire for being computationally inexpensive, fast and sufficiently accurate, its simulation results are increasingly used as a reference for the development and validation of such engineering models (Abkar et al. (2018), Gebraad et al. (2014, 2016) and Jiménez et al. (2010)).

With regard to the modelling of wind turbines within LES, various approaches have been established. Depending on the complexity of the chosen model, the duration of the simulations and the field of application differ. In the following, the three currently most common model approaches are described. For each of them, a few exemplary studies are presented in which the corresponding modelling approach was applied.

The actuator disc model (AD/ADM) is the most basic modelling approach. Thrust forces are distributed on a permeable disc of zero thickness, which represents the swept rotor area (Froude (1889) and Mikkelsen and Sørensen (2004)). The rotation of the rotor and how it affects the wake development is not considered. Therefore, in comparison to more complex models, less accurate results are obtained in the near wake region with its more pronounced wake rotation. However, the approach allows choosing relatively large simulation time steps and thus results in the fastest simulation times. An early study with turbulent inflow conditions was performed by Jiménez et al. (2008). The focus of their work was on the characteristics of the spectral coherence of turbulence fluctuations in wind turbine wakes. They compared their LES based results with experimental data from the Danish wind farm Nørrekær Enge II and with an analytical model. Reasonable agreements were obtained. Calaf et al. (2010) studied a fully developed wind turbine array boundary layer. Different turbine arrangements, loading factors and surface roughness values were chosen. The vertical transport of momentum and kinetic energy across the boundary layers was analysed. It was shown that the vertical fluxes of kinetic energy are of the same order of magnitude as the power extracted by the forces modelling the wind turbines. In addition, a modified model for predicting the effective roughness length of a wind farm was proposed. Wu and Porté-Agel (2011) investigated the characteristics of a wind turbine wake in a neutral

turbulent boundary-layer flow with LES. The turbine was implemented based on the actuator disc and the more advanced actuator disc approach with rotation. Both results were compared with data from wind tunnel experiments with a miniature turbine. In general, the wake characteristics from the LES were in good agreement with the measurements of the far-wake region.

The actuator disc model with rotation (ADM-R) (Sørensen and Kock (1995) and Wu and Porté-Agel (2011)) is the second model type covered and it can be seen as an enhanced ADM approach. In the ADM-R model, the rotor disk is divided into rotor annulus segments with varying properties along the radial axis to represent the blade characteristics. Due to the rotation of the rotor, an azimuthal velocity is assigned to each of these segments. However, the absolute positions of all blade segments are fixed and time independent. Lift and drag coefficients of the blades and the local velocities at each segment are used to calculate the lift and drag forces based on blade-element theory. The axial and tangential forces are scaled for a three bladed turbine and are distributed onto the underlying grid. Singular behaviour is avoided by a regularization kernel to ensure the smoothness of the distribution. Despite the slower simulation time in comparison to the ADM, the ADM-R is often used. This is the case as it takes the rotation of the wake into account, which leads to more realistic results in small and medium downstream distances.

Porté-Agel et al. (2013) performed an LES study with the ADM-R turbine model to investigate the effect of changing wind direction on the turbine wakes and associated power losses in the Horns Rev offshore wind farm. The results show that even small changes of the inflow direction can have a strong impact on the total power yield of the wind farm. A change in wind direction of just 10° from the worst-case wake scenario was found to increase the overall power yield by as much as 43 %. Dörenkämper et al. (2015c) investigated the impact of the stably stratified atmospheric boundary layer (SABL) on power yield and wake effects in an offshore wind farms by means of LES and measurements. In addition, the influence of the distance between wind farm and shore on the power yield was investigated. Besides the effects of the coast, jets between the turbine rows within the wind farm were identified. Vollmer et al. (2016) used the ADM-R model to investigate the general ability of performing wake deflection and their specific characteristics for different atmospheric stratifications. Stably stratified conditions were found to be the most appropriate conditions for the application of yaw control, whereas under convective conditions, the applicability is questionable because of the lack of an apparent correlation between the yaw misalignment of a turbine and its wake position. In this dissertation, the ADM-R approach was used to obtain

the wakes of a single turbine for the wake mapping approach, which is presented in Chapter 3.

The most sophisticated modelling approach in LES that is currently being used is the actuator line model (ACL/ALM) which was introduced by Sørensen and Shen (2002). Because it is not feasible to capture the blade geometry in full detail, due to the high computational demand, the blades are divided into multiple segments. Each segment is represented by a reference point for which the local blade forces are determined in each time step. With an appropriate resolution, this approach makes it possible to resolve wake features like tip and hub vortices.

The actuator line approach was used by Troldborg et al. (2007) and Troldborg et al. (2011) to investigate the wakes of a single wind turbine and two turbines operating in turbulent inflow condition. The wake characteristics of the single turbine were compared with the ones from a turbine in uniform inflow. In the second work, the focus was on the interaction of the wakes of the two turbines. Lu and Porté-Agel (2011) and Bhaganagar and Debnath (2014) used the actuator line technique in combination with LES to analyse the wake characteristics in a stably stratified boundary layer. Non-axisymmetric wind turbine wakes were observed in response to the non-uniform incoming turbulence, the Coriolis effect, and the rotational effects induced by blade motion. Atmospheric boundary layer metrics strongly affect the evolution of tip and root vortices formed behind the rotor and the strength and size of the turbulent mixing layer downstream of the turbines decreases with increasing stability. The wake characteristics of two turbines in unstably stratified and neutrally stratified conditions at sites with low and high surface roughness were investigated by Churchfield et al. (2012). Information about the structural bending moments of the wind turbines at several locations were determined. The root-mean-square (RMS) turbine loads are consistently larger when the surface roughness is higher. The two different atmospheric boundary conditions, however, do not have a uniform effect on the turbine loads. RMS blade root out-of-plane bending moment and low-speed shaft torque were found to be higher in an unstably stratified boundary layer. In contrast, the RMS yaw moments were either equal or increased in the neutrally stratified boundary layer. The overall power yield of both turbines was found to be higher in unstable conditions than in neutral conditions.

In order to understand the strengths and weaknesses of the individual models, it is useful to carry out comparative simulations with different models and to refer to data from experiments in the wind tunnel or field. Troldborg et al. (2015) simulated the wake of the *NREL 5-MW* reference wind turbine in uniform and turbulent inflow con-

ditions with a fully resolved rotor geometry, an actuator line method and an actuator disc method. Their investigations showed that the wake properties predicted by the actuator disc and line models are in very close agreement for uniform inflow conditions. However, those predicted by the fully resolved rotor differ significantly, as they are characterized by much higher turbulence. For turbulent inflow conditions, the wake characteristics predicted by the three methods were in close agreement. This indicates that the differences observed in uniform inflow are less relevant in turbulent conditions. Martínez-Tossas et al. (2015) performed simulations with the actuator disk and actuator line models. In addition, they examined the impact of several parameters of the simulation (e.g. grid spacing) on the results. Despite differences in the near-wake, the wakes predicted by both modelling approaches were found to be very similar in the far-wake. Comparisons with data from wind tunnel experiments showed good agreement between measured and predicted power, wake profiles, and turbulent kinetic energy for most tip speed ratios. The better results in the near-wake with the ACL model compared to the AD model were confirmed by Stevens et al. (2018). An investigation of four different LES research codes from the wind energy community was performed by Martínez-Tossas et al. (2018). The turbines were implemented based on the ACL approach and quantities along the blades were shown to match closely for all codes. In turbulent conditions, the empirical Smagorinsky coefficient of the eddy-viscosity model had only a negligible effect on the wake profiles. They concluded that for the tested configurations, the characteristics of the inflow turbulence appear to be more important than the details of the subgrid-scale modelling employed in the wake. In recent years, besides plain LES simulations, coupled approaches of LES code and aeroelastic code have become popular. Such frameworks are often referred to as high-fidelity simulations. One aim with these tools is to not only estimate the power yield of turbines or wind farms, but also to be able to draw conclusions about the structural loading of individual turbines and their components. Furthermore, some of these frameworks provide an interface for performing wind farm control. If the focus is solely on the power yield of the wind farm, the turbines are typically modelled with the ADM-R approach due to the shorter simulation time. If information about the structural loading of the turbines is required, the turbines in the LES are modelled based on the ACL approach. One high-fidelity framework is SOWFA (Churchfield et al. (2012), Fleming et al. (2013a) and Fleming et al. (2013b)) which is based on OpenFOAM and FAST (Jonkman and Buhl, Jr. (2005)). A significant feature is that each turbine is capable of communicating with a central controller unit. Due to this possibility, SOWFA was used in many investigations on using wind farm control for improving turbine

performance (Fleming et al. (2015) and Gebraad et al. (2014, 2016)).

A framework that consists of the LES code PALM (Maronga et al. (2015) and Raasch and Schröter (2011)) and the aeroelastic code FAST was developed by the author with the wind turbines being modelled based on the ACL approach. It was used to investigate the wake development in directionally sheared inflow (Bromm et al. (2017c), Chapter 4). Such conditions result in non-symmetrical wake development, which transfers to distinct differences in the energy yield and loading of downstream turbines of equal lateral offsets in opposite directions.

Storey et al. (2013) coupled LES with FAST and used the ADM-R approach for modelling the turbine. This approach results in a computationally efficient simulation. Despite the limitations of the ADM-R model in comparison to the ACL model, they point out that their results show trends in wake structure comparable with those seen in other work, including velocity profile development and shifts in blade loads.

1.3 Open research questions and objectives of this thesis

The motivation that led to this thesis is twofold. Firstly, there is the fundamental question regarding the potential of wake deflection through yaw misalignment and how this control concept can be used to reduce the cost of energy. Secondly, the requirements for a successful and robust application of the method at multi-megawatt wind turbines in the field needs to be better understood.

Despite promising results in the past, it was found that certain relevant factors were not taken into account in previous studies, mainly, due to a lack of the necessary means of investigation. In particular, this applies to the influence of different atmospheric boundary layer characteristics. Wind veer and inflow direction variability, for example, cannot easily, if at all, be represented in a wind tunnel. Furthermore, just in recent years, large-eddy simulations became viable means to perform simulations of wind turbines in realistic atmospheric boundary layers.

Therefore, an evaluation of the potential of wake deflection under real-life conditions with complex and highly dynamic flow regimes is necessary. Consequently, the following research questions were derived:

1. Can the wake of a utility-scale wind turbine in the field be systematically deflected through yaw misalignment and what are the requirements?
2. How do the power yields and loadings of wind turbines in a wind farm differ if, in comparison to conventional wind farm operation, wake deflection through yaw misalignment is applied?

3. How is a wind turbine's wake development and its aerodynamic interaction with a downstream turbine influenced by directionally sheared inflow?

1.4 Structure of the thesis

The thesis consists of an introductory chapter, three main chapters and a conclusion. Chapter 2 and Chapter 4 are peer-reviewed paper contributions and were previously published in the *Wind Energy* journal. Chapter 3 is an unpublished contribution.

Chapter 1 introduces the reader to wind farm control through wake deflection and gives an overview about the state-of-the-art of field experiments at full-scale wind turbines and the possibilities through large-eddy simulations. Subsequently, the objectives and research questions of this thesis are derived.

In Chapter 2, Bromm et al. (2018), 'Field investigation on the influence of yaw misalignment on the propagation of wind turbine wakes', the first research question is addressed. A measurement campaign at a multi-megawatt onshore wind turbine is described in which the applicability of wake deflection was investigated for neutrally stratified conditions and yaw offsets of up to 20° in a full-scale field experiment. State-of-the-art measurement devices, e.g. multiple lidars, global positioning systems (GPS) and eddy covariance stations were used to capture the inflow characteristics, wake flow, and turbine orientation. Due to the complexity of the measurement campaign and the high demands on the accuracy of the measurements, great emphasis was placed on a comprehensive description of the setup, including the identification of potential uncertainties.

Chapter 3 relates to the second research question and focuses on how the application of wake deflection at a turbine influences its power yield and loading, and the ones of a downstream turbine. Large-eddy simulations with a single wind turbine were performed and wind fields were extracted from the wake flow. Subsequently, these wind fields were used in aeroelastic simulations to estimate both the power yield and the loads at the blades and the tower of a virtual downstream wind turbine that would be affected by the wake flow. Several different partial and full wake conditions were investigated. The results of all investigated configurations were stored in matrices that are referred to as power and load maps. Based on this data, the power yield and loading of turbines in two exemplary wind farms with well-defined boundary conditions were estimated in case of wake deflection being applied and for conventional wind farm operation.

Chapter 4, Bromm et al. (2017c), 'Numerical investigation of wind turbine wake development in directionally sheared inflow', addresses the third research question and

focuses on the impact of wind veer on the wake development in different stably stratified boundary layers. This is of particular importance as the highest amount of wind veer is observed in stably stratified conditions, which also show the highest potential for the application of wake deflection. A simulation framework that consists of an aeroelastic code and a large-eddy code was developed to simulate two-turbine wind farm layouts. Both wind turbines were well aligned with the inflow direction at hub height to emphasize the influence of directional shear on the wake characteristics and avoid any effects through yaw misalignment. The wakes of both turbines were investigated and differences in the power yield and the loading of the downstream turbine for different lateral positions were assessed.

At last, the main conclusions of the thesis are presented in Chapter 5 and suggestions for future studies are given.

Chapter 2

Field investigation on the influence of yaw misalignment on the propagation of wind turbine wakes

The content of this chapter is identical to the journal article *Bromm et al. (2018)*: Bromm, M., Rott, A., Beck, H., Vollmer, L., Steinfeld, G. and Kühn, M. (2018). 'Field investigation on the influence of yaw misalignment on the propagation of wind turbine wakes.' In: *Wind Energy*, pp. 1–18. DOI: 10.1002/we.2210 Copyright ©2018 John Wiley & Sons, Ltd. (used with permission).

Abstract

A comprehensive understanding of the wake development of wind turbines is essential for improving the power yield of wind farms and for reducing the structural loading of the turbines. Reducing the overall negative impact of wake flows on individual turbines in a farm is one goal of wind farm control. We aim to demonstrate the applicability of yaw control for deflecting wind turbine wakes in a full-scale field experiment. For this purpose, we conducted a measurement campaign at a multi-megawatt on-shore wind turbine including inflow and wake flow measurements using ground- and nacelle-based long-range light detection and ranging devices. Yaw misalignments of the turbine with respect to the inflow direction of up to 20° were investigated. We were able to show that under neutral atmospheric conditions, these turbine misalignments cause lateral deflections of its wake. Larger yaw misalignments resulted in greater wake deflection. Because of the inherent struggle in capturing complex and highly dynamic ambient conditions in the field using a limited number of sensors, we partic-

ularly focused on providing a comprehensive and comprehensible description of the measurement setup, including the identification of potential uncertainties.

Keywords

atmospheric boundary layer, atmospheric inflow, lidar, wake deflection, wind farm control

Content not included due to copyright restrictions. Please refer to the original article in *Wind Energy*.

Bromm et al. (2018): Bromm, M., Rott, A., Beck, H., Vollmer, L., Steinfeld, G. and Kühn, M. (2018). 'Field investigation on the influence of yaw misalignment on the propagation of wind turbine wakes.' In: *Wind Energy*, pp. 1–18. DOI: 10.1002/we.2210.

Content not included due to copyright restrictions. Please refer to the original article in *Wind Energy*.

Bromm et al. (2018): Bromm, M., Rott, A., Beck, H., Vollmer, L., Steinfeld, G. and Kühn, M. (2018). 'Field investigation on the influence of yaw misalignment on the propagation of wind turbine wakes.' In: *Wind Energy*, pp. 1–18. DOI: 10.1002/we.2210.

Content not included due to copyright restrictions. Please refer to the original article in *Wind Energy*.

Bromm et al. (2018): Bromm, M., Rott, A., Beck, H., Vollmer, L., Steinfeld, G. and Kühn, M. (2018). 'Field investigation on the influence of yaw misalignment on the propagation of wind turbine wakes.' In: *Wind Energy*, pp. 1–18. DOI: 10.1002/we.2210.

Content not included due to copyright restrictions. Please refer to the original article in *Wind Energy*.

Bromm et al. (2018): Bromm, M., Rott, A., Beck, H., Vollmer, L., Steinfeld, G. and Kühn, M. (2018). 'Field investigation on the influence of yaw misalignment on the propagation of wind turbine wakes.' In: *Wind Energy*, pp. 1–18. DOI: 10.1002/we.2210.

Content not included due to copyright restrictions. Please refer to the original article in *Wind Energy*.

Bromm et al. (2018): Bromm, M., Rott, A., Beck, H., Vollmer, L., Steinfeld, G. and Kühn, M. (2018). 'Field investigation on the influence of yaw misalignment on the propagation of wind turbine wakes.' In: *Wind Energy*, pp. 1–18. DOI: 10.1002/we.2210.

Content not included due to copyright restrictions. Please refer to the original article in *Wind Energy*.

Bromm et al. (2018): Bromm, M., Rott, A., Beck, H., Vollmer, L., Steinfeld, G. and Kühn, M. (2018). 'Field investigation on the influence of yaw misalignment on the propagation of wind turbine wakes.' In: *Wind Energy*, pp. 1–18. DOI: 10.1002/we.2210.

Content not included due to copyright restrictions. Please refer to the original article in *Wind Energy*.

Bromm et al. (2018): Bromm, M., Rott, A., Beck, H., Vollmer, L., Steinfeld, G. and Kühn, M. (2018). 'Field investigation on the influence of yaw misalignment on the propagation of wind turbine wakes.' In: *Wind Energy*, pp. 1–18. DOI: 10.1002/we.2210.

Content not included due to copyright restrictions. Please refer to the original article in *Wind Energy*.

Bromm et al. (2018): Bromm, M., Rott, A., Beck, H., Vollmer, L., Steinfeld, G. and Kühn, M. (2018). 'Field investigation on the influence of yaw misalignment on the propagation of wind turbine wakes.' In: *Wind Energy*, pp. 1–18. DOI: 10.1002/we.2210.

Content not included due to copyright restrictions. Please refer to the original article in *Wind Energy*.

Bromm et al. (2018): Bromm, M., Rott, A., Beck, H., Vollmer, L., Steinfeld, G. and Kühn, M. (2018). 'Field investigation on the influence of yaw misalignment on the propagation of wind turbine wakes.' In: *Wind Energy*, pp. 1–18. DOI: 10.1002/we.2210.

Content not included due to copyright restrictions. Please refer to the original article in *Wind Energy*.

Bromm et al. (2018): Bromm, M., Rott, A., Beck, H., Vollmer, L., Steinfeld, G. and Kühn, M. (2018). 'Field investigation on the influence of yaw misalignment on the propagation of wind turbine wakes.' In: *Wind Energy*, pp. 1–18. DOI: 10.1002/we.2210.

Content not included due to copyright restrictions. Please refer to the original article in *Wind Energy*.

Bromm et al. (2018): Bromm, M., Rott, A., Beck, H., Vollmer, L., Steinfeld, G. and Kühn, M. (2018). 'Field investigation on the influence of yaw misalignment on the propagation of wind turbine wakes.' In: *Wind Energy*, pp. 1–18. DOI: 10.1002/we.2210.

Content not included due to copyright restrictions. Please refer to the original article in *Wind Energy*.

Bromm et al. (2018): Bromm, M., Rott, A., Beck, H., Vollmer, L., Steinfeld, G. and Kühn, M. (2018). 'Field investigation on the influence of yaw misalignment on the propagation of wind turbine wakes.' In: *Wind Energy*, pp. 1–18. DOI: 10.1002/we.2210.

Content not included due to copyright restrictions. Please refer to the original article in *Wind Energy*.

Bromm et al. (2018): Bromm, M., Rott, A., Beck, H., Vollmer, L., Steinfeld, G. and Kühn, M. (2018). 'Field investigation on the influence of yaw misalignment on the propagation of wind turbine wakes.' In: *Wind Energy*, pp. 1–18. DOI: 10.1002/we.2210.

Content not included due to copyright restrictions. Please refer to the original article in *Wind Energy*.

Bromm et al. (2018): Bromm, M., Rott, A., Beck, H., Vollmer, L., Steinfeld, G. and Kühn, M. (2018). 'Field investigation on the influence of yaw misalignment on the propagation of wind turbine wakes.' In: *Wind Energy*, pp. 1–18. DOI: 10.1002/we.2210.

Content not included due to copyright restrictions. Please refer to the original article in *Wind Energy*.

Bromm et al. (2018): Bromm, M., Rott, A., Beck, H., Vollmer, L., Steinfeld, G. and Kühn, M. (2018). 'Field investigation on the influence of yaw misalignment on the propagation of wind turbine wakes.' In: *Wind Energy*, pp. 1–18. DOI: 10.1002/we.2210.

Content not included due to copyright restrictions. Please refer to the original article in *Wind Energy*.

Bromm et al. (2018): Bromm, M., Rott, A., Beck, H., Vollmer, L., Steinfeld, G. and Kühn, M. (2018). 'Field investigation on the influence of yaw misalignment on the propagation of wind turbine wakes.' In: *Wind Energy*, pp. 1–18. DOI: 10.1002/we.2210.

Content not included due to copyright restrictions. Please refer to the original article in *Wind Energy*.

Bromm et al. (2018): Bromm, M., Rott, A., Beck, H., Vollmer, L., Steinfeld, G. and Kühn, M. (2018). 'Field investigation on the influence of yaw misalignment on the propagation of wind turbine wakes.' In: *Wind Energy*, pp. 1–18. DOI: 10.1002/we.2210.

Content not included due to copyright restrictions. Please refer to the original article in *Wind Energy*.

Bromm et al. (2018): Bromm, M., Rott, A., Beck, H., Vollmer, L., Steinfeld, G. and Kühn, M. (2018). 'Field investigation on the influence of yaw misalignment on the propagation of wind turbine wakes.' In: *Wind Energy*, pp. 1–18. DOI: 10.1002/we.2210.

Content not included due to copyright restrictions. Please refer to the original article in *Wind Energy*.

Bromm et al. (2018): Bromm, M., Rott, A., Beck, H., Vollmer, L., Steinfeld, G. and Kühn, M. (2018). 'Field investigation on the influence of yaw misalignment on the propagation of wind turbine wakes.' In: *Wind Energy*, pp. 1–18. DOI: 10.1002/we.2210.

Content not included due to copyright restrictions. Please refer to the original article in *Wind Energy*.

Bromm et al. (2018): Bromm, M., Rott, A., Beck, H., Vollmer, L., Steinfeld, G. and Kühn, M. (2018). 'Field investigation on the influence of yaw misalignment on the propagation of wind turbine wakes.' In: *Wind Energy*, pp. 1–18. DOI: 10.1002/we.2210.

Content not included due to copyright restrictions. Please refer to the original article in *Wind Energy*.

Bromm et al. (2018): Bromm, M., Rott, A., Beck, H., Vollmer, L., Steinfeld, G. and Kühn, M. (2018). 'Field investigation on the influence of yaw misalignment on the propagation of wind turbine wakes.' In: *Wind Energy*, pp. 1–18. DOI: 10.1002/we.2210.

Content not included due to copyright restrictions. Please refer to the original article in *Wind Energy*.

Bromm et al. (2018): Bromm, M., Rott, A., Beck, H., Vollmer, L., Steinfeld, G. and Kühn, M. (2018). 'Field investigation on the influence of yaw misalignment on the propagation of wind turbine wakes.' In: *Wind Energy*, pp. 1–18. DOI: 10.1002/we.2210.

Content not included due to copyright restrictions. Please refer to the original article in *Wind Energy*.

Bromm et al. (2018): Bromm, M., Rott, A., Beck, H., Vollmer, L., Steinfeld, G. and Kühn, M. (2018). 'Field investigation on the influence of yaw misalignment on the propagation of wind turbine wakes.' In: *Wind Energy*, pp. 1–18. DOI: 10.1002/we.2210.

Content not included due to copyright restrictions. Please refer to the original article in *Wind Energy*.

Bromm et al. (2018): Bromm, M., Rott, A., Beck, H., Vollmer, L., Steinfeld, G. and Kühn, M. (2018). 'Field investigation on the influence of yaw misalignment on the propagation of wind turbine wakes.' In: *Wind Energy*, pp. 1–18. DOI: 10.1002/we.2210.

Content not included due to copyright restrictions. Please refer to the original article in *Wind Energy*.

Bromm et al. (2018): Bromm, M., Rott, A., Beck, H., Vollmer, L., Steinfeld, G. and Kühn, M. (2018). 'Field investigation on the influence of yaw misalignment on the propagation of wind turbine wakes.' In: *Wind Energy*, pp. 1–18. DOI: 10.1002/we.2210.

Content not included due to copyright restrictions. Please refer to the original article in *Wind Energy*.

Bromm et al. (2018): Bromm, M., Rott, A., Beck, H., Vollmer, L., Steinfeld, G. and Kühn, M. (2018). 'Field investigation on the influence of yaw misalignment on the propagation of wind turbine wakes.' In: *Wind Energy*, pp. 1–18. DOI: 10.1002/we.2210.

Content not included due to copyright restrictions. Please refer to the original article in *Wind Energy*.

Bromm et al. (2018): Bromm, M., Rott, A., Beck, H., Vollmer, L., Steinfeld, G. and Kühn, M. (2018). 'Field investigation on the influence of yaw misalignment on the propagation of wind turbine wakes.' In: *Wind Energy*, pp. 1–18. DOI: 10.1002/we.2210.

2.4 Conclusion

In this article, we presented the field measurements of the wake flow of a 3.5 MW wind turbine for different degrees of yaw misalignment. A setup comprising two long-range lidar devices was employed for capturing the inflow and wake flow of the test turbine. An eddy covariance stations was used for characterizing the atmospheric boundary layer at the site, and the inflow and turbine orientation were aligned using GPS devices and a laser scanner.

Based on the recorded measurements, we demonstrated that in neutrally stratified boundary layers, the wake trajectories of a yaw misaligned wind turbine deviate on average from the overall hub height inflow direction. For positive yaw offsets of the turbine, a lateral offset of the wake trajectory toward the downstream left-hand side of the turbine was observed. In the cases of negative yaw offsets, the wake trajectory was shifted toward the downstream right-hand side. Furthermore, larger absolute yaw offsets corresponded to larger lateral wake offsets in the investigated yaw offset range from -20° to 20° , with the maximum values reaching approximately $0.2D$.

The wake trajectories were determined based on the minimum of the power-based rotor equivalent wind speed at each downstream distance. This approach focuses on the impact of the wake flow on downstream wind turbines and is less dependent on the specific wake characteristics than methods that describe a wake by curve fitting or by tracking the maximum deficit. In the case of deflected wakes, this is of particular importance due to their asymmetric cross sections.

Investigating the wake development of full-scale wind turbines is still considered state-of-the-art research and is undergoing rapid development. At the same time, there is an urgent need for high-quality measurement data for the quantitative validation of simulation models. Therefore, a thorough documentation of all practical and technical aspects of a measurement campaign is required, including the estimation of uncertainties due to sensor accuracy and alignment.

Within the scope of our research, we critically assessed several aspects of field campaigns that could affect the quality of the results. This includes investigations focusing on the precision of the SCADA signal of the turbine orientation, the ability to determine the inflow direction, and the impacts of nacelle movement and lidar positioning on nacelle-based long-range lidar measurements. Considering all these aspects, we concluded that wake deflection based on yaw misalignment of the wind turbine was successfully applied in the field. Up to a downstream distance of approximately $3D$, it was possible to track and quantify the wake deflection at hub height with reasonable

accuracy. Beyond this distance, the measured wake trajectories of the yawed turbine were increasingly affected by the slight downward tilt of the scanning lidar. This effect was investigated by means of highly resolved large-eddy simulations of a wind turbine under comparable ambient conditions that proved valuable for enhancing our understanding of the field measurements.

Despite the successful application of wake tracking in the field, the authors see several aspects that need to be investigated in further campaigns. Additional measurement data is particularly required. Furthermore, it is desirable to directly investigate the impact of the deflected wakes on downstream turbines for various turbine layouts and atmospheric stability conditions.

Since the introduction of lidar technology for velocity measurements of the flow around wind turbines, its availability to the scientific community and industry has increased continuously. Despite the already gathered practical experiences, the investigation and characterization of the wake development of individual full-scale turbines or even wind farms remains challenging, mainly due to complex and dynamically changing ambient conditions and limited campaign durations. Because field data is frequently demanded as a reference for a qualitative and preferably a quantitative validation of simulation model results, a comprehensive and comprehensible documentation of all aspects of a measurement campaign, including the potential uncertainties, is required. Unfortunately, no common guidelines or suggestions currently exist for measurement procedures and post-processing routines. Different methods and the complexity of current field campaigns tend to reduce the comparability of the data, make it difficult to assess the quality of the data, and increase the risk that relevant aspects are not taken into account. Therefore, the authors are convinced that closer cooperation between researchers would help to better exploit the full potential of field measurements.

Acknowledgement

This work was partially funded by the Federal Ministry for Economic Affairs and Energy (BMWi) according to a resolution by the German Federal Parliament (projects *CompactWind*, FKZ 0325492B and *DFWind - Phase 1*, FKZ 0325936C). We wish to thank *eno energy systems GmbH*, our partner in the *CompactWind* project and operator of the wind farm, for their cooperation and commitment. In addition, we would like to thank our colleague Stephan Voß for his major role in the practical planning of the campaign and his work at the site, which enabled the smooth operation of all the measurement systems throughout the entire campaign. Finally, we would like to acknowledge our

colleagues Marijn Floris van Dooren and Anantha Padmanabhan Kidambi Sekar who provided the *SpinnerLidar* measurements. This data was obtained in the scope of the *ventus efficiens* project through the funding initiative *Niedersächsisches Vorab* of the Ministry for Science and Culture of Lower Saxony.

Chapter 3

Numerical investigation on the influence of wake deflection control on the power yield and loading of wind turbines in a wind farm

3.1 Introduction

The annual energy yield of a wind turbine is the most important parameter when it comes to optimising its operation and increasing its economic efficiency. A financial gain or loss, e.g. caused by some control action or wind farm layout adaptation, can easily be determined once the corresponding changes in the annual energy yield are understood. This becomes more difficult when considering structural loads. For this reason and because of only a limited availability of load information, wind farm optimisations are often carried out just based on the power yield and simple generic load models (e.g. Frandsen and Thøgersen (1999)). However, high fatigue loads can lead to performance losses over time or a reduced operational lifetime. Therefore, neglecting the load aspect complicates the transfer of new control concepts to industrial application, as operators are understandably hesitant if the impact of a technology is not fully understood.

Since it is possible to determine realistic atmospheric boundary layer wind fields with large-eddy simulations (Breton et al. (2017) and Mehta et al. (2014)), it seems obvious to use such wind fields to estimate the structural loads of a wind turbine for different inflow conditions. Unfortunately, the applicability of large-eddy simulations still is limited because of the high computational demands.

In this chapter, results from an approach that we refer to as wake mapping are presented. The method represents our attempt to benefit from the advantages of realistic large-eddy atmospheric boundary layer wind fields whilst still being able to carry out a large number of simulations for a variety of wake situations. By using the large-eddy wind fields as a basis for subsequent aeroelastic simulations, power yield and loading of a downstream wind turbine were determined and also set in relation to the ones of the upstream turbine for many different types of wake conditions. The upstream turbine was operating in normal operation as well as under yaw misalignment. Using two exemplary wind farm layouts and well-defined boundary conditions, it was estimated how the application of wake deflection through yaw misalignment affects the loading of the individual wind turbines in the wind farms.

An overview of the current state-of-the-art of wake deflection research and possibilities of large-eddy simulations are given in Chapter 1, Section 1.2.

3.2 Methods

3.2.1 Simulation approach - wake mapping

In this section, the general simulation approach that we refer to as wake mapping is briefly introduced (Figure 3.1). Furthermore, a few general guidelines on how to interpret the results of the investigation are defined. Detailed information on all individual aspects of the analysis is given in the following subsections.

Wake mapping is an attempt to obtain power and load information for wind turbines in a variety of wake situations based on realistic boundary layer wind fields without the disadvantages of extensive large-eddy simulations. In step one, a large-eddy simulation is performed to determine the wake flow of a single wind turbine for specific ambient conditions and a given operating point. In a second step, wind fields are extracted from the obtained flow for several downstream positions. These are then used as inputs for aeroelastic simulations to determine the power yield and loading of a virtual second turbine that is located at these different downstream positions and therefore exposed to different partial and full wake conditions. The obtained relations between the various analysed downstream positions and the corresponding power and load information are referred to as power and load maps. An advantage of this approach is that for a given setup, a large number of different wake conditions of a downstream turbine can be investigated at relatively small computational costs in comparison to other methods, which rely on extensive large-eddy simulations with embedded aerodynamic simulations. In this work, five large-eddy reference cases, with mean hub

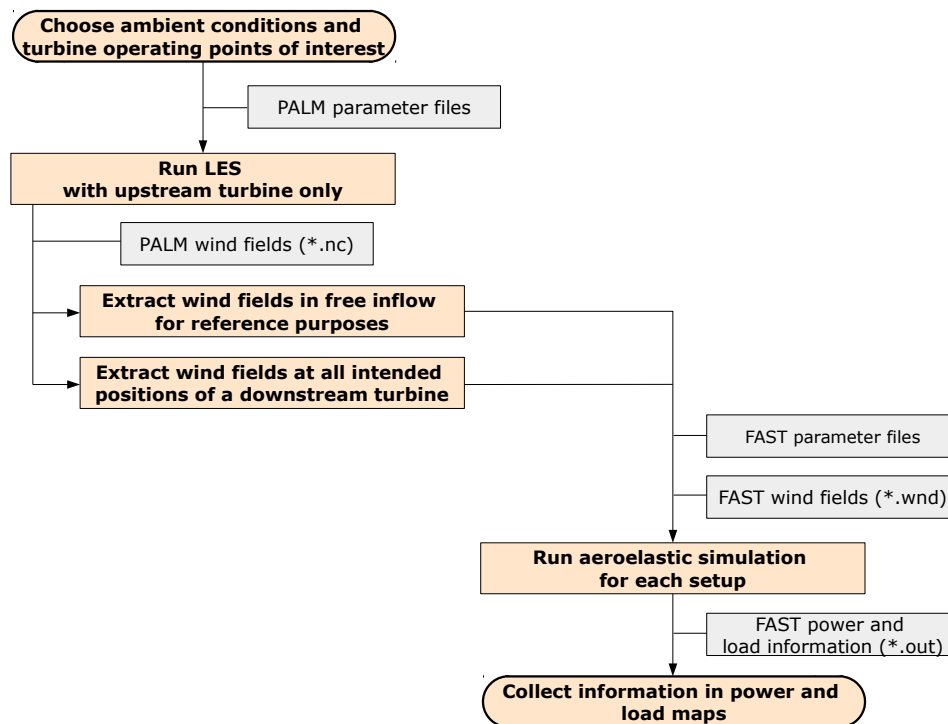


Figure 3.1: Flow chart of the wake mapping procedure to outline the individual steps

height wind speeds of 6 ms^{-1} to 14 ms^{-1} and a simulation time of 3600 s each, were analysed. This covers most of the partial and the lower full load range of the reference turbine.

In order to improve the understanding of individual aspects of the wake mapping approach and to ensure the quality and informative value of the results, we performed several comparisons with state-of-the-art methods to determine and estimate potential deviations and uncertainties. This includes how the limited frequency range of large-eddy wind fields influences the estimated turbine loading (Section 3.3.3) and how different ways of determining the power output of a turbine affect the results (Section 3.3.2).

In addition, we would like to point out that several assumptions were made in the investigation to account for influences that cannot be sufficiently represented with the available means. In particular, it is assumed that individual wind turbines and groups of wind turbines can be examined independently from the full wind farm. Any possible effects of downstream turbines on the approaching flow, e.g. due to blockage,

are neglected. Also globally developing wind farm flows, e.g. jets between rows of turbines, are not taken into account.

Additionally, recent investigations have indicated that small yaw offsets even at the turbine which is furthest downstream could possibly have a positive influence on the overall power yield and even loading of these turbines (Bartl et al. (2018)). However, in this study it is assumed that downstream wind turbines do not operate under yaw misalignment, as this would require a much higher number of large-eddy simulations to investigate how wakes interact with yawed turbines. Furthermore, it is still unclear to what extent very small, targeted yaw misalignments can be implemented in the field with the currently available technical possibilities and the exposure to highly dynamic inflow conditions.

For a clear and uniform representation of the results, a few guidelines are defined in the following. These apply unless explicitly stated otherwise. All two-dimensional vertical and horizontal flow fields, derived values and information on the turbine responses are presented as seen by an upstream observer or an observer who is located above the turbines. Figure 3.2 shows a conceptual visualization of the investigated turbine layouts with the origin of the $x - y$ coordinate system being located at the position of the upstream turbine. Distances are stated in multiples of the rotor diameter D . Velocity components in longitudinal x , lateral y and vertical z direction of the domain are referred to as u , v and w , respectively. While describing the wake characteristics, left and right refer to positive and negative y -values, respectively. A positive yaw misalignment, γ , indicates a clockwise rotation of the wind turbine when looked at from above. The main inflow direction is indicated by β . Due to inflow dynamics and the influence of wind veer, minor deviations do occur in the individual simulations. These are discussed in Section 3.2.4.1. The added underlying grid in all images has a spacing of $0.5D$ in downstream direction and $0.25D$ in lateral direction. In order to extract information about the undisturbed inflow of the simulated domain, a $5D$ wide $y - z$ reference plane R_{x_R} has been defined $4D$ in front of the upstream turbine at the longitudinal position of x_R . The plane extends over the entire height of the simulated domain.

3.2.2 Flow solver

For simulating the wake flow of a wind turbine, the *PALM* code (Maronga et al. (2015)) version 3.10 (r2412) was used. *PALM* is an open source large-eddy simulation model for atmospheric and oceanic flows and designed for performing on massively parallel computer architectures. It is based on the non-hydrostatic incompressible Boussinesq-approximated Navier-Stokes equations and the conservation equations of energy and

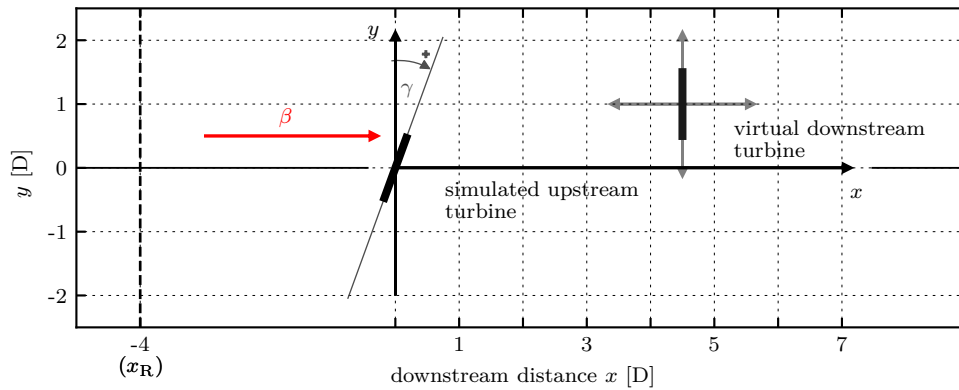


Figure 3.2: Conceptual visualisation of the investigated turbine layout for the clarification of the utilized nomenclature, variables, and orientation of the coordinate systems

mass.

All simulations with *PALM* were performed with its default model configuration. This includes a fifth-order scheme described by Wicker and Skamarock (2002) for solving the advection terms and an explicit third-order Runge-Kutta scheme for performing the integration in time. The Poisson equation for disturbance pressure, which follows from the constraint that the flow field has to be free from divergences, is either solved by Fast Fourier Transform in case of cyclic lateral boundary condition as they are used in the spin-up runs or else by a multigrid scheme (Section 3.2.4.1). For modelling the effects of subgrid scale turbulence on the resolved scale turbulence, *PALM* employs by default a 1.5th order closure following Deardorff (1980). Between the surface and the first computational grid point, Monin-Obukhov similarity theory (Monin and Obukhov (1954)) is used to obtain information on the turbulent fluxes at the bottom of the model domain. For a detailed and comprehensive description of all *PALM* options please refer to Maronga et al. (2015).

3.2.3 Turbine modelling

The wind turbine model, which was used in all simulations, is the conventional variable speed and variable pitch *NREL 5-MW* reference turbine including its baseline controller (Jonkman et al. (2009)). The turbine has a hub height (h_H) of 90 m and a 5° upward tilted rotor with a diameter (D) of 126 m. It reaches rated rotational speed of 12.1 rpm at a wind speed of 11.4 ms⁻¹.

In *PALM*, the *NREL 5-MW* turbine is implemented based on an enhanced actuator disc model with rotation (ADM-R) (Dörenkämper et al. (2015c) and Witha et al. (2014b)). With this approach, the rotor disk is divided into rotor annulus segments with varying

properties along the radial axis to represent the blade characteristics. Due to the clockwise rotation of the rotor, an azimuthal velocity is assigned to each of these segments. However, the absolute positions of all blade segments are fixed and time independent. Lift and drag coefficients of the blades and the local velocities at each segment are used to calculate the lift and drag forces. The forces are scaled for a three bladed turbine and are distributed onto the underlying grid. Singular behaviour is avoided by using a three-dimensional Gaussian regularization kernel to ensure the smoothness of the distribution. A variable-speed generator-torque controller and a pitch controller are implemented as described in Jonkman et al. (2009). The turbine's yaw angle can be freely chosen, for example to carry out investigations on the effects of yaw misalignment.

The aeroelastic response of the virtual downstream wind turbine was calculated with *FAST* v7.02 (Jonkman and Buhl, Jr. (2005)), an aeroelastic open source code specifically developed for horizontal axis wind turbines. In *FAST*, the turbines are modelled as a combination of rigid and flexible bodies and the aerodynamic forces along the blades are calculated by the AeroDyn module based on the blade element momentum theory (BEM) in combination with tabulated airfoil data and an external controller.

In *PALM* and *FAST*, the substructure as well as the geometry of the nacelle, the hub and the spinner are not modelled in detail. However, in *PALM* the effects of a generic nacelle and the tower on the wake flow development are considered through drag coefficients of 0.85 and 1.25, respectively.

3.2.4 Inflow conditions

Wind turbines operate in the atmospheric boundary layer whose properties can vary greatly depending on the specific type of sub-layer and thermal stratification. Large-eddy simulations are very well suited to generate realistic inflow conditions for wind turbines which reflect most of the underlying physics (Breton et al. (2017), Hertwig (2013) and Mehta et al. (2014)). However, the computational demands are generally high and especially heavily dependent on the number of grid points. Therefore, one usually chooses a grid resolution as coarse as possible. But besides its impact on the computational demand, the grid spacing acts as a filter and predetermines to what extent high-frequency fluctuations are present in the flow field.

In order to have reference values with which we can compare the loads obtained with our approach, we created stochastic wind fields with the commonly used TurbSim code. Such stochastic wind fields are widely used in the wind industry to perform aeroelastic load simulations. The stochastic wind fields obey Gaussian turbulence char-

acteristics and have similar statistical parameters (e.g. mean wind speed including vertical shear and turbulence intensity) as the ones from the large-eddy simulations. Despite their higher temporal resolution, they do not fully reflect the underlying physics and thus do not realistically represent the turbulent structures and the intermittency in the flow. A detailed description of both types of wind fields can be found in the following two sections.

3.2.4.1 Large-eddy simulation - PALM

To investigate the load mapping approach, we created five large-eddy wind fields of neutrally stratified atmospheric boundary layers that are referred to as *N06*, *N08*, *N10*, *N12* and *N14* based on the targeted mean wind speed at hub height. For obtaining the required conditions, 40-hour spin-up runs without model turbines were performed allowing the boundary layers to develop and converge at a quasi-equilibrium. Initialisation took place based on the stationary wind profiles obtained with a one-dimensional model incorporated in *PALM*. All simulations presented in this paper were performed in box-shaped domains on uniformly spaced Cartesian grids with a resolution of 5 m (Abkar and Porté-Agel (2015) and Allaerts and Meyers (2015)). The outer dimensions of the domain of the spin-up runs were approximately $40D \times 20D \times 6D$ ($L_x \times L_y \times L_z$). In all five cases, the potential temperature was set to 283.15 K within the first 500 m above the ground. Gradients of 8 K and 1 K per 100 m were chosen above heights of 500 m and 600 m, respectively. To damp potentially occurring gravity waves, Rayleigh damping above 700 m height was applied with a factor of 0.01. A roughness length of 0.002 m was chosen, typical for low turbulence conditions as for example featureless land or offshore (World Meteorological Organization (2008)). All setups were simulated for a latitude of 54 degree north. For establishing the desired atmospheric inflow conditions and for maintaining them throughout the simulations, different boundary conditions for the velocity were imposed on the outer limits of the simulation domains. They are summarized in Table 3.1. The boundary conditions of the potential temperature are of type Dirichlet at the bottom of the domain.

Once the reference wind fields were generated, simulations with one ADM-R model turbine were performed in an enlarged domain with a size of approximately $80D \times 20D \times 6D$ ($L_x \times L_y \times L_z$). These main runs lasted 3900 s and a fixed time step of 0.125 s was chosen, which is considerably smaller than the ones demanded by the CFL (Courant-Friedrichs-Lewy) condition (Courant et al. (1928)) and the diffusion criterion (Roache (1985)). The first 300 s were treated as a transient initialisation phase and discarded. The remaining 3600 s were divided into six 10 min time periods that we refer to as seeds (e.g. *N08-1* to *N08-6*). For later use in combination with variables, two indices c and s

Table 3.1: Imposed velocity boundary conditions for the performed simulations

	spin-up	main
Inlet	Cyclic	Dirichlet
Outlet	Cyclic	Radiation
Lateral	Cyclic	Cyclic
Bottom	Dirichlet	Dirichlet
Top	Dirichlet	Dirichlet

Table 3.2: Overview of the assignment of the two indices c and s to wind field case and seed. Index c refers to the wind field case $N06$ to $N14$ and runs from 1 to 5. Index s refers to the specific seed (10 min interval) of each reference case and runs from 1 to 6. In addition, a single index c is used to refer to the total 3600 s of an entire reference field.

		seed (s)							
		1	2	3	4	5	6	-	
case (c)	1	11	12	13	14	15	16	1	<i>N06</i>
	2	21	22	23	24	25	26	2	<i>N08</i>
	3	31	32	33	34	35	36	3	<i>N10</i>
	4	41	42	43	44	45	46	4	<i>N12</i>
	5	51	52	53	54	55	56	5	<i>N14</i>

are assigned to most variables for easy identification of the corresponding 10 min wind field seeds (Table 3.2). The two indices c and s indicate the wind field case and the seed, respectively. If only one index is specified, the variable refers to the entire reference field of 3600 s length. Longitudinal and lateral velocity components at a specific point in space and time of each of the individual seeds are referred to as $u_{cs}(x, y, z, t)$ and $v_{cs}(x, y, z, t)$, respectively.

Whereas in the five reference cases the turbine is aligned with the inflow direction, additional simulations with yaw misalignments γ of $\pm 10^\circ$ and $\pm 20^\circ$ were performed. They are based on *N08* so that the overall inflow characteristics of *N08* and these four simulations are identical. The results are used for the general investigation of the influence of yaw-based wake deflection on the loads of the involved wind turbines and applied in the test case scenario (see Section 3.2.7). The chosen γ values of $\pm 10^\circ$ and

$\pm 20^\circ$ were selected for the investigation because these average offsets could be implemented more easily in the field even under complex and dynamic inflow conditions compared to deliberate misalignments of only a few degrees.

Average characteristics of the full 3600 s time periods of the five reference cases are summarized in Table 3.3 and the corresponding profiles of the mean undisturbed longitudinal inflow velocity \hat{u}_c^P (Equation (3.1)), the longitudinal turbulence intensity TI_{u_c} (Equation (3.2-3.4)) and the mean inflow direction β_c (Equation (3.6)) are shown in Figure 3.3. All values were determined in the vertical reference plane R_{x_R} at position x_R from the full 8 Hz data sets. $|T|$ and $|Y|$ are the cardinality of the two sets T and Y (Equation (3.7) and (3.8)) which include all time steps of the simulation and all distinct positions of the grid points along the y -axis within the range of the R_{x_R} reference plane, respectively. The velocity \hat{u}_c^P was determined based on the cubic average to account for the influence of the wind on the power output of wind turbines. A z value of h_H refers to hub height of 90 m. Due to a very dominant inflow direction, β_c was determined based on the average longitudinal and lateral inflow profiles \hat{u}_{cs} (Equation (3.4)) and \hat{v}_{cs} (Equation (3.5)). In case of larger deviations of the inflow direction, directional statistics should be considered (Rott et al. (2018)). $\Delta\beta_c$ is the change in mean inflow direction between 30 m and 150 m height, which approximately corresponds to the full rotor range. Positive values indicate a clockwise rotation with increasing height, which one would expect in a barotropic atmosphere on the northern hemisphere because of the Coriolis force. The distributions of the inflow direction throughout the reference simulations are shown in Figure 3.4. They each were obtained from the 8 Hz time series of a point centred in the reference plane R_{x_R} upstream of the wind turbine. The values were assigned to bins with a width of 1° . For the assumption of a Gaussian distribution of the inflow directions, a standard deviation of 2.8° to 2.9° is obtained in each of the five cases.

The parameters u_g and v_g indicate the velocity components of the geostrophic wind.

Table 3.3: Characteristics of the five neutrally stratified atmospheric reference offshore boundary layers

case	$\hat{u}_c^P(h_H)$ (m/s)	$\mathbf{TI}_{u_c}(h_H)$ (%)	$\beta_c(h_H)$ (°)	$\Delta\beta_c$ (°)	$\mathbf{u}_g, \mathbf{v}_g$ (m/s)
N06	6.0	5.7	0.3	3.3	6.634, -1.350
N08	8.0	6.1	0.1	2.5	8.930, -2.010
N10	9.9	6.4	0.2	1.9	11.200, -2.770
N12	12.1	6.4	-0.1	1.7	13.720, -3.700
N14	14.0	6.5	0.3	1.4	16.290, -3.620

$$\hat{u}_{cs}^P(z) = \left(\frac{1}{|Y|} \sum_{y \in Y} \left(\frac{1}{|T|} \sum_{t \in T} |u_{cs}(x_R, y, z, t)|^3 \right) \right)^{\frac{1}{3}} \quad (3.1)$$

$$\mathbf{TI}_{u_{cs}}(z) = \frac{\sigma_{u_{cs}}(z)}{\hat{u}_{cs}(z)} \quad (3.2)$$

$$\sigma_{u_{cs}}(z) = \frac{1}{|Y|} \sum_{y \in Y} \left(\frac{1}{|T|} \sum_{t \in T} \left(u_{cs}(x_R, y, z, t) - \frac{1}{|T|} \sum_{t \in T} u_{cs}(x_R, y, z, t) \right)^2 \right)^{\frac{1}{2}} \quad (3.3)$$

$$\hat{u}_{cs}(z) = \frac{1}{|Y|} \sum_{y \in Y} \left(\frac{1}{|T|} \sum_{t \in T} u_{cs}(x_R, y, z, t) \right) \quad (3.4)$$

$$\hat{v}_{cs}(z) = \frac{1}{|Y|} \sum_{y \in Y} \left(\frac{1}{|T|} \sum_{t \in T} v_{cs}(x_R, y, z, t) \right) \quad (3.5)$$

$$\beta_{cs}(z) = -\arctan \left(\frac{\hat{v}_{cs}(z)}{\hat{u}_{cs}(z)} \right) \quad (3.6)$$

$$T := \{0 \text{ s}, 0.125 \text{ s}, \dots, T_{\max}\} \quad (3.7)$$

$$Y := \{-317.5 \text{ m}, -312.5 \text{ m}, \dots, 317.5 \text{ m}\} \quad (3.8)$$

For all six 10 min time periods of each reference case the average $\hat{u}_{cs}^P(h_H)$ differs less than 2% from the targeted wind speed. The homogeneity of the wind fields is further discussed in Section 3.3.1. The boundary conditions of the simulations with the turbine slightly differ from the spin-up runs and are included in Table 3.1. Turbulence recycling

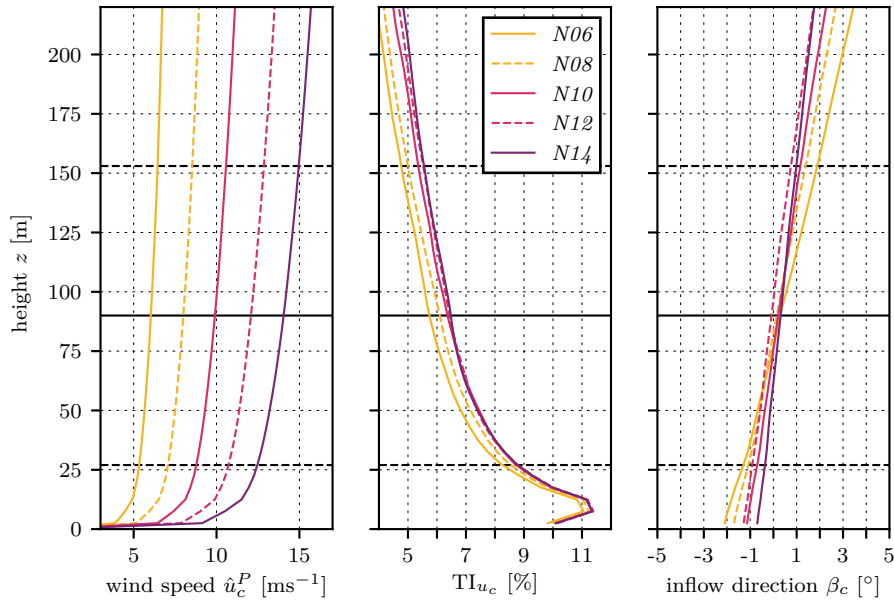


Figure 3.3: Undisturbed mean longitudinal inflow velocity \hat{u}_c^P (left), longitudinal turbulence intensity TI_{u_c} (centre) and mean inflow direction β_c (right) of the five large-eddy atmospheric boundary layer reference cases *N06-N14*. The rotor range and hub height of the *NREL 5-MW* turbine model used in the simulations are emphasized by horizontal dashed and solid lines, respectively.

(Lund et al. (1998)) was applied at a plane 40D downstream of the inlet to reduce the overall simulation time. At 48D downstream of the inlet, the upstream turbine was positioned. The large distances between the inlet, the recycling plane and the wind turbine were chosen so that the atmospheric turbulence has enough space to develop and that it is unaffected by disturbances that are being introduced by the turbine.

3.2.4.2 Extracted large-eddy wind fields

To perform the actual load mapping, we extracted the wind speed information from all seeds of each large-eddy reference simulation and converted it to the *.wnd* file format, which can be read by the aeroelastic simulation code *FAST*. For each file, this was done for 357 potential positions of a virtual downstream turbine at a lateral range from -2D to 2D with a spacing of 0.25D and a longitudinal range from 0D to 10D with a spacing of 0.5D were considered. For each time step of a *.wnd* file, the three-component velocity vectors are available at grid points in a vertical plane that is centred at hub height. We chose a grid size of 31x31 grid points, a grid spacing of 5 m and a time step of 0.125 s to fully cover the rotor area and match the spatial and temporal resolutions of the large-eddy simulation. Since in the *FAST* simulations a time step of 0.02 s was chosen, *FAST* performs a linear interpolation between the individual vertical velocity

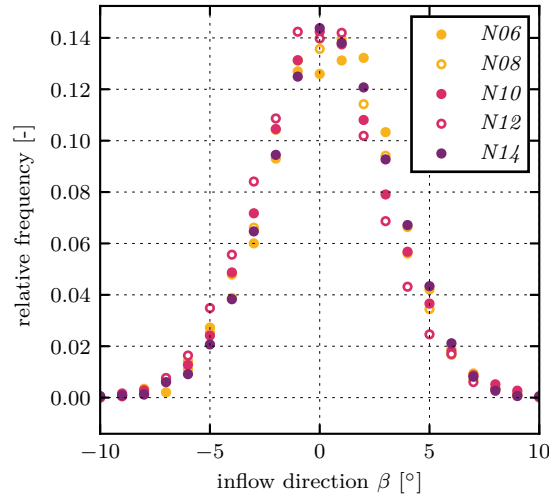


Figure 3.4: Distribution of the inflow direction of the large-eddy reference wind fields at hub height, obtained from the 8 Hz time series of a point centred in the reference plane R_{xR} upstream of the wind turbine. The bin width is 1° .

slices of the *.wnd* input file during the simulation.

In addition to the wind fields intended for load mapping, further wind fields of undisturbed inflow were extracted from all large-eddy seeds in the reference plane R_{xR} at the seven lateral positions Y_F ranging from $-1.5D$ to $1.5D$ (Equation (3.9)). This was done for two reasons. Firstly, we use the power and load information obtained from the extracted wind fields to compare them with those of stochastic wind fields (Section 3.2.4.3) that have comparable statistical characteristics to the large-eddy wind fields (Sections 3.3.2.1 and 3.3.3.1). Secondly, it allows us to investigate to what extent the characteristics of the large-eddy wind fields are homogeneous across the inflow of the simulation domain (Section 3.3.2.1).

$$Y_F := \{-1.5D, -1D, \dots, 1.5D\} \quad (3.9)$$

3.2.4.3 Stochastic simulation - *TurbSim*

In large-eddy simulations, the presence of high-frequency fluctuations is limited by the grid resolution. To get an idea of how a reduced frequency range might affect our turbine load information, additional investigations with higher resolution stochastic wind fields were performed. We would like to point out that the comparison is not a conclusive investigation and has more of an indicative character. One reason for this is that stochastic wind fields do not account for the underlying physics of the atmospheric boundary layer. Turbulent structures are therefore not realistically represented.

In a first step, six stochastic baseline wind fields were generated for each large-eddy

reference case seed. They are named in analogy to the large-eddy reference wind fields (e.g. *S08-1* to *S08-6*). For the stochastic wind fields, the same spatial resolution of 5 m and a grid size of 31x31 points were chosen as for the extracted LES wind fields. Previous investigations have confirmed that this resolution is sufficient for load analysis with the NREL turbine model (Sim et al. (2012)). The time step of the *FAST* simulation was set to 0.031 25 s (32 Hz).

To generate these stochastic wind fields, the *TurbSim* code (Jonkman (2009)) was used (Appendix 3.A, Listing 3.1). The Kaimal spectral model and the IEC Normal Turbulence Model were chosen with the turbulence intensity being scaled according to IEC-61400-1, 3rd edition (IEC (2005), Jonkman (2009) and Kaimal et al. (1972)).

For meaningful results, it was our goal to obtain the best possible match between the statistical inflow characteristics of the *TurbSim* wind fields and the average undisturbed inflow of the large-eddy reference case seeds. The latter was determined in the reference plane R_{xR} , 4D upstream of the turbine. The level of the turbulence intensity was chosen according to the hub height average of the undisturbed inflow of each large-eddy simulation seed. To ensure the desired turbulence intensity in the stochastic wind fields, a scaling of the wind speed time series at each grid point was performed by *TurbSim* (input parameter $ScaleIEC=2$) which slightly affects the coherence between individual grid points.

To obtain the desired inflow profiles, *TurbSim's* option to define the mean longitudinal inflow profile based on the power law approach (Equation (3.10)) was chosen. The three parameters of reference wind speed $u_{M,ref}$, reference height $h_{M,ref}$ and the power law exponent α were determined by optimisation. Our criterion for the optimisation was to minimise the sum of the cubed velocity differences of the averaged large-eddy inflow and the power law profiles for all data points within the rotor range (Equations (3.11, 3.12)).

$$u_M(z, u_{M,ref}, h_{M,ref}, \alpha) = u_{M,ref} \cdot \left(\frac{z}{h_{M,ref}} \right)^\alpha \quad (3.10)$$

$$\underset{u_{M,ref}, h_{M,ref}, \alpha}{\operatorname{argmin}} \left(\sum_{z \in Z} |u_M(z, u_{M,ref}, h_{M,ref}, \alpha) - \hat{u}_{cs}^P(z)|^3 \right)^{\frac{1}{3}} \quad (3.11)$$

$$Z := \{27.5 \text{ m}, 32.5 \text{ m}, \dots, 152.5 \text{ m}\} \quad (3.12)$$

In Figure 3.5a and Figure 3.5b, the average inflow profiles of the longitudinal velocity \hat{u}_{21}^P and the turbulence intensity $TI_{u_{21}}$ of the first seed of the *N08* reference case

and corresponding stochastic baseline wind field are compared, respectively. Additional graphs that are included in the figure represent further stochastic wind fields that were derived from the baseline ones and are characterised by a reduced frequency range. They are described at a later stage in this section. Within the rotor range, the average inflow profiles of the longitudinal velocity show a good agreement. At hub height, the turbulence intensity of the stochastic baseline wind fields matches the one from the large-eddy wind fields. However, above hub height the turbulence intensity from the stochastic wind fields is higher and below hub height lower than the one in the large-eddy wind fields. Furthermore, we would like to point out that the profiles of the turbulence intensity of the 10 min periods show a different curvature than the ones of the full 3600 s wind fields that were shown in Figure 3.3. This indicates that the 600 s observation period, which is commonly used in wind energy applications, is insufficient as relevant contributions of the atmospheric turbulence extend to larger time scales.

Interestingly, the optimisation led to the best matching profiles for an average h_{ref} of 142.8 m and an average α of 0.105. To verify the results, we determined the IEC rotor equivalent wind speed (REWS) (IEC (2017)) for the power law and large-eddy simulation profiles. In all cases, the REWS of the power law profiles differs by less than 0.15 % from the LES profiles. An intended optimisation directly based on the IEC REWS did not result in satisfactory results. Even strongly deviating profiles can lead to the same REWS, which results in the optimisation not converging to the desired profiles. With a more sensible choice of solver and boundary conditions, this issue could probably be avoided. Since in our opinion the approach used only led to negligible differences between the targeted and the obtained profiles we refrained from further investigations. In addition, *TurbSim* does not allow providing profiles for the v -component of the wind speed. Due to the presence of only a small amount of wind veer no attempt of including a mean profile for the lateral wind speed was made.

In order to draw substantial conclusions from the load analysis, it is important to understand what one can expect based on the available inflow data. From the 32 Hz stochastic baseline wind fields, further wind fields with a reduced frequency range of all three velocity components u , v and w were derived to investigate how the results of the load simulations are affected by these fluctuations. The filtered wind fields were obtained by decimation, which includes the application of a low-pass filter to reduce high-frequency components and a subsequent downsampling (IEEE Acoustics, Speech, and Signal Processing Society. Digital Signal Processing Committee (1979)). The filtering was done with an 8th order Chebyshev low-pass filter with cut-off fre-

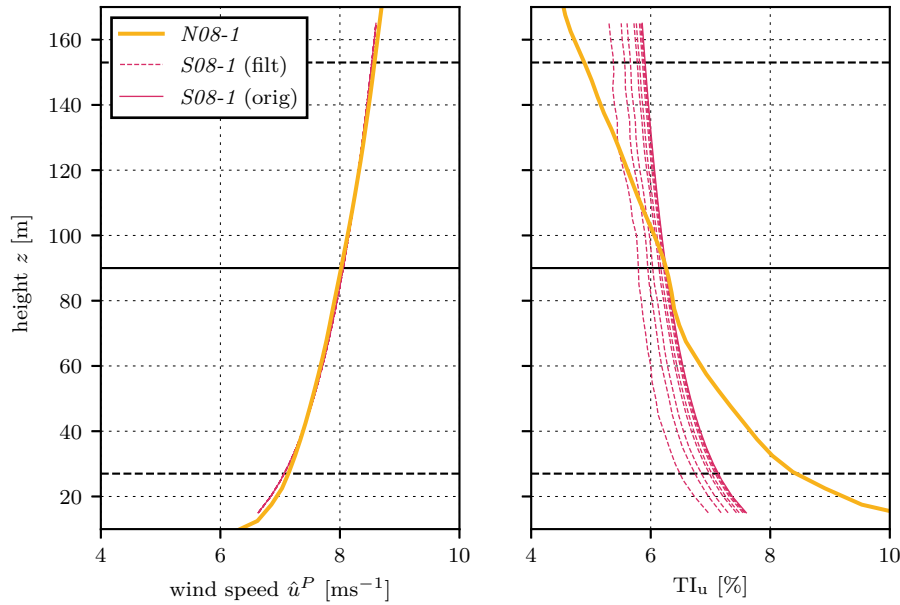


Figure 3.5: Comparison of the (a) average undisturbed longitudinal inflow velocity profile \hat{u}^P and (b) average turbulence intensity profiles TI_u of the first seed of the large-eddy reference simulation *N08-1* and the corresponding stochastic baseline and filtered *TurbSim* wind fields *S08-1*. The rotor range and hub height of the turbine model used in the simulations are emphasized by horizontal dashed and solid lines, respectively.

frequencies of 16 Hz, 8 Hz, 4 Hz, 2 Hz, 1 Hz, 1/2 Hz, 1/4 Hz, and 1/8 Hz.

No effect of the filtering on the average inflow of the stochastic wind fields was determined (Figure 3.5a). However, due to the filtering a small reduction in turbulence intensity does occur at all heights (Figure 3.5b).

In Figure 3.6, the power spectral densities of the longitudinal velocity components $u_{21}(x_R, Y_F, h_H, t)$ of the different wind fields of the *N08-1* case are compared. The spectrum labelled *LES (fixed)* is the average power spectral density of the longitudinal inflow velocity components $u_{21}(x_R, Y_F, h_H, t)$. It was calculated by averaging the spectra obtained at the seven lateral positions Y_F at hub height h_H within the reference plane R_{x_R} of the first seed of the reference case *N08*. Furthermore, the spectra of the corresponding baseline and filtered stochastic wind fields are shown in the graph. Also, the Kolmogorov -5/3 power law for the scaling of turbulence in the inertial subrange is included as a reference. All spectra in this work were determined with the Multitaper algorithm (Thomson (1982)).

Due to the filtering, the spectra of the stochastic wind fields show a lack of energy content at frequencies higher than the corresponding Nyquist frequency as one would expect. Overall, in the frequency range under consideration, the spectra of the wind

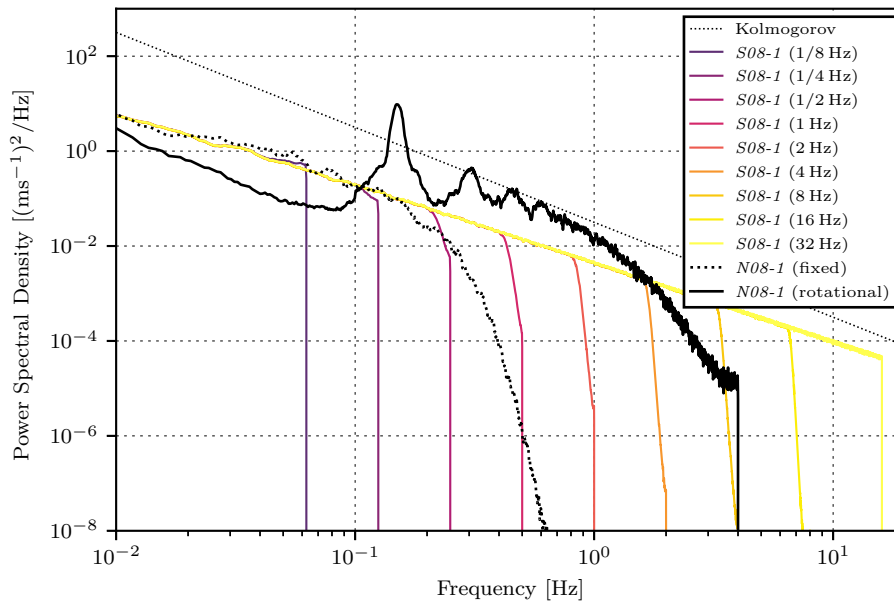


Figure 3.6: Comparison of the average spectrum of the longitudinal velocity components $u_{21}(x_R, Y_F, h_H, t)$ of reference wind field *N08-1* and the corresponding baseline and filtered stochastic wind fields *S08-1*. In addition, the averaged rotationally sampled spectrum of a point at $2/3$ of the blade radius is shown which was obtained for the same turbine positions as the spectrum for the fixed point. The Kolmogorov $-5/3$ power law for the scaling of turbulence in the inertial sub-range is shown for reference.

fields have a slightly less steep slope than the Kolmogorov power law indicates. For lower frequencies, the fixed point large-eddy spectrum corresponds with the spectra of the stochastic wind fields. At frequencies above approximately 0.1 Hz a reduction of the energy content is noticeable that can be attributed to a limited spatial resolution. However, when it comes to the analysis of structural loads, spectra of fixed points in time do not show the whole picture. Due to the movement of the blades, a rotational sampling of the inflow takes place (Connell (1981), Hardesty and Weber (1987)). Therefore, in addition to the fixed-point spectrum, the spectrum that was obtained from a time series of a moving reference point at $2/3$ of the blade radius is shown in Figure 3.6. *FAST* simulations were performed to generate a representative time series of the azimuth angle of the turbine rotor. The inflow conditions were extracted from the large-eddy simulation with the centre of the rotor being at the same positions (x_R, Y_F) as for the fixed-point analysis. The rotor azimuth angle was read from the *FAST* .out file and the wind speed at the position of the moving reference point at any given time was interpolated from the wind field data.

A distinct difference from the rotationally sampled spectrum with respect to the fixed

point in space spectrum is the prominent peak at the rotational speed of the turbine rotor. Further less prominent peaks can be found at multiples of this frequency. Yet another difference is the overall energy shift, which is observed from lower frequencies to higher frequencies.

3.2.5 Power output

To determine the power of a virtual downstream turbine, two different methods were investigated and compared.

In the first approach, a *FAST* simulation (Appendix 3.A, Listings 3.2, 3.3) with the corresponding wind field extracted from the large-eddy simulation (see Section 3.2.4.2) was performed for each assumed position of the virtual downstream turbine to obtain the *FAST* power output *RotPwr*. The 10 min average of each power time series is referred to as $P_{cs}^{\text{FAST}}(x, y, \gamma)$ with γ indicating the yaw misalignment of the upstream turbine. If the investigated turbine is the upstream turbine that is in free inflow than γ is referring to its own yaw misalignment. The 60 s prior to each investigated 600 s time period were included in the simulations but discarded during the analysis to account for the transient startup phase of each simulation.

The power that is obtained from *FAST* simulations with the stochastic wind fields is referred to as P_{cs}^{STO} .

$$A_{x,y} = \left\{ (\mathbf{x}, \mathbf{y}, \mathbf{z}) \mid \left((\mathbf{y} - y)^2 + (\mathbf{z} - h_H)^2 \right)^{\frac{1}{2}} \leq \frac{D}{2}, \mathbf{x} = x, \mathbf{y} \in Y, \mathbf{z} \in Z \right\} \quad (3.13)$$

$$\bar{u}_{cs}(x, y) = \left(\frac{1}{|A_{x,y}|} \sum_{\mathbf{x}, \mathbf{y}, \mathbf{z} \in A_{x,y}} \left(\frac{1}{|T|} \sum_{t \in T} |u_{cs}(\mathbf{x}, \mathbf{y}, \mathbf{z}, t)|^3 \right) \right)^{\frac{1}{3}} \quad (3.14)$$

In the second approach, the power-based rotor equivalent wind speed (REWS) $\bar{u}_{cs}(x, y)$ (Equation (3.14)) was determined for each potential turbine position x, y based on the longitudinal velocity components $u_{cs}(\mathbf{x}, \mathbf{y}, \mathbf{z}, t)$ of the large-eddy wind fields, following the examples of Schlipf et al. (2013) and Vollmer et al. (2016). A rotor diameter of 126 m was chosen equal to the one of the wake-generating *NREL 5-MW*. For the calculation, at each turbine position all grid points within the rotor area $A_{x,y}$ were considered and equally weighted. Using the REWS value and the laminar power curve of the *NREL 5-MW* turbine (Table 3.4), the power $P_{cs}^{\text{REWS}}(x, y)$ of the downstream turbine was determined. The power curve was obtained by performing *FAST* simulations with homogeneous and uniform inflow conditions for the wind speeds stated in Table 3.4. All values in between were obtained through shape-preserving piecewise cubic inter-

Table 3.4: Reference power curve obtained through *FAST* simulations with homogeneous and uniform inflow conditions.

wind speed	power*
(ms^{-1})	(kW)
3.0	47
4.0	194
5.0	438
6.0	804
7.0	1300
8.0	1938
9.0	2747
10.0	3751
11.0	4958
11.4	5274

* *RotPwr*

polation. The model parameters were identical to the ones that were used when the simulations with the extracted LES wind fields were performed. We are aware that the power curve for turbulent inflow conditions does deviate, especially near the rated wind speed, from the chosen one for laminar conditions. Nevertheless, the latter was chosen for reproducibility and comparability reasons. A power curve that was determined for conditions more similar to the investigated ones most likely results in more accurate estimations. Unfortunately, this would also increase the complexity of the currently relatively simple approach, which has a significantly lower computational effort in comparison to a *FAST* based power mapping. However, if a load mapping analysis of the structural turbine loads is intended, *FAST* simulations are required anyhow (see Section 3.2.6).

In the further course of the analysis, a normalisation of the power maps is intended for a comparison of the results between different inflow conditions. Furthermore, reference power outputs for turbines in the undisturbed inflow of the reference cases are required for the application of the wake mapping in the test case scenario (Section 3.2.7). The reference power output $\tilde{P}_c^{\text{FAST}}(\gamma)$ (Equation (3.15)) of the upstream turbine in undisturbed inflow is a single reference value that only depends on the yaw

Table 3.5: Reference power $\tilde{P}_c^{\text{FAST}}(\gamma)$ and loading information $\tilde{L}_c^{\text{FAST}}(\gamma)$ of the sensors EB, FB, TS and TF of a wind turbines operating in free inflow of the reference wind fields *N06* to *N14* without yaw misalignment ($\gamma = 0^\circ$).

case	$\tilde{P}_c^{\text{FAST}}$ (kW)	EB (kN·m)	FB (kN·m)	TS (kN·m)	TF (kN·m)
<i>N06</i>	768	5834	953	1282	4046
<i>N08</i>	1834	5994	1590	1213	3740
<i>N10</i>	3441	6168	2446	954	3872
<i>N12</i>	5250	6296	3766	2007	6849
<i>N14</i>	5297	6150	3499	2102	5224

misalignment of the turbine chosen in the *FAST* simulation (Table 3.5). It is the average of the 42 power outputs obtained with *FAST* from the large-eddy wind fields at the seven lateral positions Y_F in the reference plane R_{x_R} of all six 10 min seeds for each of the five reference cases *N06* to *N14*. The reference load information also included in Table 3.5 are further described in Section 3.2.6.

For the optimisation of the yaw misalignment in the test case scenario, the power outputs for a wind turbine that operates under yaw misalignments of $\pm 10^\circ$ and $\pm 20^\circ$ in relation to the case without yaw misalignment ($\gamma = 0^\circ$) is required (Equation (3.16)). These reference power ratios for the yaw misaligned cases of *N08* are listed in Table 3.6. According to the simulations, yaw misalignments of $\pm 10^\circ$ lead to a power loss of 4 % whereas for $\pm 20^\circ$, losses of 16 % are expected. Again, the corresponding load information, which are described in Section 3.2.6, are included in the table.

$$\tilde{P}_c^{\text{FAST}}(\gamma) = \frac{1}{6|Y_F|} \sum_{i=1}^6 \sum_{\mathbf{y} \in Y_F} P_{ci}^{\text{FAST}}(x_R, \mathbf{y}, \gamma) \quad (3.15)$$

$$\tilde{\rho}_c^{\text{FAST}}(\gamma) = \frac{\tilde{P}_c^{\text{FAST}}(\gamma)}{\tilde{P}_c^{\text{FAST}}(0^\circ)} \quad (3.16)$$

3.2.6 Structural turbine loading

An important aspect of this investigation is the analysis of the structural loads of a turbine in wake conditions. To obtain load information for a waked virtual downstream turbine, we performed aeroelastic simulations with the *FAST* code and used the wind

Table 3.6: Reference power ratio $\tilde{\rho}_c^{\text{FAST}}(\gamma)$ and load ratio $\tilde{\Lambda}_c^{\text{FAST}}(\gamma)$ of the load sensors EB, FB, TS and TF of a wind turbines operating under yaw misalignment ($\gamma \neq 0^\circ$) relative to the case without yaw misalignment ($\gamma = 0^\circ$) in free inflow conditions for the reference wind field *N08*.

γ ($^\circ$)	$\tilde{\rho}_c^{\text{FAST}}$ (-)	EB (-)	FB (-)	TS (-)	TF (-)
20	0.841	1.027	1.213	2.501	1.076
10	0.958	1.017	1.103	1.669	1.027
0	1.000	1.000	1.000	1.000	1.000
-10	0.960	0.979	1.060	1.299	1.004
-20	0.844	0.958	1.168	1.917	1.062

fields extracted from large-eddy simulations as input. In addition, we performed simulations of undisturbed inflow with the stochastic baseline wind fields, the filtered stochastic wind fields and the extracted wind fields from the large-eddy simulations to improve our understanding of the impact of inflow with a reduced frequency spectrum on turbine loads.

For being able to quantify and compare the structural loads, we determined the 1 Hz damage equivalent loads (DELs) with the rainflow cycle counting algorithm (ASTM E 1049-85 (2011)) for the edgewise blade root bending moment (EB, *RootMxb1*), the flap-wise blade root bending moment (FB, *RootMyb1*), the tower base side-to-side moment (TS, *TwrBsMxt*) and the tower base fore-aft moment (TF, *TwrBsMyt*). Wöhler exponents of 10 and 3 were chosen for the composite material of wind turbine blades and the steel tower, respectively.

The reference load values for a turbine in free stream conditions with and without wake deflection were determined according to Equations (3.17) and (3.18). L_{ci}^{FAST} is representing the DEL of the load sensor EB, FB, TF or TS and otherwise follows the behaviour of P_{ci}^{FAST} . In Equations (3.17), the Wöhler exponent m must be chosen in accordance with the load sensor. The results are also included in Table 3.5 and in Table 3.6.

$$\tilde{L}_c^{\text{FAST}}(\gamma) = \left(\frac{1}{6|Y_F|} \sum_{i=1}^6 \sum_{\mathbf{y} \in Y_F} (L_{ci}^{\text{FAST}}(x_R, \mathbf{y}, \gamma))^m \right)^{\frac{1}{m}} \quad (3.17)$$

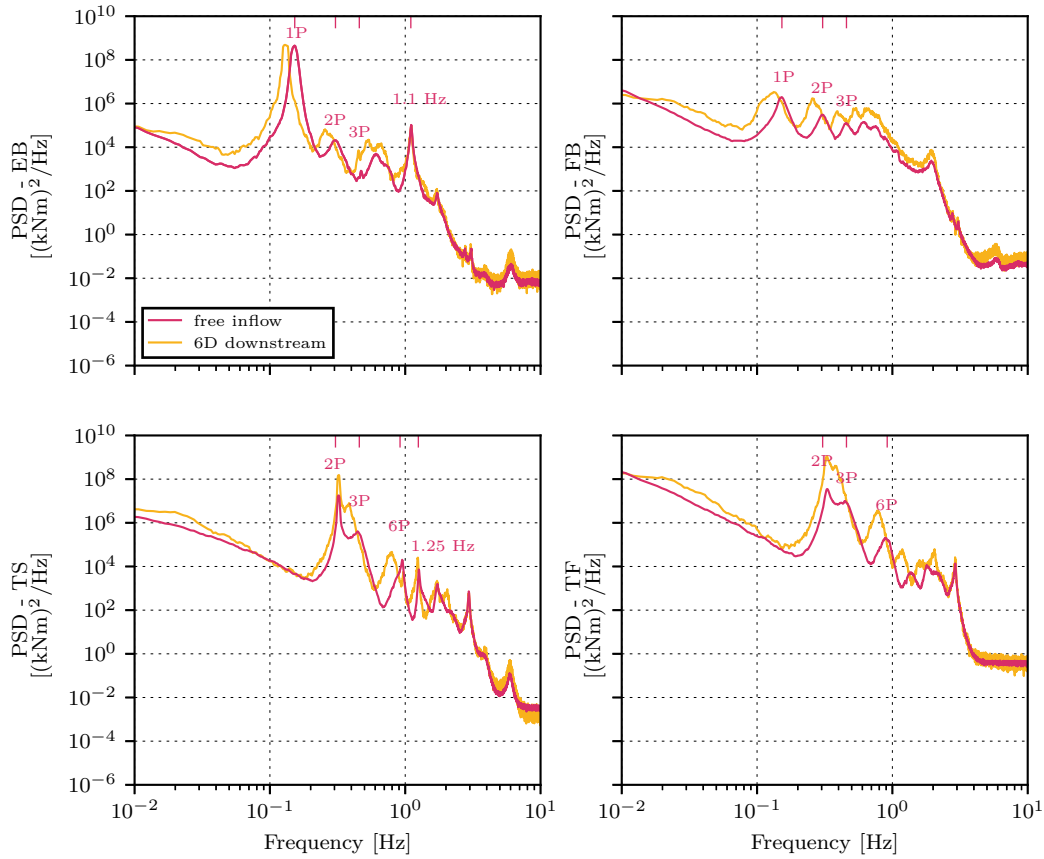


Figure 3.7: Average power spectral density of the EB, FB, TS and TF load series of a turbine operating in the undisturbed inflow of *N08* and a turbine located 6D downstream in the full wake of the upstream turbine.

$$\tilde{\Lambda}_c^{\text{FAST}}(\gamma) = \frac{\tilde{L}_c^{\text{FAST}}(\gamma)}{\tilde{L}_c^{\text{FAST}}(0^\circ)} \quad (3.18)$$

In Figure 3.7 the average power spectral densities (PSD) of the four investigated load sensors are plotted for a turbine in free inflow and in full wake conditions. The wind fields for the simulation of the upstream turbine were extracted upwind in the $y-z$ reference plane R_{xR} at the seven lateral positions of Y_F . Considering all six seeds of the wind field *N08*, this leads to a total of 42 individual spectrums that were considered for each average load spectra. The spectra of the turbine that was located 6D downstream in the full wake of an upstream turbine are the average of the six spectra that were obtained from the six simulations with the wind fields *N08-1* to *N08-6*. For the sake of clarity, characteristic frequencies were highlighted with most of them being harmonic of the rotational frequency 1P of the turbine rotor. The edgewise and the flapwise blade spectra are dominated by the 1P frequency at approximately 0.152 Hz

and the corresponding harmonics due to the asymmetrical blade loading. In addition, the natural frequency of the first edgewise mode at 1.1 Hz stands out. In general, all load spectra of the downstream turbine show a shift towards lower frequencies due to lower mean wind speeds in the wake and therefore a reduced rotational speed. The results are in good agreement with those from Lee et al. (2012) who performed large-eddy simulations of a *NREL 5-MW* in similar conditions. In their investigation, the turbine was modelled with the actuator line method and the large-eddy simulation was additionally coupled with the aeroelastic code *FAST*. If one examines the tower base fore-aft and side-to-side spectra, it becomes clear that in our results, in addition to the expected dynamic response at 3P and 6P frequencies, the 2P frequency makes a substantial contribution as well. In contrast, the results of Lee et al. (2012) do not indicate any significant contribution of the 2P frequency at all. We do not have a complete explanation for this difference, however, we observed that the 2P frequency and the first tower fore-aft/side-to-side natural frequencies of approximately 0.32 Hz match for the given conditions (Jonkman et al. (2009)). This is a special case, which was not intended as such prior to the investigation. As a result, very high DELs are observed for the tower base fore-aft and side-to-side moments regardless of the yaw misalignment of the turbine.

3.2.7 Test case scenario

In order to estimate the consequences of the application of a yaw based wake deflection on the structural loads of the turbines in a wind farm we defined four exemplary test case scenarios (Table 3.7). The test case scenarios are based on two reference wind farms with four *NREL 5-MW* turbines and a set of inflow conditions. The layouts of the two wind farms are shown in Figure 3.8. *WF2* is an upscaled version of *WF1* with the absolute distances between the turbines being increased by 50 %. This was done to be able to compare two wind farm arrangements of different densities since the effects of wake deflection on waked turbines vary for different downstream distances (see Sections 3.3.2, 3.3.3). In the further course, information about inflow directions refers to the definition given in the upper right-hand corner of Figure 3.8.

Whereas for the first two cases *A1* and *A2* only the two turbines *WT1* and *WT4* were considered and the inflow sector was limited to 45° to 135°, the complete wind farms *WF1* and *WF2* were considered in the two cases *B1* and *B2* with the full 360° inflow. For these four setups the power and loadings of all involved wind turbines were evaluated and the results with and without the use of wake deflection were compared. The inflow conditions for the analysis are based on the reference case *N08* wind fields with and

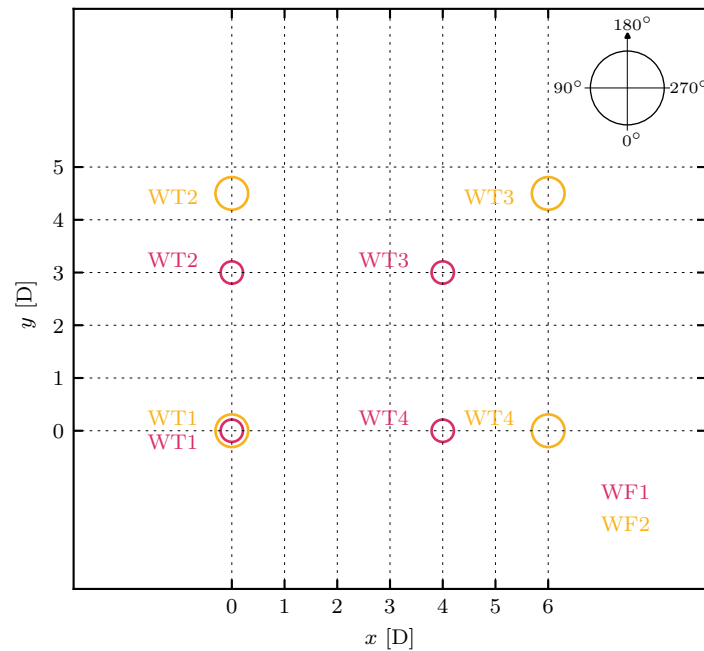


Figure 3.8: Layouts of the two reference wind farms WF1 and WF2.

Table 3.7: Overview of the setups of the four test case scenarios. Each scenario was investigated with and without wake deflection being used.

	turbines	layout of turbines	inflow directions
<i>A1</i>	2	WT1 and WT4 of WF1	$45^\circ - 135^\circ$
<i>A2</i>	2	WT1 and WT4 of WF2	
<i>B1</i>	4	full WF1	$0^\circ - 360^\circ$
<i>B2</i>	4	full WF2	

without yaw misalignment.

The aerodynamic interaction of the wind turbines within each wind farm depends on the inflow direction. In order to take this into account, all inflow directions from 0° to 359° in 1° steps were investigated. In each configuration it was determined which turbines operate fully in undisturbed inflow and which turbines are within the wake mapping region of an upstream turbine (Figure 3.9). If a turbine is situated in multiple wake maps simultaneously, the one with the strongest impact on the power output is chosen. Power and loading information of the waked turbines were obtained for the respective downstream positions by linear interpolation from the generated power and load maps. The results for the full 360° analysis are the cumulated wind farm power of all 360 inflow directions and the corresponding aggregated loading of each individual

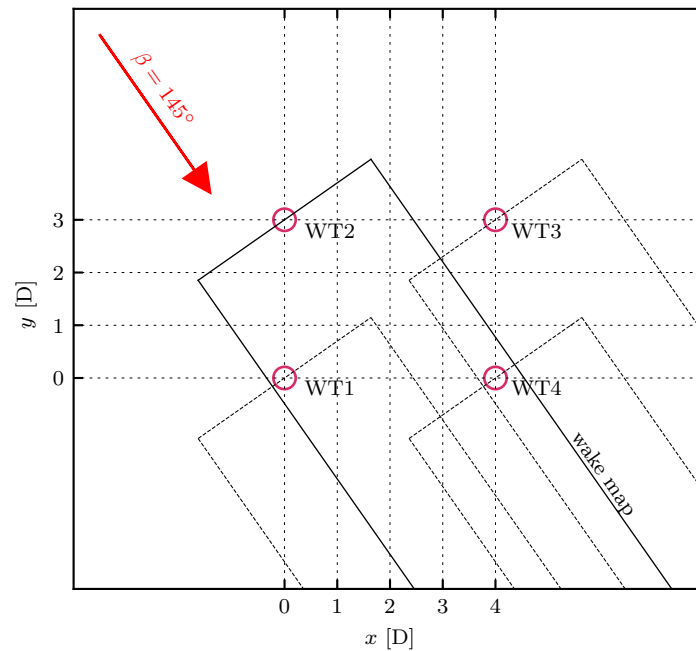


Figure 3.9: Exemplary inflow case of the reference wind farm *WF1* for an inflow direction of 145° . The limit of the wake mapping regions of all four turbines *WT1*, *WT2*, *WT3* and *WT4* are marked by black lines. In the given case, *WT4* is within the wake map limits of *WT2* and *WT3*.

wind turbine. In case of wake deflection, the yaw misalignments γ of the upstream turbines (0° , $\pm 10^\circ$ and $\pm 20^\circ$) that result in the highest power yield of the wind farm for the given inflow direction were chosen. For turbines in free inflow, the reference power and loading information listed in Table 3.5 and Table 3.6 were chosen.

3.3 Results and Discussion

This section is divided into four parts. In the first part, the characteristics of the large-eddy wind fields are analysed in detail. The goal is to develop a better understanding of the extent to which the conditions in the individual 10 min wind fields, and in comparison to each other, vary spatially. This is important to assess the uncertainties associated with the prediction of the power maps and loads maps (i.e. wake maps) in the two subsequent sections. In the last section, the wake maps are used to exemplarily estimate the consequences of the application of a yaw based wake deflection on the power and loading of the individual wind turbines in the reference wind farms.

3.3.1 Wind field characteristics

When comparing wind fields, information such as average wind speeds and turbulence intensities are usually used. Even if these figures match, seemingly equivalent wind fields can still lead to different structural loadings of wind turbines due to varying characteristics of the individual wind speed time series at specific points in space. When working with stochastic wind fields, statistical models are used to generate wind fields with certain characteristics. Although identical on average, different temporal and spatial distributions of wind speeds within a wind field can be generated using random numbers, i.e. seeding. By using several such wind fields, more representative average turbine loads are obtained for the investigated mean conditions.

When using LES, different wind fields with similar characteristics can be created by introducing distortions at different locations at the beginning of the simulation that affect the development of the flow. Unfortunately, creating new wind fields is a rather computationally demanding and time consuming process. Due to the inflow dynamics of the large-eddy simulations, a longer simulation time or the choice of different positions of the wind turbine within the wind field could serve as a basis for a simpler approach. In the case of longer simulation times, however, it must be remembered, that the overall characteristics of the large-eddy wind field are changing more and more over time. The extent to which the conditions differ in the wind fields used in this study was examined exemplarily based on the average power output P_{cs}^{REWS} and P_{cs}^{FAST} of a virtual turbine in undisturbed inflow that was positioned at the seven lateral positions Y_F in the reference plane R_{XR} . The investigation was performed for all six seeds of the four reference wind fields $N06$ to $N12$ and additionally allows a comparison of both methods established for obtaining the power output. The results are presented in Figure 3.10.

For the reference cases $N06$ to $N12$, the standard deviations of P_{cs}^{FAST} within a seed is approximately 2% to 5% of the average power from the respective seven examined positions with free flow. Individual power outputs differ by up to 8% from the mean value of the corresponding seed. Furthermore, P_{cs}^{REWS} values for the three below-rated wind fields are 6% larger on average than the P_{cs}^{FAST} results. For the case $N12$, P_{cs}^{REWS} is consistently at rated power. However, P_{cs}^{FAST} indicates that the turbine is in some cases still operating slightly below rated.

To illustrate how the power output from the large-eddy wind fields and the derived stochastic wind fields differ, the average P_{cs}^{STO} of the six stochastic seeds of each large-eddy wind speed case and their standard deviation are also included in Figure 3.10. The small standard deviations of each mean value shows, that the seeding does not

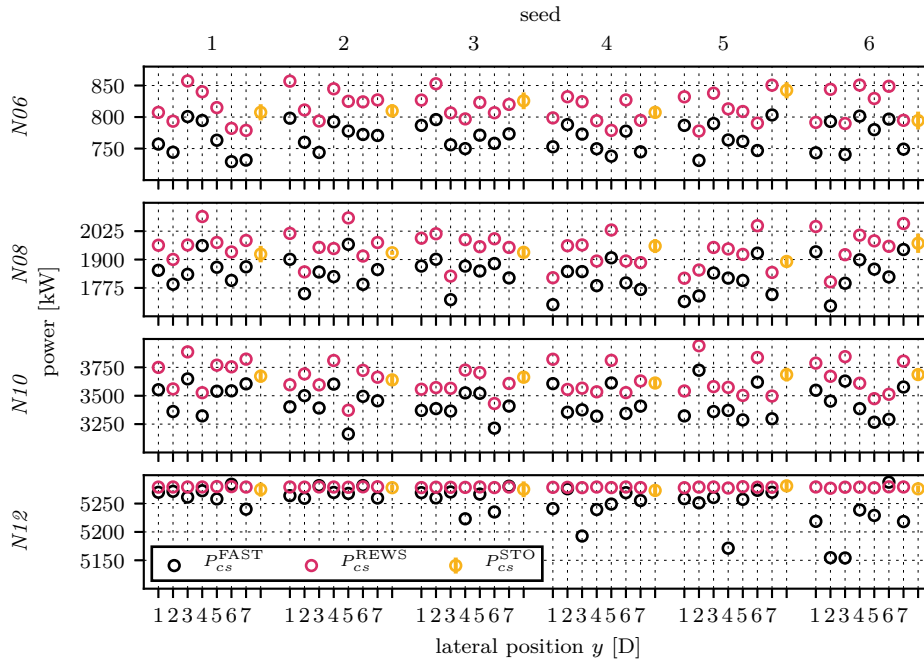


Figure 3.10: Average power values $P_{cs}^{\text{REWS}}(x_R, Y_F)$ and $P_{cs}^{\text{FAST}}(x_R, Y_F, \gamma)$ at the seven lateral positions Y_F in the reference plane R_{x_R} with undisturbed inflow for all six seeds of the reference wind fields $N06$ to $N12$. P_{cs}^{STO} indicates the average power of the six stochastic seeds of each large-eddy seed and the corresponding standard deviation.

significantly affect the resulting power. However, in most cases, the P_{cs}^{STO} results are slightly higher than the P_{cs}^{FAST} values or in the upper range.

3.3.2 Wake mapping - power

3.3.2.1 Wind turbine in normal operation

For estimating the power output of a downstream turbine, which is affected by the wake of an upstream turbine, we tested two different methods. Due to it being well known and widely used, *FAST* was chosen as reference for the comparisons carried out in the following. In Figure 3.11, the normalised average power $\rho_c^{\text{FAST}}(x, y, 0^\circ)$ of the virtual downstream turbine is shown for the reference wind fields $N06$ to $N12$. These values were determined according to Equation (3.19) which involves an averaging of the power maps of the individual seeds and a subsequent normalisation of the results with the average power obtained at free flow. It should be emphasized that in all cases the wakes are still clearly pronounced even 10D downstream of the wake-generating turbine. Due to an almost constant thrust coefficient of the *NREL 5-MW* within the below rated region, the three power maps of the cases $N06$, $N08$ and $N10$ are very comparable. The white region in the centre of the wake map of the $N06$ reference case

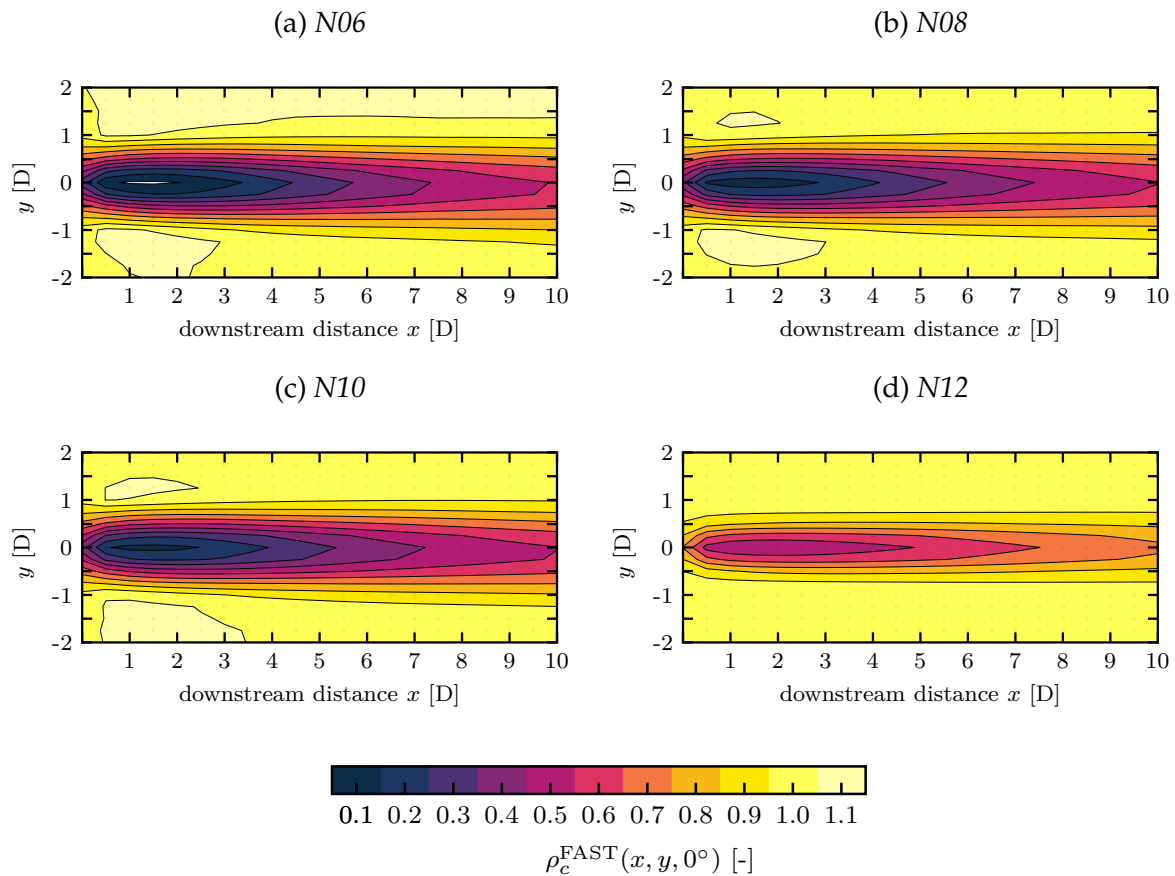


Figure 3.11: Normalised power maps $\rho_c^{\text{FAST}}(x, y, 0^\circ)$ for the four reference wind fields *N06* to *N12*.

at a downstream distance of 1D to 2D indicates that the turbine did not generate any power in the *FAST* simulation due to too low wind speeds.

In Figure 3.12 the corresponding standard deviation of the power maps of the six seeds for each case are shown (Equation (3.20)). It indicates that despite their similar characteristics, larger inhomogeneity in wind speed exist within the six large-eddy simulations of 10 min duration each. This can result in considerable differences in the power yield of a wind turbine that is located at one specific position throughout the six cases and of a turbine that is located at different positions within one single wind field case. These uncertainties need to be considered when drawing conclusions from the results of only a few simulations.

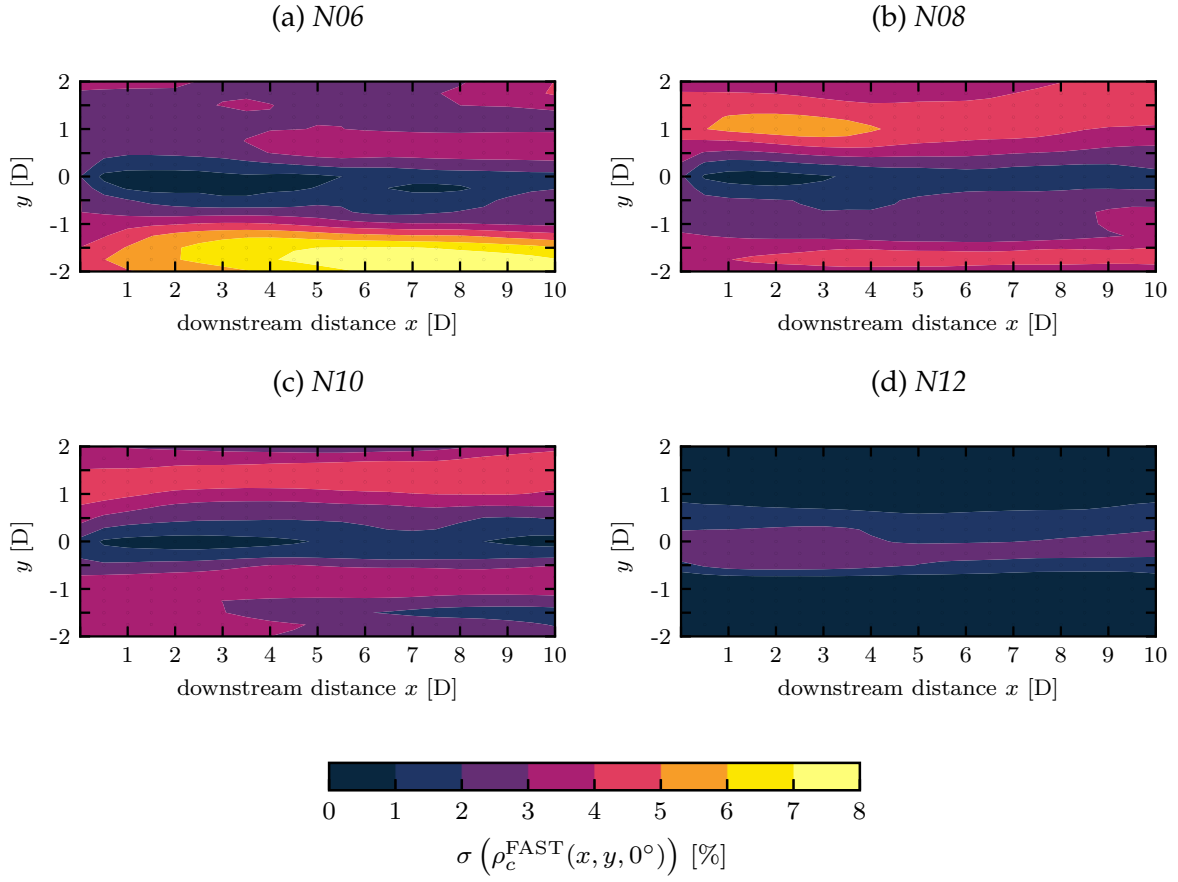


Figure 3.12: Standard deviation of the average power values $\rho_c^{\text{FAST}}(x, y, 0^\circ)$ of the power maps of the six seeds of each reference case.

$$\rho_c^{\text{FAST}}(x, y, \gamma) = \frac{\frac{1}{6} \sum_{i=1}^6 P_{ci}^{\text{FAST}}(x, y, \gamma)}{\bar{P}_c^{\text{FAST}}(0^\circ)} \quad (3.19)$$

$$\sigma(\rho_c^{\text{FAST}}(x, y, \gamma)) = \frac{1}{\bar{P}_c^{\text{FAST}}(0^\circ)} \left(\frac{1}{5} \sum_{i=1}^6 \left(P_{ci}^{\text{FAST}}(x, y, \gamma) - \frac{1}{6} \sum_{j=1}^6 P_{cj}^{\text{FAST}}(x, y, \gamma) \right)^2 \right)^{\frac{1}{2}} \quad (3.20)$$

In Figure 3.13, the ratio $\eta_c(x, y, 0^\circ)$ of the normalised REWS-based power (Equation (3.22)) and the normalised *FAST*-based power (Equation (3.19)) is shown. The values are determined according to Equation (3.21). White areas in the graphs indicate that the turbine did not generate any power in the *FAST* simulation due to too low wind speeds. Regarding the comparison of REWS-based and *FAST*-based power outputs, it is evident that the estimated absolute REWS power value, as determined

by us (Equation (3.22)), is always higher than the one from *FAST*. The strongest differences of the quotient of the normalised power maps exists in the wake region at small downstream distances. With increasing wind speeds the region of larger differences extends further and further downstream. In the near wake of the 6 ms^{-1} case, differences of up to 44 % occur due to a very small overall power output near cut-in conditions. This is not fully represented in the colour bar, which has been limited to 1.2 so that the dominant regions of minor and moderate increases are highlighted. For the 8 ms^{-1} and 10 ms^{-1} cases and downstream distances of more than 5D, the differences are below 10 %. Unfortunately, the 2D to 5D downstream region, in which the larger differences occur, is getting more and more attention as wind farm developers try to reduce the distances between turbines to make optimal use of the limited number of sites that promise high energy yields.

$$\eta_c(x, y, \gamma) = \frac{\rho_c^{\text{REWS}}(x, y, \gamma)}{\rho_c^{\text{FAST}}(x, y, \gamma)} \quad (3.21)$$

$$\rho_c^{\text{REWS}}(x, y, \gamma) = \frac{\frac{1}{6} \sum_{i=1}^6 P_{ci}^{\text{REWS}}(x, y, \gamma)}{\bar{P}_c^{\text{REWS}}(0^\circ)} \quad (3.22)$$

Whilst the REWS-based method is an idealised approach that is simple and easy to implement, the achievable accuracy, at least in the form implemented by us, may not meet the requirements of investigations in every case. Especially in inhomogeneous wake regions, differences are significant. In most cases, it can be used as an upper estimate though. To what extent more accurate predictions can be achieved with the approach and a power curve that is more specifically fitted to the investigated conditions was not part of this investigation.

3.3.2.2 Wind turbine operating under yaw misalignment

In Figure 3.14 the average normalised power outputs $\rho_c^{\text{FAST}}(x, y, \gamma)$ are shown for the *N08* case and yaw misalignments γ of $\pm 10^\circ$ and $\pm 20^\circ$. For positive yaw misalignments, a displacement of the strongest wake effect at each downstream position towards the left-hand side can be seen. A yaw misalignment in the opposite direction leads to a wake deflection towards the right hand side. The overall wake depth along the centre axis $y = 0\text{D}$ in the downstream direction is illustrated in Figure 3.15 for the reference cases *N06* to *N12* and the four cases of *N08* with yaw misalignments.

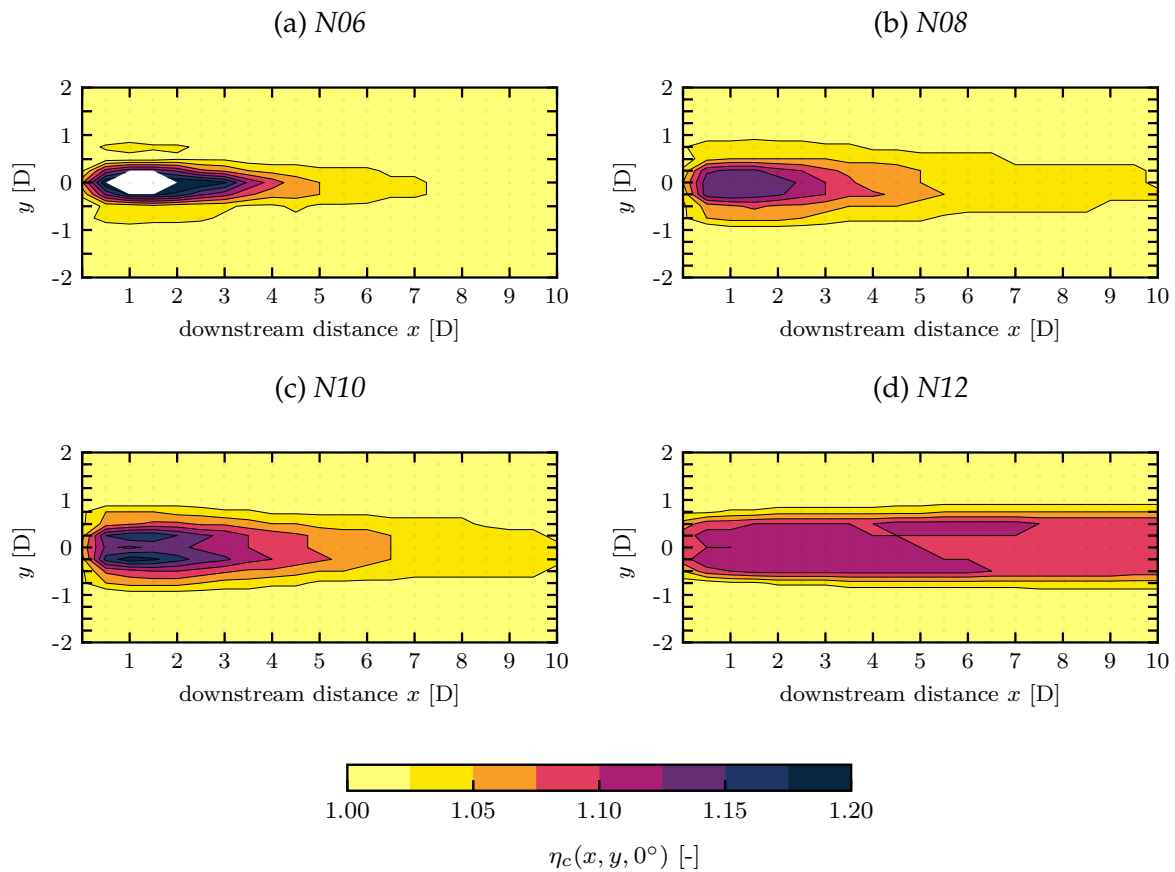


Figure 3.13: Wake mappings of $\eta_c(x, y, 0^\circ)$ which represents the ratio of the normalised REWS-based power maps and the normalised *FAST*-based power maps for the four reference wind fields *N06* to *N12*

In general very comparable results are obtained for the cases *N06* to *N10* with the exception of the deficit of *N06* being higher within the first 4D. Due to the small ambient turbulence intensity of around 6%, a very slow wake recovery is observed. Even at 10D downstream, power values of approximately only 55% to 75% in comparison to the ones in free inflow are obtained.

For the cases with yaw misalignment, a higher power output at the downstream turbine is obtained. The gain is larger for the two cases with 20° yaw misalignment in comparison to the cases with 10° misalignment. Furthermore, the deflection towards the right hand side results in higher gains at the downstream turbines. An analysis regarding the benefit of the wake deflection when looking at a two-turbine configuration is part of Section 3.3.4.

A graphic representation of the results of the comparison between the REWS-based power maps and the *FAST*-based power maps for the cases with yaw misalignment

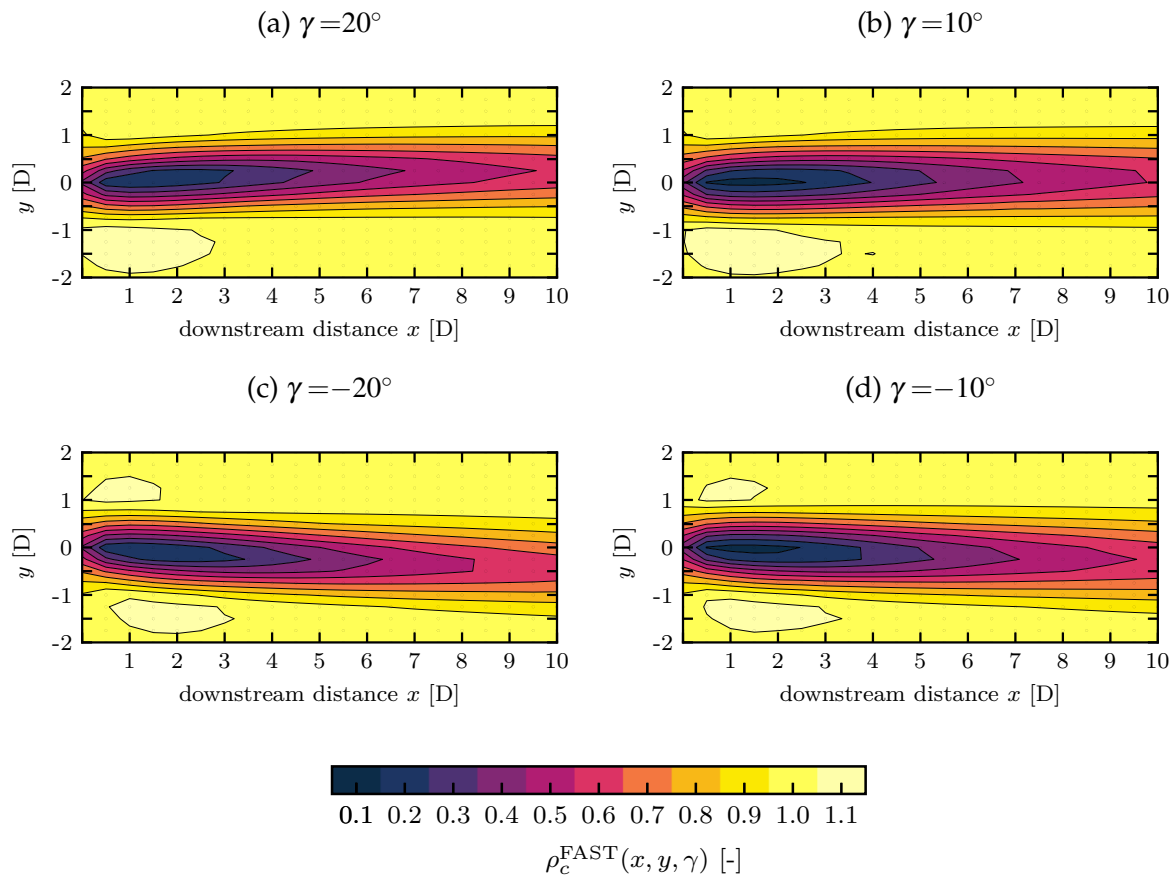


Figure 3.14: Normalised power maps $\rho_c^{\text{FAST}}(x, y, \gamma)$ for the reference wind field *N08* and turbine yaw misalignments γ of (a) 20° , (b) 10° , (c) -20° and (d) -10° .

is omitted. The reason for this is that the findings did not differ from those for *N08* which are depicted in Figure 3.13 with the exception of the characteristic shape of the deflected wakes (Figure 3.11).

3.3.3 Wake mapping - loading

In this section, the loads of a wind turbine in undisturbed inflow with and without yaw misalignment and the corresponding loads of a downstream turbine are examined. The content of this section is directly related to the analysis of the power output of the wind turbine in the previous section. The main goals are to obtain the load maps for the different blade and tower sensors and to understand how turbine loads are affected if low-pass filtered wind fields with a reduced range of turbulence are being used.

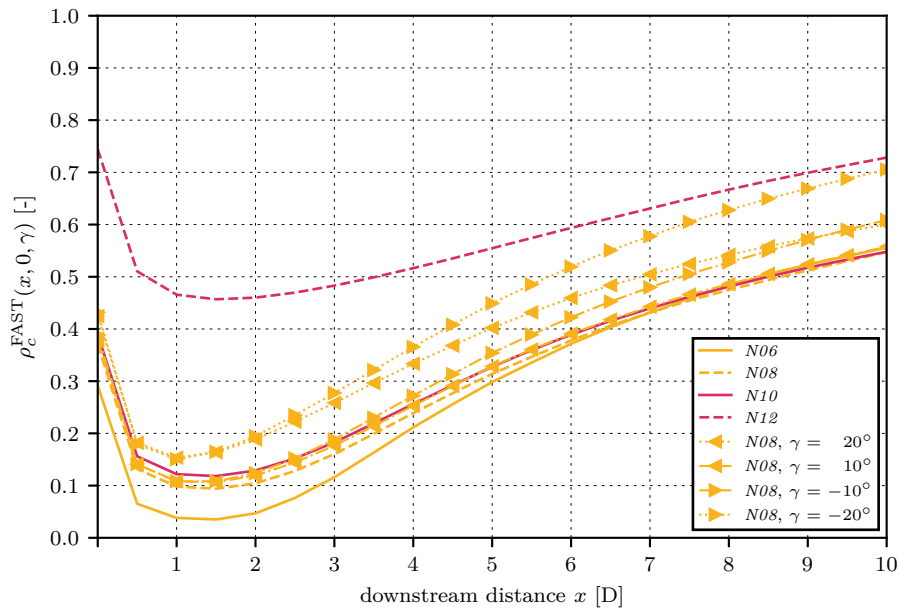


Figure 3.15: Power output $\rho_c^{\text{FAST}}(x, 0, \gamma)$ for the reference cases *N06* to *N12* and the yaw misalignment cases of *N08*.

3.3.3.1 Wind turbine in normal operation

In Figure 3.16a-d, the average DELs and the standard deviation of the four investigated load sensors FB, EB, TS and TF for a turbine in undisturbed inflow conditions of the five large-eddy reference wind fields are shown. All four figures are identically structured. The investigated wind fields are listed along the x -axis. The column labelled 32 Hz includes the results of the stochastic baseline wind fields that were generated for each large-eddy reference case seed. Towards the left-hand side, the results of the more and more filtered stochastic wind fields are shown. On the right-hand side of the vertical black dashed line, the results obtained from the undisturbed inflow of the large-eddy wind fields are presented. Each individual mean DEL value and the corresponding standard deviation of the stochastic wind fields are determined by considering the 36 results of the six *TurbSim* seeds of each of the six large-eddy seeds for the corresponding reference wind speed case. In the case of the large-eddy simulation results, all 42 cases consisting of the seven extracted undisturbed inflow wind fields at the lateral positions Y_F in the reference plane R_{xR} of each of the six large-eddy seeds, are considered.

The edgewise blade root bending moment (Figure 3.16a) does not differ significantly between the five reference cases as it is mainly driven by mass of the blades and the number of rotor revolutions. The filtering of the inflow therefore has little effect on the observed loads and all results differ by less than 1% from the unfiltered inflow. Furthermore, the deviations between individual seeds are very small as the standard devi-

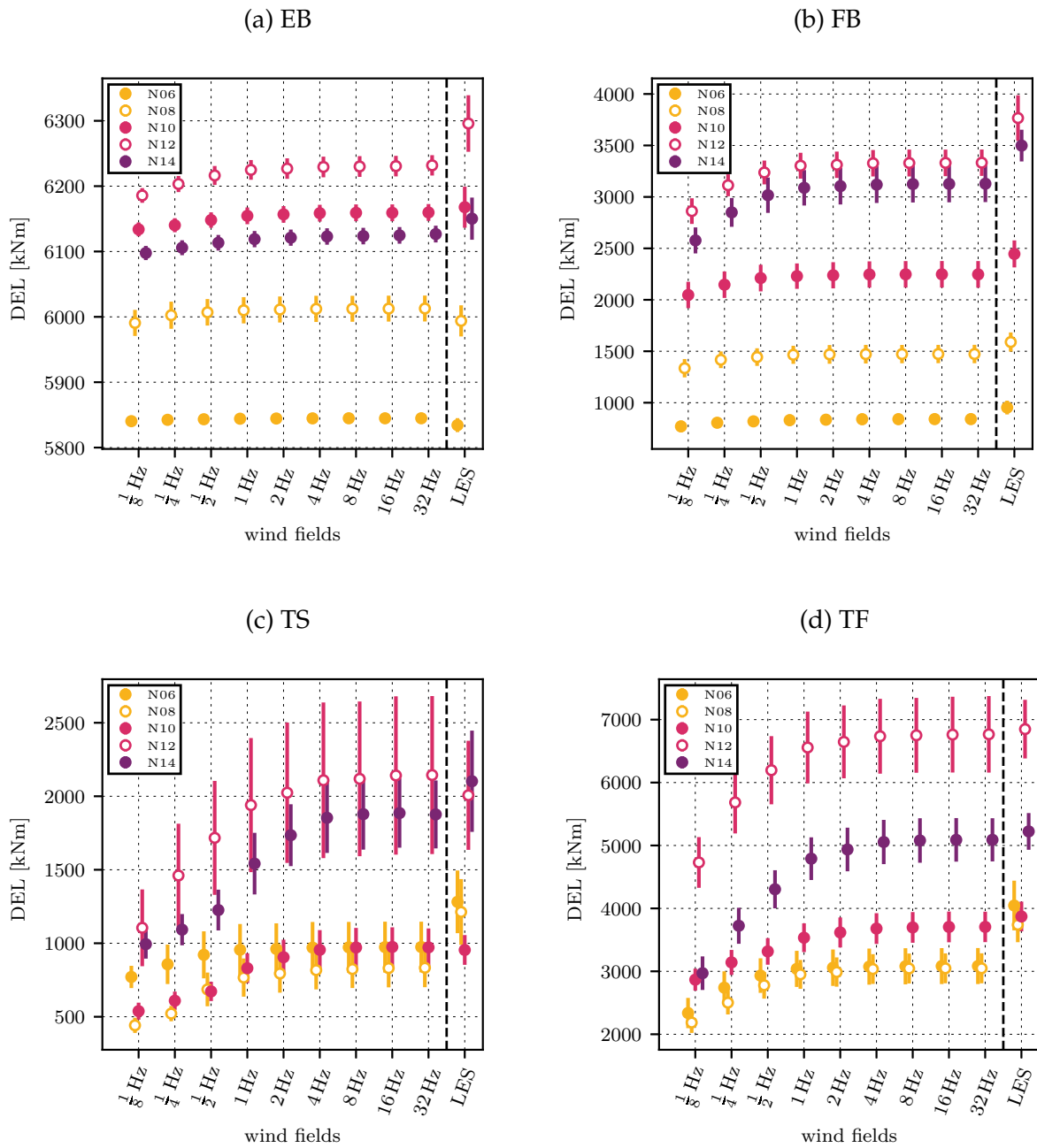


Figure 3.16: Average DELs of the (a) edgewise and (b) flapwise blade root bending moments and the tower base (c) side-to-side and (d) fore-aft moments generated by the undisturbed large-eddy inflow, the stochastic baseline cases (32 Hz) and the filtered stochastic wind fields. The error bars indicate one standard deviation of uncertainty. The results of the five reference cases are plotted slightly shifted with respect to the x-axis for each wind field case to avoid any overlapping of the graphs.

ation indicates. The DELs obtained from the large-eddy simulation agree well with the results from *FAST*. However, larger standard deviations suggest that the seven undisturbed inflow seeds of each 10 min large-eddy seed differ and that the inflow conditions are not fully homogeneous across the inflow throughout the full simulation time. The reduction of the blade root moments of the *N14* case in comparison to the *N12* case is due to the pitching activity above rated. Due to the constant rotational speed in the above rated region, the in-plane blade root moment hardly changes.

In contrast to the edgewise loads, the flapwise loads (Figure 3.16b) are more dependent on the inflow conditions which is indicated by an increased standard deviation. Filtering fluctuations above 2 Hz results in a reduction of the obtained loads below 99 % of the baseline case results for all reference cases. Overall, the flapwise loads from the LES are higher in all cases than those from the derived stochastic wind fields. The load reduction observed for the case *N14* in comparison to the *N12* case is caused by a reduction in thrust force in the above rated control region for increasing wind speeds.

In contrast to the blade root loads, a strong dependency on the frequency content is observed for the tower base loads. For the filtered stochastic inflow wind fields 98 % of the stochastic baseline case loads are obtained with the 4 Hz wind fields. In case of a further reduction of the frequency range, a steep decrease in loads is observed as relevant frequency contributions are filtered. This must be taken into account when referring to loads from LES as the frequency resolution that can be obtained is related to the grid spacing. Unfortunately, an infinite reduction of the grid spacing is not possible due to a significant increase of the required computational resources. Still, an adequate frequency resolution of the LES wind fields is of particular importance for assessing the tower loads. The effect of the rotational sampling of the blades is transferred but no sampling takes place through the tower itself. This can lead to an underestimation of tower loads with LES simulations.

A further observation regarding the tower loads are the higher standard deviations in comparison to the blade loads. This indicates a larger sensitivity to the inflow conditions. Especially the case *N12* stands out due to a very high standard deviation. As this test case is the closest one to the transition point of below rated and rated turbine operation with a significant peak in the thrust curve, a correlation between high tower load fluctuations and turbine control is assumed.

In Figure 3.17 the normalised load maps $\Lambda_c^{\text{FAST}}(x, y, 0^\circ)$ (Equation 3.23 for the reference wind field *N08* are shown). The normalised load maps for the other four reference wind fields can be found in the Appendix 3.B. For each sensor, the colour scale is identical throughout the different wind fields to ensure a good comparability of the results.

$$\Lambda_c^{\text{FAST}}(x, y, \gamma) = \frac{\left(\frac{1}{6} \sum_{i=1}^6 (L_{ci}^{\text{FAST}}(x, y, \gamma))^m \right)^{\frac{1}{m}}}{\bar{L}_c^{\text{FAST}}(0^\circ)} \quad (3.23)$$

As in the case of the power deficit, the wake of the upstream turbine can be identified up to the investigated 10D downstream distance based on the DELs for the given inflow conditions. Looking at the results, it is once again confirmed that the DELs of the edgewise blade root bending moments are least dependent on the inflow conditions. However, an increase of these loads is still to be expected for downstream turbines with a negative lateral displacement. For positive lateral displacements, even a reduction of loads is observed. Nevertheless, the load variations of the edgewise bending moment are significantly lower for any wake position than for any other investigated load sensor. The flapwise blade DELs show an almost symmetrical characteristic in the wake with minimally higher DELs for negative lateral offsets. The load maps also show that partial wake conditions in the near wake lead to DELs much higher than for full wake conditions.

In comparison to the blade DELs, a significantly higher increase of the tower DELs in the wake is observed with peaks at 500%. We assume that the results are caused because of the 2P frequency of the rotor matching the first natural frequency of the tower (Figure 3.6).

In case of the side-to-side DELs, four streaks can be identified in the near wake region that indicate high loads for conditions in which the partial wake exposure has the highest imbalance between the left and right side of the rotor. This changes further downstream as higher side-to-side DELs are experienced by turbines with smaller lateral displacement and full wake exposure. The tower fore-aft DELs are similar to the side-to-side DELs for downstream distances of more than 3D. Also in this case, the highest DELs are experienced for small lateral displacements. Below 3D, the load map has the same characteristics as the one of the flapwise DELs map with the highest DELs being experienced in the partial wake region and lower ones in the full wake region.

Overall, it should be noted that the load maps indicate no preferred wake regions with a more optimal load distribution. If the load increases in certain regions are lower for specific sensors, then other sensors are particularly affected. The flapwise loads are, for example, highest in partial wake conditions at small downstream distances whereas the tower fore-aft loads are high in full wake conditions for medium downstream distances. Further investigations are therefore needed in order to better understand the consequences for an optimised wind farm operation.

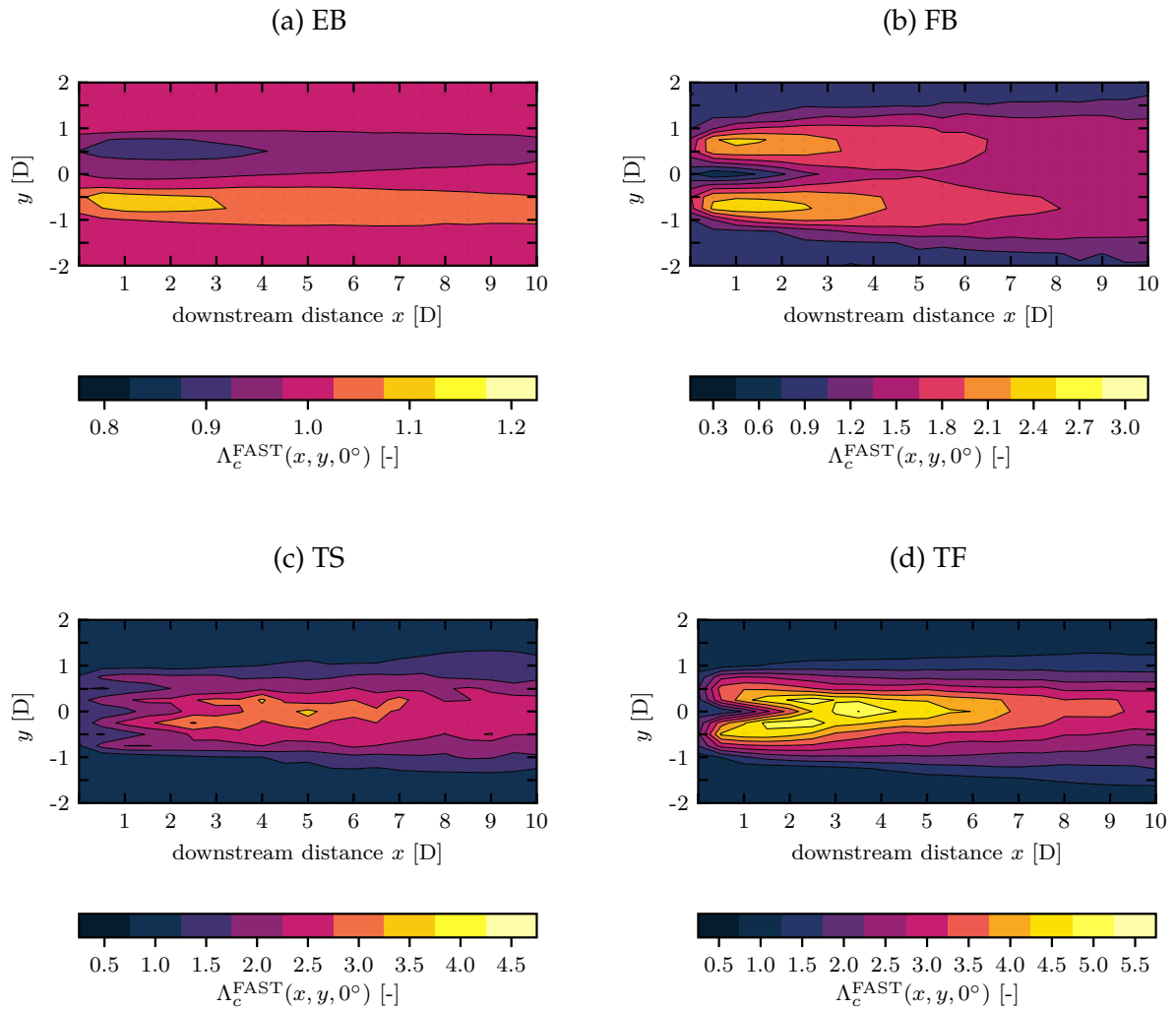


Figure 3.17: Normalised load maps $\Lambda_c^{\text{FAST}}(x, y, 0^\circ)$ for the reference wind field *N08* and the load sensors (a) edgewise blade root bending moment, (b) flapwise blade root bending moment, (c) tower base side-to-side moment and (d) tower base fore-aft moment.

3.3.3.2 Wind turbine operating under yaw misalignment

In Figure 3.18 and Figure 3.19 the normalised load maps $\Lambda_c^{\text{FAST}}(x, y, \gamma)$ for the blade and tower loads, respectively, are shown for the reference wind field *N08* and $\gamma = \pm 20^\circ$. The normalised load maps for $\gamma = \pm 10^\circ$ can be found in the Appendix 3.C. To ensure a good comparability of the results, the colour scale for each sensor matches the ones from the previous analysis without yaw misalignment (Section 3.3.3.1).

First it becomes clear that yaw misalignment does affect the load maps similar to the investigated power maps as the skew of the wake pattern indicates. Furthermore, the emerging characteristics for the cases with and without wake deflection are virtually identical throughout the investigated yaw misalignments γ . These are important findings, as the mean wind speed plays a large role when considering the power yield. Fluctuations in the inflow are partly filtered by the rotor. In the case of turbine loads, the fluctuations are more relevant. The fact that the behaviour is nevertheless similar in both cases and that the yaw misalignment does not result in the development of new structures simplifies further investigation and model development.

Due to the great similarities of the load maps with yaw misalignment to the ones without yaw misalignment, we again do not have preferred wake regions with more optimal load distribution. When optimising the overall wind farm power yield this could lead to an increase of certain loads at turbines that are exposed to wake conditions, whereas at the same time other loads might be reduced in comparison to the non-optimised wind farm operation. Concerning an optimisation of a wind farm with the focus on the loading of the turbines, these differences require that one would have to focus on certain components instead of an overall reduction.

3.3.4 Test case scenario - Impact of wake deflection on power and loading

3.3.4.1 Test case: Two turbines

The basic approach for the analysis of the effects of yaw-based wake deflection on the loads of the turbines in the wind farm is described in Section 3.2.7. Reference case *N08* serves as the basis for the inflow conditions. Before the effects of wake deflection on the two reference wind farms *WF1* and *WF2* are examined in their entirety, a preliminary analysis of the two turbines *WT1* and *WT4* for the *WF1* and *WF2* configurations is carried out for inflow directions of 45° to 135° to investigate the interaction between two turbines in more detail (see Table 3.7, test cases *A1* and *A2*). In this sector, *WT4* is exposed to different partial and full wake situations due to the wake of *WT1*.

As in the case of the reference wind farms, the inflow directions are evaluated in 1°

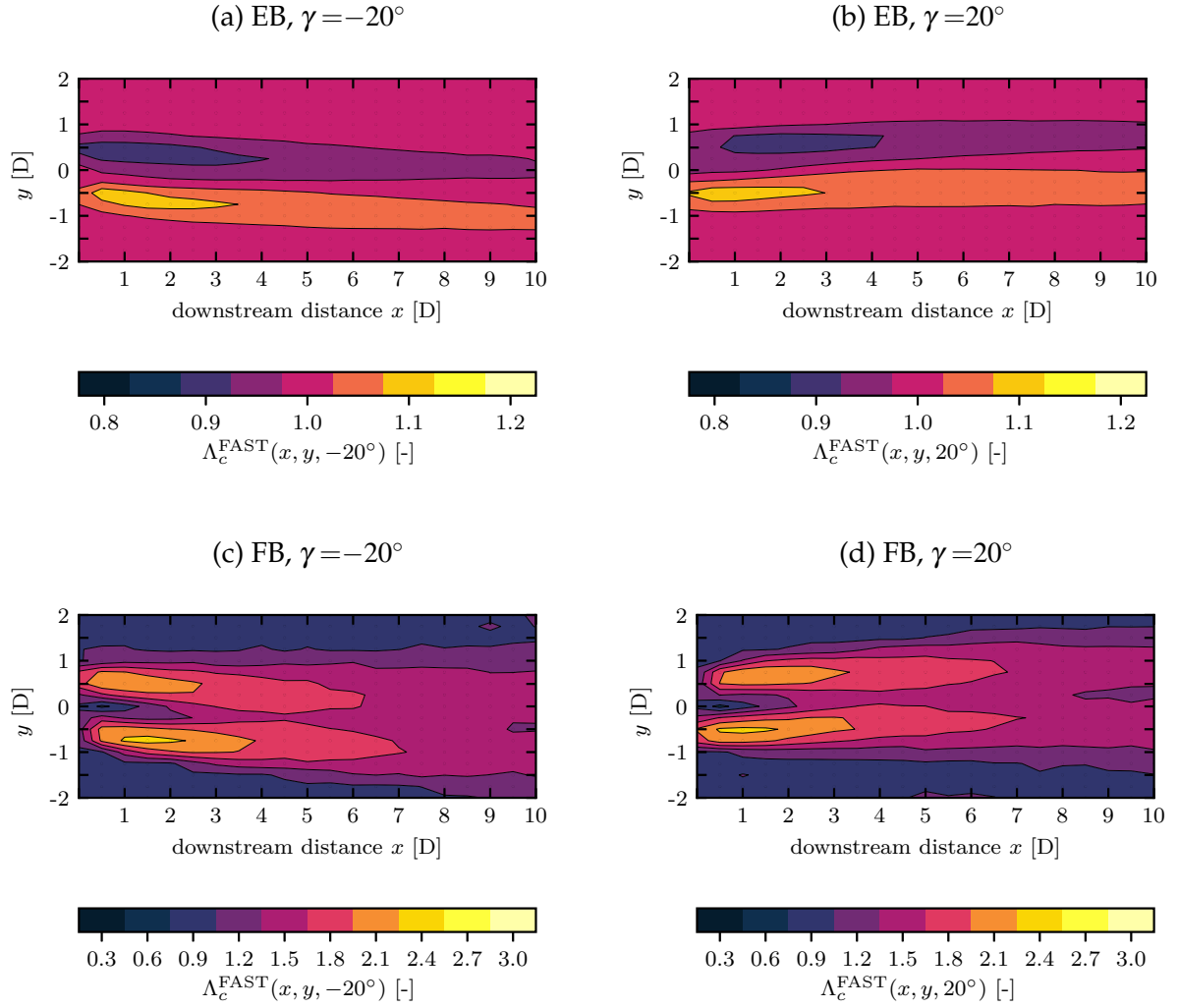


Figure 3.18: Normalised load maps $\Lambda_c^{\text{FAST}}(x, y, \gamma)$ for the reference wind field *N08* with yaw misalignments γ of the upstream turbine of -20° and 20° and the load sensors for the edgewise and flapwise blade root bending moments.

steps so that there are 91 individual situations to be analysed in the relevant 90° sector. The resulting power output and optimal yaw angles are presented in Figure 3.20. In the left column, the results for the *WF1* configuration are shown in which *WT1* and *WT4* are $4D$ apart whereas in the right column the results of the *WF2* configuration with a distance of $6D$ between the turbines are shown. The spacing between the wind turbines for both cases are referred to as D_{WT} (Equation (3.24)) for the sake of clarity in upcoming equations.

$$D_{\text{WT}} = \{4D, 6D\} \quad (3.24)$$

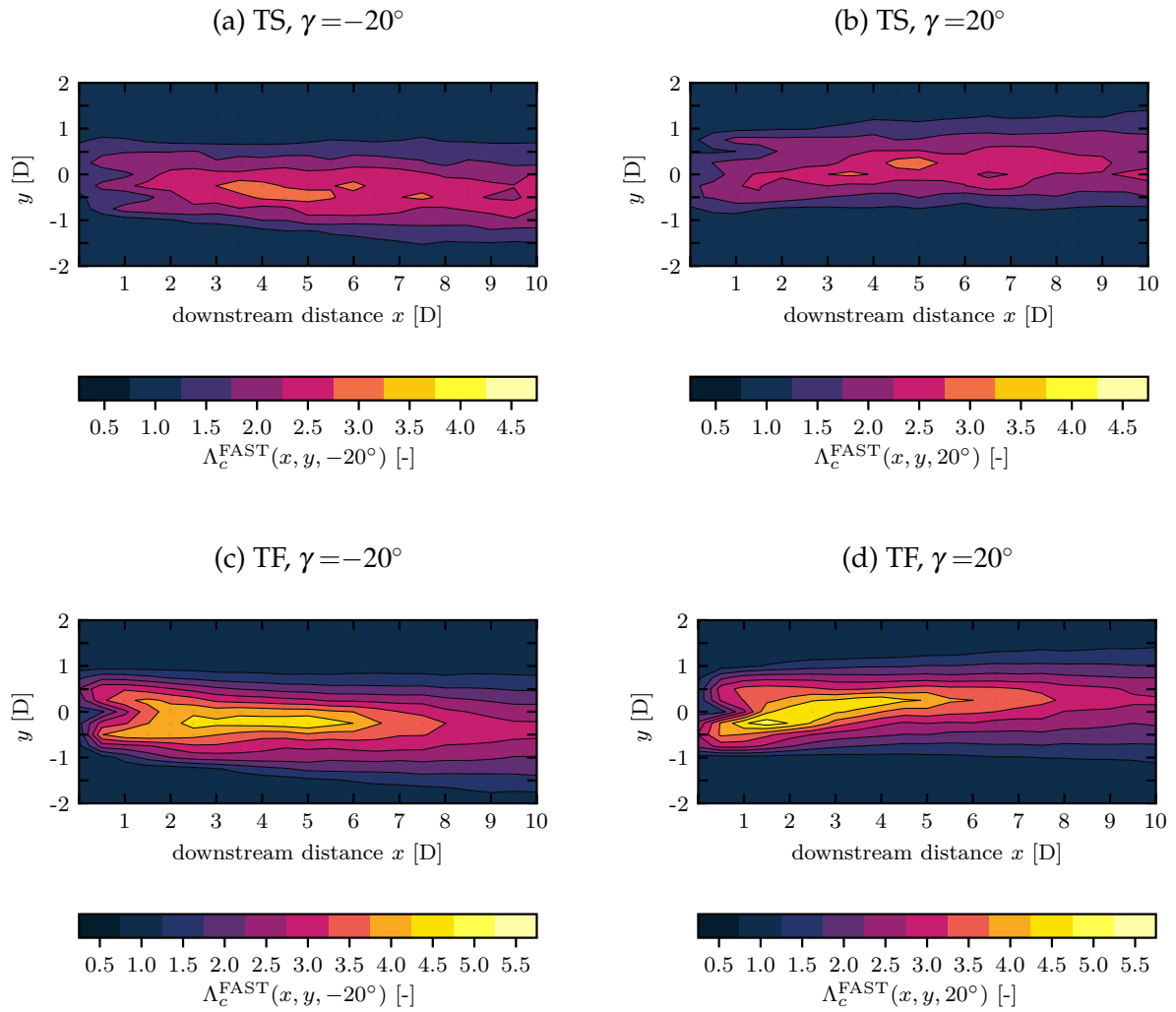


Figure 3.19: Normalised load maps $\Lambda_c^{\text{FAST}}(x, y, \gamma)$ for the reference wind field *N08* with yaw misalignments γ of the upstream turbine of -20° and 20° and the load sensors for the tower base side-to-side moment and tower base fore-aft moment.

3.3.4.2 Power

For all investigated inflow directions, the individual power outputs P_{WT1} of *WT1* and P_{WT4} of *WT4* are visualized in the first two rows of Figure 3.20 for the conventional greedy control and optimised with wake deflection. P_{WT1} and P_{WT4} are calculated according to Equations (3.25) and (3.26). The two variables $\tilde{\rho}_c^{\text{FAST}}(\gamma)$ and $\rho_c^{\text{FAST}}(x, y, \gamma)$ were previously introduced in Equations (3.16) and (3.19). If wake deflection is applied, γ is chosen such that the combined power of *WT1* and *WT4* is maximized (Equation (3.27)). The corresponding yaw angle γ of *WT1* is given in the third row of Figure 3.20. In the last row, P_G is presented which indicates the overall gain in power yield of *WT1* and *WT2* with the application of wake deflection in relation to

the conventional greedy control. P_G is determined according to Equation (3.28). The combined power of both *NREL 5-MW* turbines in free inflow conditions of 1834 kW each is used for normalisation (Table 3.5). This was done to ensure a high level of comparability of the data.

$$P_{WT1}(\gamma) = \tilde{\rho}_c^{\text{FAST}}(\gamma) \quad (3.25)$$

$$P_{WT4}(D_{WT}, \beta, \gamma) = \rho_c^{\text{FAST}}(\cos(\beta - 90^\circ) \cdot D_{WT}, -\sin(\beta - 90^\circ) \cdot D_{WT}, \gamma) \quad (3.26)$$

$$\operatorname{argmax}_{\gamma} (P_{WT1}(\gamma) + P_{WT4}(D_{WT}, \beta, \gamma)) \quad (3.27)$$

$$P_G = 100 \cdot \frac{P_{WT1}(\gamma) + P_{WT4}(D_{WT}, \beta, \gamma) - (P_{WT1}(0^\circ) + P_{WT4}(D_{WT}, \beta, 0^\circ))}{1834 \text{ kW} \cdot 2} \quad (3.28)$$

As one would expect, the results show that *WT4* is exposed to more severe wake conditions in *WF1* in comparison to *WF2* due to the smaller spacing between the two turbines. Furthermore, the output value P_G confirms that for the given conditions, the application of wake deflection does increase the overall power output of the two wind turbines. Maximum gains on the order of 4.7% are achieved for certain inflow directions in relation to the combined power of the two wind turbines in undisturbed inflow. The optimal yaw misalignment γ increases as the conditions approach full wake exposure of the downstream turbine *WT4*. However, if the downstream turbine is situated in a full wake condition, the application of wake deflection does not lead to an increase of the overall power output.

When looking at the results of P_{WT4} for the wake deflection case (Figure 3.20), peaks in the graph can be seen. These are caused by the fact that only a limited number of yaw misalignment cases ($0^\circ, \pm 10^\circ, \pm 20^\circ$) have been examined. Therefore, situations are obtained in which the power gain at the downstream turbine is just not sufficient to compensate the loss at the upstream turbine caused by an additional yaw misalignment of 10° . When investigating a larger number of γ values, a more continuous curve is to be expected.

With regard to the application of the wake deflection, we determined, that with our setup it is being used by the upstream turbine for an inflow sector of $\pm 15^\circ$ if both turbines are 4D apart and in a $\pm 11^\circ$ wide sector in the case of 6D spacing. The effective

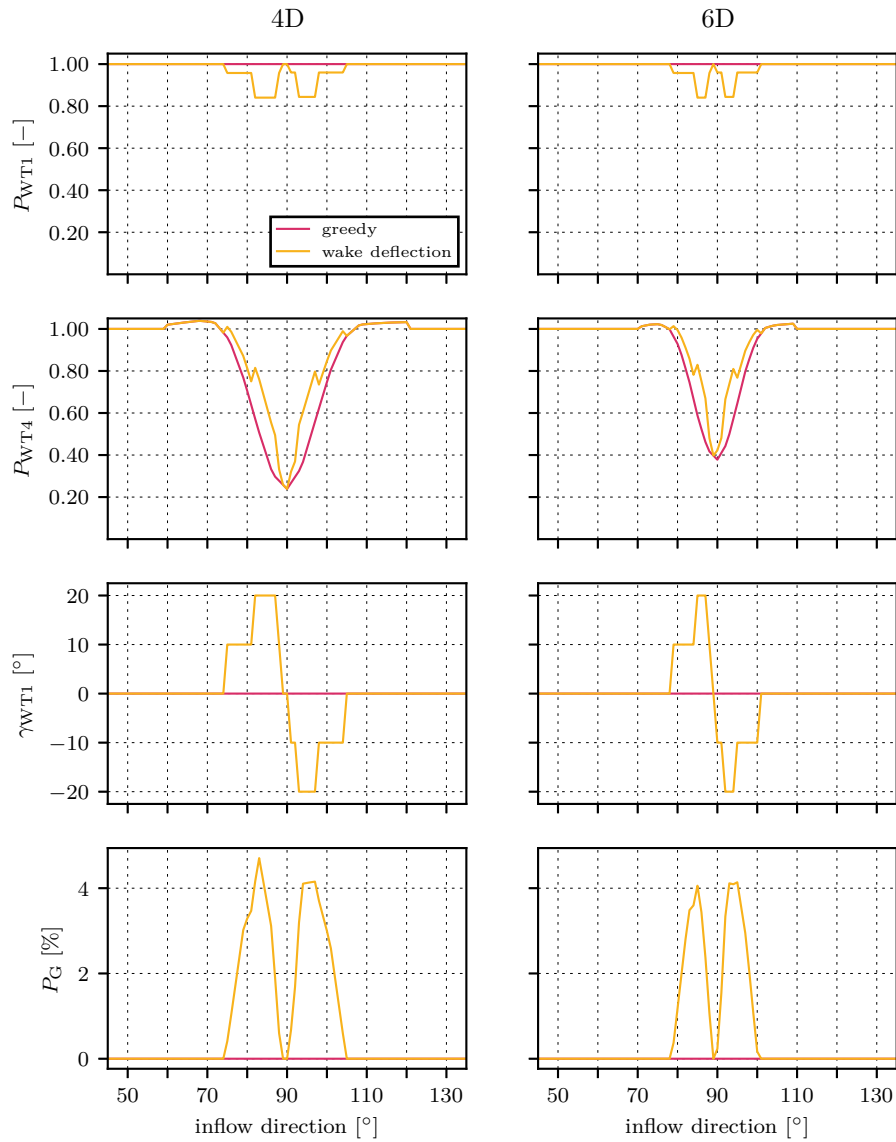


Figure 3.20: Power output P_{WT1} and P_{WT4} for a turbine spacing of 4D and 6D with-out yaw misalignment of *WT1* (greedy) and with an optimal yaw misalignment γ of *WT1* (wake deflection). P_G indicates the overall power gain of *WT1* and *WT4* for the case with wake deflection in comparison to the greedy control. The gain is determined with respect to the combined power of both turbines in free inflow conditions (two times 1834 kW).

lateral distances between the turbines in both cases are 130 m and 144 m, respectively. This indicates that even for minor partial wake conditions, wake deflection is beneficial. If we compare the overall power output of *WT1* and *WT4* with and without the application of wake deflection for the 30° and the 22° wide sectors of the *WF1* and *WF2* configuration in which yaw misalignment is beneficial, we obtain increases in power output of 2.54 % and 2.35 %, respectively. This is again in relation to the combined power of both turbines in undisturbed inflow.

In order to get a feeling for the comparability of our results, we referred to data from Gebraad et al. (2016). They used the high-fidelity framework SOWFA (Churchfield et al. (2012), Fleming et al. (2013a) and Fleming et al. (2013b)) which is based on OpenFOAM and *FAST* to perform simulations of two *NREL 5-MW* turbines that were modelled with the actuator line approach. It was investigated how different yaw misalignments of the upstream turbine affect the power output of both turbines which were $7D$ apart without any lateral displacement. The inflow conditions were similar to the ones used in our investigation with a mean hub height free stream wind speed of 8 ms^{-1} , a turbulence intensity of 6 % and a low roughness length of 0.001 m. In Table 3.8 the power outputs of both individual turbines and of both turbines combined are given. The data of Gebraad et al. (2016) was approximated from their Figure 2b and normalised with 1726 kW, the power output of the upstream turbine for $\gamma = 0^\circ$. The power outputs of the two individual turbines are referred to as $P_{1G}(\gamma)$, $P_{2G}(\gamma)$ for Gebraad et al. (2016) and $P_{1B}(\gamma)$, $P_{2B}(\gamma)$ for our investigation. $P_{1B}(\gamma)$ and $P_{2B}(\gamma)$ are based on $P_{WT1}(\gamma)$ and $P_{WT4}(6D, 90^\circ, \gamma)$ which were normalised with 1834 kW, the power output for free inflow conditions and $\gamma = 0^\circ$. The overall gains in P_{GB} and P_{GG} are determined according to Equation (3.28).

In general, a slightly higher power output of 1834 kW in comparison to 1726 kW is observed in the simulation performed by us. Due to the merely similar, but not identical inflow conditions, we consider the difference to be within the expected range. In addition, the power output of the downstream wind turbine ($P_{2B}(0^\circ) = 0.432$) in our investigation is below the one in the investigation of Gebraad et al. (2016) ($P_{2B}(0^\circ) = 0.482$). This is also in line with the slightly reduced distance between the upstream and the downstream turbines. Both results have in common that the loss at the upstream turbine is the same for positive and negative yaw angles. However, the results obtained in our investigation indicate larger losses. With respect to the power output of the downstream turbine, an asymmetric behaviour can be seen in both cases with higher power outputs being achieved for negative yaw misalignments of the upstream turbine. The relative power at the downstream turbine is much higher in the study of Gebraad et al.

Table 3.8: Comparison of the power outputs of the two-turbine test case of this investigation and the results that were published by Gebraad et al. (2016) - Figure 2b. The power outputs of the individual turbines ($P_{1B}(\gamma)$, $P_{2B}(\gamma)$, $P_{1G}(\gamma)$, $P_{2G}(\gamma)$) are normalised with the power output of the upstream turbine without the application of wake deflection. The overall gain of both wind turbines if wake deflection is applied in comparison to conventional greedy operation is indicated by P_{GB} and P_{GG} and was normalised with the combined power of both turbines in undisturbed inflow.

	Our investigation			Gebraad et al. (2016)		
γ	P_{1B}	P_{2B}	P_{GB}	P_{1G}	P_{2G}	P_{GG}
($^{\circ}$)	(-)	(-)	(%)	(-)	(-)	(%)
20	0.841	0.505	-4.30	0.888	0.529	-3.25
10	0.958	0.443	-1.55	0.967	0.483	-1.60
0	1.000	0.432	0.00	1.000	0.482	0.00
-10	0.960	0.480	0.40	0.965	0.555	1.90
-20	0.844	0.578	-0.50	0.888	0.662	3.40

(2016) with 0.662 compared to 0.578 for our study for the case with $\gamma = -20^{\circ}$. This characteristic affects whether the overall performance of the wind farm can be influenced by wake deflection. Whereas in both investigations (columns P_{GB} and P_{GG}) a loss is obtained for positive yaw angles, a gain of 2.0 % to 3.5 % is obtained by Gebraad et al. (2016) for negative yaw angles. This is in contrast to the results of our investigation in which almost no benefit is achieved with yaw deflection for this specific case of both turbines being perfectly in line. Due to the different models and only similar but not identical inflow conditions, it is difficult to determine the exact causes for the partially deviating results. That it is difficult to compare results from different sources in general becomes clear when looking at data from Churchfield et al. (2012). They used a very similar setup as Gebraad et al. (2016) which consisted of an LES approach with ACL turbine models and the integration of the aeroelastic code *FAST*. The setup of two *NREL 5-MW* turbines with 7D spacing is identical. Key characteristics of the inflow conditions include a hub height free stream wind speed of 8 ms^{-1} , a turbulence intensity of 6 % and a low roughness length of 0.001 m. These are very similar to the one of the *N08* wind field and virtually identical to the ones used in the investigations of Gebraad et al. (2016). Unfortunately, Churchfield et al. (2012) determined a power ratio of downstream turbine to upstream turbine of 0.56 (Table 2 in their paper) which is much

higher than the 0.432 and 0.482 obtained by us and by Gebraad, respectively. In order to better understand such differences, it can help to perform code-to-code comparison with the different models and well-defined boundary conditions. In the scope of the research project *IEA Wind Task 31 Phase 3* (Doubrawa et al. (2018)), such a code-to-code comparison is intended with the emphasis on wake development in different atmospheric boundary layers. In addition to the simulation results, field measurements are available which significantly increase the benefit of the comparison once again.

3.3.4.3 Loading

In Figure 3.21 the edgewise EB_{WT1} , EB_{WT4} and flapwise FB_{WT1} , FB_{WT4} damage equivalent blade loads of *WT1* and *WT4* for the *WF1* and *WF2* configurations of the test case with conventional greedy control and for wake deflection are shown. The corresponding tower base side-to-side TS_{WT1} , TS_{WT4} and tower base fore-aft TF_{WT1} , TF_{WT4} damage equivalent loads are plotted in Figure 3.22.

The results show that the application of yaw deflection leads to an increased loading at the upstream turbine for all investigated sensors with the exception of the edgewise blade loads for $\gamma < 0^\circ$. Due to the strong dependency on the blade masses and the number of revolutions, a rather limited impact of yaw misalignment on the edgewise DELs is observed. The increased DELs for $\gamma > 0^\circ$ and the reduction for $\gamma < 0^\circ$ is in line with the results of Damiani et al. (2018) obtained from simulations and field measurements.

Further data we approximated from Lee et al. (2012) gives us edgewise DELs of 6050 kNm and 5790 kNm for the upstream and downstream turbine, respectively. This is similar to the 5994 kNm (Table 3.5) and the 5894 kNm we got with our simulations. The value of the downstream turbine was extracted from the load map at a downstream position of 7D to agree with the setup of Lee et al. (2012) which is based on the data from Churchfield et al. (2012).

When analysing the flapwise DELs of *WT1*, increased loads occur for all cases with yaw misalignment. Maximum values are up to about 25 % higher. In addition, slightly higher loads are obtained for $\gamma > 0^\circ$ in comparison to the same γ in opposite direction. Recent results of Damiani et al. (2018) that are based on *FAST* simulations and field data support the general load increase that we obtained in cases with turbine yaw misalignment. However, our results are in contrast to the results published by Fleming et al. (2014) as they obtained a reduction of the out-of-plane DELs for $\gamma < 0^\circ$. Please note that they use an opposing definition of γ and that their out-of-plane DELs and our flapwise DELs represent the same sensors because the investigated cases are all below rated and no pitching takes place.

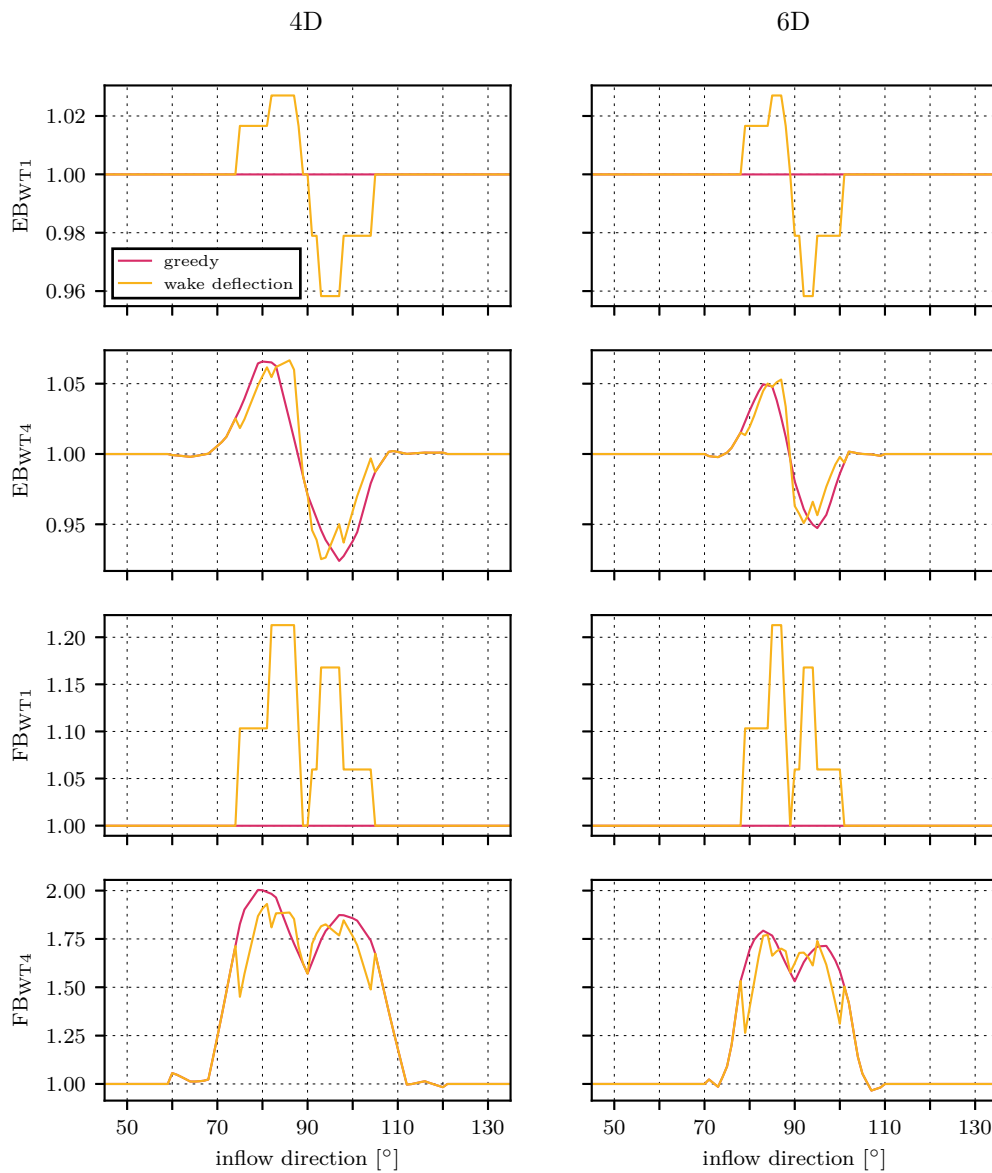


Figure 3.21: Edgewise EB_{WT1} , EB_{WT4} and flapwise FB_{WT1} , FB_{WT4} damage equivalent blade loads of $WT1$ and $WT4$ for the configurations presented in Figure 3.20.

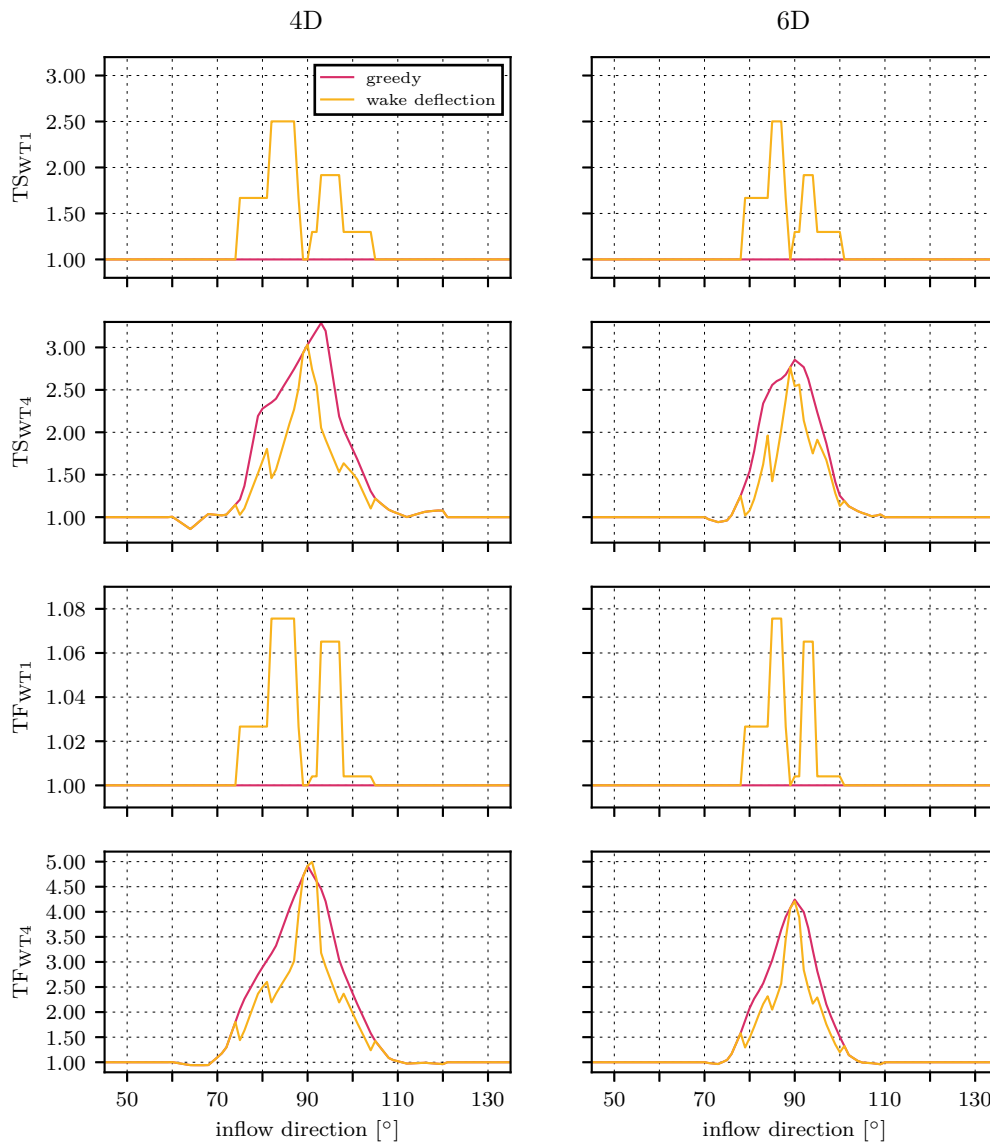


Figure 3.22: Tower base side-to-side TS_{WT1} , TS_{WT4} and tower base fore-aft TF_{WT1} , TF_{WT4} damage equivalent loads of $WT1$ and $WT4$ for the configurations presented in Figure 3.20.

At the downstream turbine *WT4*, even up to twice as high loads were measured in the wake in comparison to free inflow conditions for the *WF1* case. A reduction of the DELs is achieved if wake deflection is applied. Fleming et al. (2015) published results for the case of both turbines being in line with the inflow which show that yaw misalignment rather leads to increased DELs even at the downstream turbine (Figure 4 in their paper). Unfortunately, Fleming et al. (2015) did not publish any absolute DELs that we can use for comparison. At least for the case of normal operation without any wake deflection, we can get some reference data from Lee et al. (2012). It shows that the out-of-plane DELs of the downstream turbine are increased with respect to the turbine in free inflow conditions (Figure 10 in their paper). Unfortunately, the increase is on the order of 15 % and well below the 100 % that we determined in our study. Both absolute values for undisturbed inflow are comparable with them listing approximately 1400 kNm and us obtaining 1590 kNm (Table 3.5).

If we finally now look at the tower base side-to-side and tower base fore-aft DELs, a few more questions arise. Whereas the tower base fore-aft DELs of *WT1* are increasing by a maximum of 8 % in cases with yaw misalignment, a substantial increase of up to 250 % is seen for the tower base side-to-side DELs. For the downstream turbine *WT4*, even higher DELs of 500 % and 300 % are determined. A comparison of the tower DELs in case of no yaw misalignment with the results of Lee et al. (2012) does also reveal larger differences between the data. In our simulations, values of 1213 kNm and 3740 kNm are obtained for the tower base side-to-side and fore-aft DELs, respectively. The values of Lee et al. (2012) of 810 kNm and 2270 kNm are much lower. Their corresponding values for the downstream turbine are 1060 kNm and 3480 kNm, which reflect an increase of 31 % and 51 %.

The very high DELs of the downstream turbine *WT4* in comparison to *WT1* seem to be a general issue in our investigation. In addition, even the tower DELs of the upstream turbine seem to be quite high, whereas the blade DELs are comparable to the results of Lee et al. (2012). Due to a lack of further reference data, no final conclusions can be drawn at this stage.

3.3.4.4 Test case: Wind farms *WF1* and *WF2*

The results for the wind farms *WF1* and *WF2* (see Table 3.7, test cases *B1* and *B2*) are presented in Figure 3.23 and Figure 3.24, similarly to the ones for the sector analysis of *WT1* and *WT4*. Due to the symmetry of the conditions within the wind farm and the amount of data, we limit the output to the values of *WT1*.

In the first row of Figure 3.23, the power output of *WT1* is shown. At around 0°, 36.9° and 90°, downstream turbines are affected by its wake in both wind farm configura-

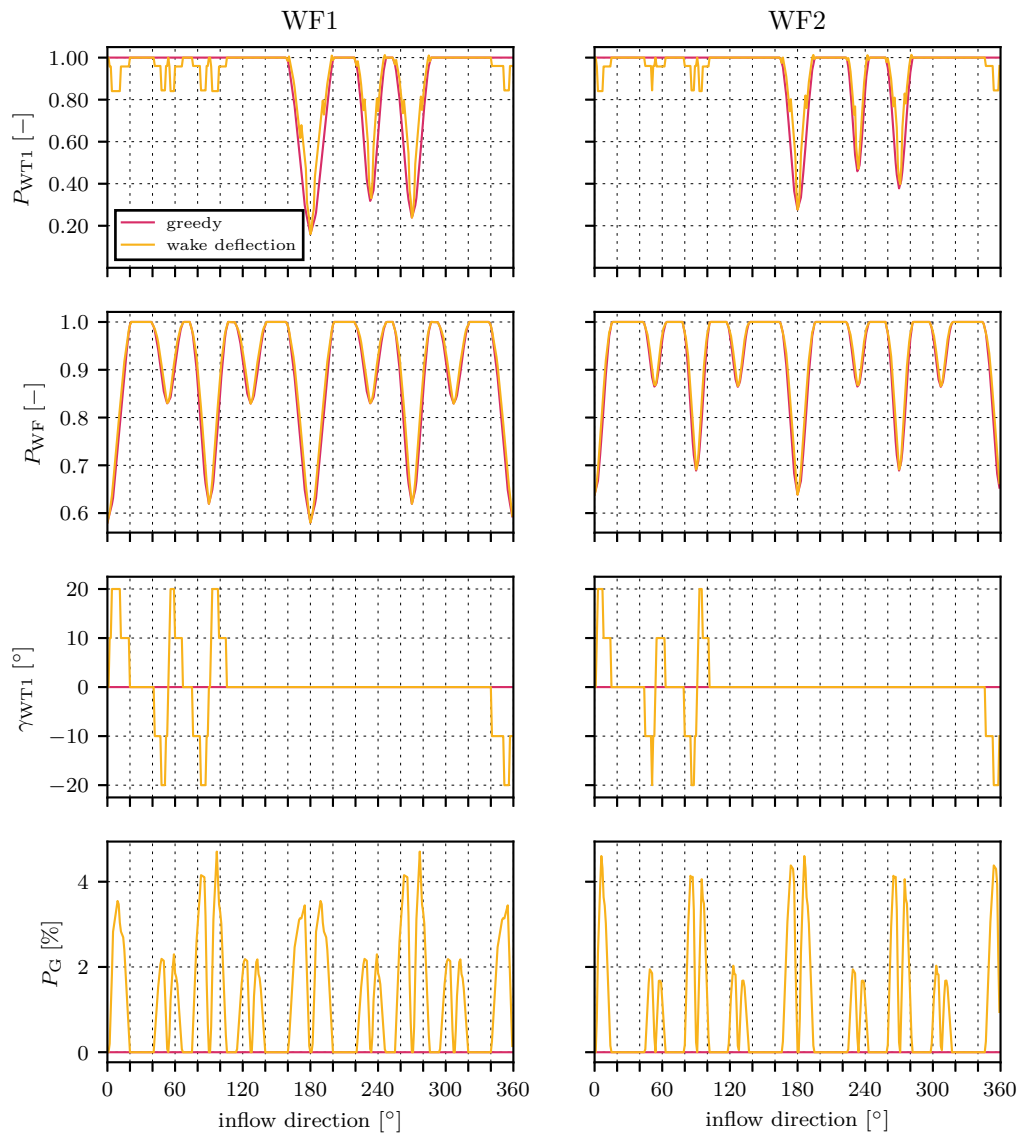


Figure 3.23: Power outputs of *WT1* (P_{WT1}) and the entire wind farms *WF1* and *WF2* with and without the application of yaw misalignment. The optimal yaw angle of *WT1* is indicated by γ_{WT1} . P_G indicates the overall power gain of the wind farm if wake deflection is applied. The gain is determined with respect to the combined power of both turbines in free inflow conditions (four times 1834 kW).

tions and wake deflection is applied. The corresponding yaw angles are shown in the third row of Figure 3.23. At inflow angles of 180° , 233.1° and 270° , *WT1* itself is exposed to wake conditions. The most severe wake conditions for *WT1* are caused by *WT2* and lead to a reduction of the power output below 30 %. For the wind farms, the largest reduction in power output to around 60 % is obtained for inflow directions of 0° and 180° due to the small spacing between *WT1/WT2* and *WT4/WT3*. The power outputs of the whole wind farms for each inflow direction are plotted in the second row of Figure 3.23. The values are normalised with four times the 1834 kW that one turbine yields in free inflow conditions (Table 3.5).

In the fourth row P_G is plotted, which indicates maximum gains of approximately 4.5 % for specific inflow directions. As in the analysis of the two turbines before (Equation 3.28), P_G was determined with respect to the combined power of all turbines in the wind farm at free inflow conditions, which equals four times 1834 kW.

Considering all inflow directions equally, 1.23 % and 0.90 % more power is yielded for *WF1* and *WF2*, respectively, if wake deflection with yaw misalignments of up to $\pm 20^\circ$ is applied for the investigated inflow conditions. If we concentrate only on the sectors in which deflection is used at any of the four wind turbines, we obtain gains of 1.98 % and 1.44 % for *WF1* and *WF2*, respectively. In *WF1*, wake deflection is being used for 62 % of the inflow directions, whereas in *WF2* it is only used in 46 % of the cases.

Please note that these numbers just give indications regarding the benefit of the application of wake deflection. In order to get more accurate figures for a particular wind farm, the annual wind direction and wind speed distribution of the site should be estimated or known so that the number of occurrences of each wake situation can be taken into account.

In Figure 3.24 the blade edgewise (EB_{WT1}), blade flapwise (FB_{WT1}), tower base side-to-side (TS_{WT1}) and tower base fore-aft (TF_{WT1}) DELs of *WT1* for both wind farm configurations *WF1* and *WF2* are shown. One graph indicates the results for conventional greedy control and one if wake deflection is applied.

With the exception of the edgewise DELs for negative yaw angle, the maximum DELs during yaw misalignment are less than the ones during wake exposure. As was to be expected from the results from Section 3.3.4.1, high tower loads are once again encountered in the wake in general and side-to-side during yawed operation.

For comparison we have determined the average DELs for the conventional greedy control case and for the optimised case with yaw deflection throughout all inflow directions (Table 3.9). We determined the averages following the approach used in Equation 3.17, thus considering the non-linear behaviour of the loading. The edgewise DELs

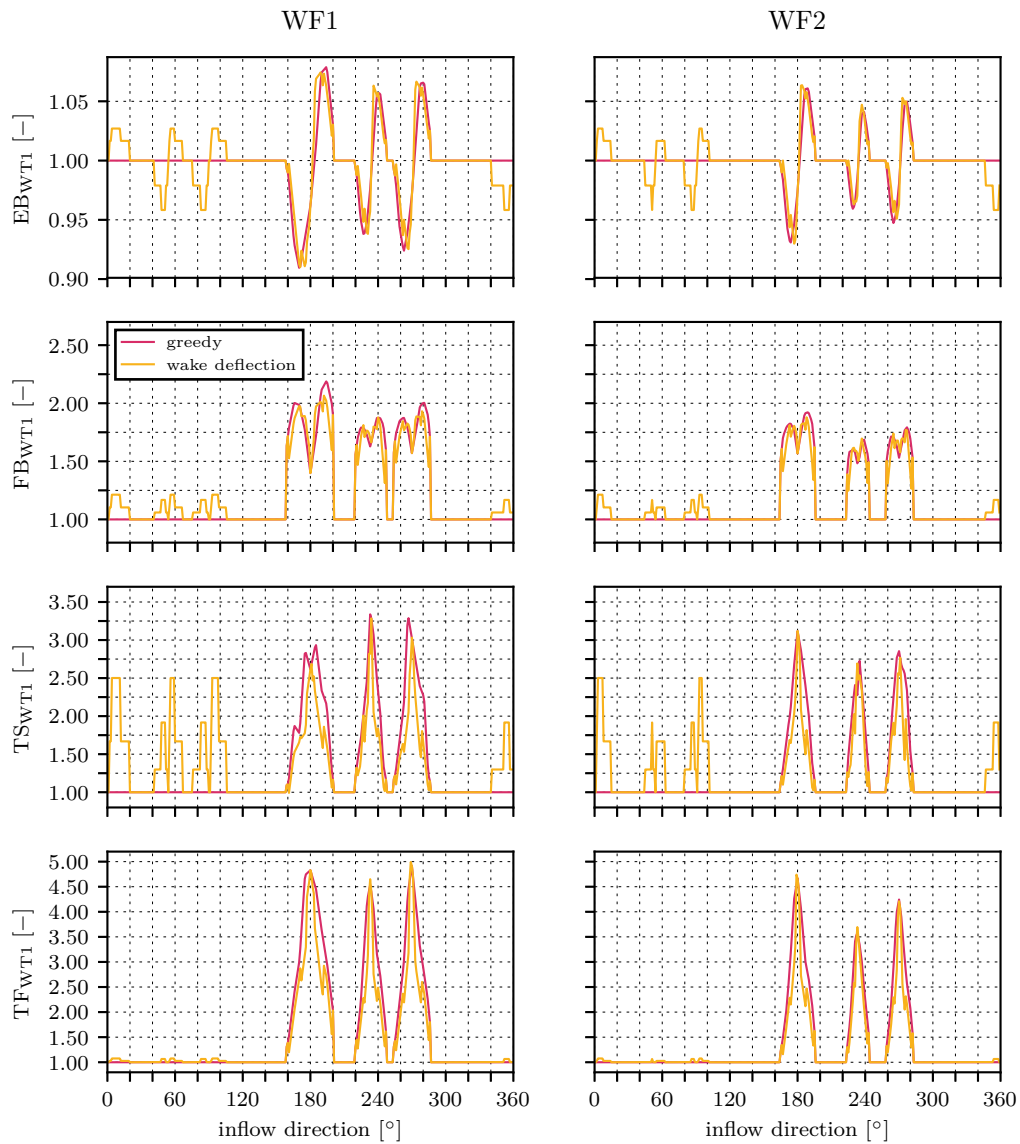


Figure 3.24: Edgewise EB_{WT1} , flapwise FB_{WT1} , tower base side-to-side TS_{WT1} and tower base fore-aft TF_{WT1} damage equivalent loads of $WT1$ for the investigation described in Figure 3.23.

do not show any increase or reduction due to their asymmetrical characteristics. For the flapwise DELs, the differences between the individual cases are on the order of 5 % with minimal higher loads on average if yaw misalignment is applied. The average increase in comparison to *WF1* being in free inflow only is on the order of 65 % for *WF1* and 45 % for *WF2* due to the impact of the three wake conditions.

The side-to-side DELs show a similar behaviour as the flapwise DELs. If yaw misalignment is being used, the DELs increase by 8 % for *WF1* and 5 % for *WF2*. Overall, the average DELs are above the ones of a turbine in free inflow by 63 % for *WF1* and 46 % for *WF2*. Even more severe are the results for the fore-aft DELs with increases of 134 % for *WF1* and 90 % for *WF2* in comparison to free inflow. However, if wake deflection is applied, the DELs are reduced to increases of 101 % for *WF1* and 66 % for *WF2*. This confirms the inconsistent effect that the application of wake deflection has on the turbine loading.

As for the power output, the results concerning the loading can only give some indication. On the one hand, this is due to the issues in determining the tower loads and, on the other hand, due to the idealised inflow distribution. The latter allows a fundamental analysis of the occurring conditions, but does not correspond to the site-specific inflow dynamics usually observed in the field.

3.4 Conclusion

We used a simulation approach that we refer to as wake mapping for estimating the changes in power and loading of wind turbines in a wind farm with and without wake deflection being used. In a first step, large-eddy simulations with one turbine were performed for several neutrally stratified atmospheric boundary layers. The turbine was modelled based on the ADM-R approach. In a second step, wind fields were extracted from the LES generated wake flow at several longitudinal and lateral downstream distances. Finally, these wind fields were used as inputs for aeroelastic simulations with *FAST* to obtain power and loading information at all the different locations. We refer to the resulting matrices as power and load maps. This approach has the benefit of being computationally much less demanding than performing comprehensive LES simulations for all turbine configurations but obviously, it cannot entirely represent the complex turbine interactions in a wind farm to full extent.

Besides the basic analysis of the presented method and the obtained results, further individual elements such as the characteristics of the generated large-eddy wind fields were examined in detail to better understand the uncertainties associated with the investigation.

Table 3.9: Average DELs of *WT1* throughout all inflow directions in *WF1* and *WF2* configurations with respect to a turbine in free inflow only. The control column indicates whether conventional greedy control or wake deflection was applied.

DEL	control	WF1	WF2
		(-)	(-)
EB	greedy	1.00	1.00
	yaw	1.00	1.00
FB	greedy	1.66	1.47
	yaw	1.60	1.43
TS	greedy	1.63	1.46
	yaw	1.59	1.44
TF	greedy	2.34	1.90
	yaw	2.01	1.66

One first thing to keep in mind when using LES wind fields for load estimation is that the available frequency range of wind speed fluctuations in the inflow is limited as it is linked to the chosen grid spacing. Unfortunately, an arbitrarily small grid spacing cannot be used as it leads to a significant increase of the required computational resources. To investigate how the turbine loads were affected for our setup, we generated stochastic wind fields with similar average statistical characteristics (e.g. mean wind speed, turbulence intensity) as the wind fields that were extracted from the LES. In a first comparison, both types of wind fields were used to determine the loads of a wind turbine in undisturbed inflow. Despite the different properties of the stochastic wind fields and those of the LES in terms of frequency resolution and representation of the physical characteristics, the obtained load data showed a good agreement.

In a second investigation, several wind fields with a reduced frequency range were derived from the stochastic baseline wind fields. It turned out that the edgewise and flapwise DELs differed by less than 2 % from the 32 Hz baseline case if the low-pass filtered wind fields contained frequency content of up to 2 Hz. In contrast, the tower base fore-aft and side-to-side DELs required a higher frequency content of up to 4 Hz to stay within the same 2 % limit. Below this value, a rapid reduction of the loads much faster than for the blade loads was observed. One reason for the two different characteristics could be that the blades perform a rotational sampling of the inflow. The effect of the

rotational sampling of the blades is transferred to the tower through the 3P frequency and the harmonics but no sampling takes place through the tower itself.

Furthermore, we would like to emphasize that in the cases examined by us, the 2P frequency of the rotor and the first natural frequency of the tower matched. This special case leads to strongly increased tower loads of the examined wind turbines. For further investigations, we suggest a reassessment of the structural turbine design, its modelling in FAST and potentially a different operating point at which this specific scenario is avoided.

With regard to the characteristics of the large-eddy reference wind fields, our results show that these are not completely homogeneous despite the long initialization phase. This was tested by performing *FAST* simulations with wind fields that were extracted at various locations in the undisturbed inflow. Deviations in the power output of up to 8 % from the mean power output of all simulations were observed. This variability must be taken into account when comparing results and drawing conclusions from only a small number of simulations.

To calculate the power output of the wind turbines, we have used two methods. At first, we extracted wind fields from the large-eddy wind fields at the locations of interest and used them as input for *FAST* simulations. For the second approach, we determined the rotor equivalent wind speed (REWS) of a turbine at a certain location and used its power curve to obtain the power output for the given conditions. To ensure reproducibility and comparability, the power curve was determined for uniform inflow conditions throughout the rotor area. With the simplistic and easy to use REWS approach, the absolute power was always above the one determined by *FAST*. To investigate how both of the employed methods put the power of an upstream and downstream turbine into perspective, we compared the REWS and *FAST* power outputs that were normalised with the corresponding values for undisturbed inflow. Differences of more than 10 % were obtained in the near wake, with the REWS-based values being higher. For larger downstream distances the differences decreased. Overall, the REWS values in the tested form only serve as an upper estimate of the power characteristics. If more detailed information is required, we suggest basing the REWS-approach on a power curve that was derived from turbulent inflow conditions that are more similar to the investigated ones. However, in the context of this study, this approach was not further pursued.

In order to put the wake mapping approach into practice, various test scenarios were developed with the focus being on two wind farm layouts, each consisting of four turbines arranged in a rectangle. For these cases, the power outputs and loading of

the individual turbines were determined for all inflow directions over the full circle of 360° in steps of 1° . Wake situations were taken into account and evaluated based on the established power and load maps. In addition to conventional greedy turbine operation, wake deflection was applied and the yaw angles of the wind turbines were optimised for each configuration. In each case, the goal was to maximize the combined power output of the wind turbines involved. The considered yaw angles were 0° , $\pm 10^\circ$ and $\pm 20^\circ$ to limit the number of simulations and to assess situations that could also be implemented in the field with current equipment. The largest yaw offset of $\pm 20^\circ$ resulted in a power loss of just under 16 % for the misaligned upstream wind turbine with respect to its power output for the same conditions without yaw misalignment. Nevertheless, even these seemingly unfavourable operating points of the upstream turbine have proven to be beneficial for certain inflow configurations in wind farms. As shown in other studies, we were also able to demonstrate that the application of wake deflection leads to an increase of the overall power output for the investigated conditions. For both wind farms, power output gains of approximately 4.5 % were achieved for individual situations in relation to the combined power of the two wind farms in undisturbed inflow. Due to the larger distances between the turbines, wake deflection was used for fewer inflow directions in the test wind farm *WF2* than in *WF1* as it otherwise did not result in an improved power output. When taking only those inflow directions into account in which wake deflection was applied, overall gains of 1.98 % and 1.44 %, relative to the combined power of all turbines in the wind farm at undisturbed inflow conditions, were achieved for wind farm *WF1* and *WF2*, respectively.

No uniform picture emerged with regard to the loading. On the one hand, the loads on the waked wind turbine decreased when the upstream turbine applied wake deflection. On the other hand, the loads on the yaw misaligned turbine increased in parallel in almost all cases. Depending on the magnitude of both changes, we observed an overall increase (e.g. tower base side-to-side DELs) or decrease (e.g. tower base fore-aft DELs). For the blade loads, virtually no change was observed. Due to the different characteristics of the load sensors, an optimised wind farm operation with regard to the total loads of all sensors does therefore not seem feasible according to our current state of knowledge. Whether this changes for inflow conditions in which the natural frequency of the tower does not match the 2P frequency should be assessed in further investigations.

Finally, we conclude that with the developed approach it was possible for us to gain further insight in how wake deflection affects the loading of wind turbines in a wind

farm. A comparable investigation with traditional LES would have required a large number of computationally demanding individual simulations and therefore is usually only feasible for very specific research purposes. Nevertheless, it is certainly advisable to further investigate how much the results of considering the downstream turbine only virtually differ from those in which upstream and downstream turbines are both simulated with LES. Moreover, our approach reaches its limits when turbine wakes interact or complex wind farm flows develop. Besides these fundamental limitations of the approach, we think it would be useful to use the wake maps as an input for the robust control algorithm suggested by Rott et al. (2018). It considers dynamic wind direction changes of the inflow and inaccuracies in the determination of the wind direction and therefore, should result in even more realistic predictions.

Last but not least, in order to guarantee the quality of the results, we recommend regular code-to-code comparison and, if possible, comparisons with field data as it is for example carried out in the research project *IEA Wind Task 31 Phase 3*. Results from various publications partially differ noticeably and it would be good to know to what extent these differences can be attributed to the chosen boundary conditions, model assumptions or other reasons. In addition, it would help to learn more about the strengths and weaknesses of individual simulation models.

Acknowledgement

This work was partially funded by the Federal Ministry for Economic Affairs and Energy (BMWi) according to a resolution by the German Federal Parliament (project *WIMS-Cluster*, FKZ 0324005). In addition, I would like to thank my colleagues Dr. Gerald Steinfeld, Andreas Rott and Frederik Berger for their valuable feedback and overall support.

3.A Appendix A - Parameter files

Listing 3.1: Reference.TurbSimInputFile.inp

TurbSim Input File. Valid for TurbSim v1.50, 25-Sep-2009

```

-----Runtime Options-----
PARAM_SEED      RandSeed1      - First random seed (-2147483648 to 2147483647)
RANLUX          RandSeed2      - Second random seed (-2147483648 to 2147483647) for int...
False           WrBHHTP        - Output hub-height turbulence parameters in binary form...
False           WrFHHTP        - Output hub-height turbulence parameters in formatted f...
False           WrADHH         - Output hub-height time-series data in AeroDyn form?
(...)
False           WrADFF         - Output full-field time-series data in TurbSim/AeroDyn ...
True            WrBLFF         - Output full-field time-series data in BLADED/AeroDyn f...
False           WrADTWR        - Output tower time-series data? (Generates RootName.twr...
False           WrFMFFF         - Output full-field time-series data in formatted (reada...
FALSE           WrACT          - Output coherent turbulence time steps in AeroDyn form?...
True            Clockwise      - Clockwise rotation looking downwind? (used only for fu...
2              ScaleIEC       - Scale IEC turbulence models to exact target standard d...

-----Turbine/Model Specifications-----
31              NumGrid_Z      - Vertical grid-point matrix dimension
31              NumGrid_Y      - Horizontal grid-point matrix dimension
0.03125         TimeStep       - Time step [seconds]
700             AnalysisTime  - Length of analysis time series [seconds] (program will...
700             UsableTime    - Usable length of output time series [seconds] (program...
90              HubHt         - Hub height [m] (should be > 0.5*GridHeight)
150             GridHeight    - Grid height [m]
150             GridWidth     - Grid width [m] (should be >= 2*(RotorRadius+ShaftLengt...
0               VFlowAng     - Vertical mean flow (uptilt) angle [degrees]
0               HFlowAng     - Horizontal mean flow (skew) angle [degrees]

-----Meteorological Boundary Conditions-----
"IECKAI"        TurbModel      - Turbulence model ("IECKAI"=Kaimal, "IECVKM"=von Karman...
"1-ED3"         IEStandard    - Number of IEC 61400-x standard (x=1,2, or 3 with optio...
PARAM_TURB      IECturbc      - IEC turbulence characteristic ("A", "B", "C" or the tu...
"NTM"           IEC_WindType   - IEC turbulence type ("NTM"=normal, "xETM"=extreme turb...
default         ETMc          - IEC Extreme Turbulence Model "c" parameter [m/s]
"PL"            WindProfileType - Wind profile type ("JET", "LOG"=logarithmic, "PL"=power ...
PARAM_ZREF      RefHt         - Height of the reference wind speed [m]
PARAM_UREF      URef         - Mean (total) wind speed at the reference height [m/s] ...
default         ZJetMax      - Jet height [m] (used only for JET wind profile, valid ...
PARAM_PEXP      PLExp        - Power law exponent [-] (or "default")
0.03            Z0           - Surface roughness length [m] (or "default")

-----Non-IEC Meteorological Boundary Conditions-----
default         Latitude    - Site latitude [degrees] (or "default")
0.05            RICH_NO      - Gradient Richardson number
default         UStar       - Friction or shear velocity [m/s] (or "default")
default         ZI          - Mixing layer depth [m] (or "default")
default         PC_UW       - Hub mean u'w' Reynolds stress (or "default")
default         PC_UV       - Hub mean u'v' Reynolds stress (or "default")
default         PC_VW       - Hub mean v'w' Reynolds stress (or "default")
default         IncDec1     - u-component coherence parameters (e.g. "10.0
0.3e-3" ...
default         IncDec2     - v-component coherence parameters (e.g. "10.0
0.3e-3" ...
default         IncDec3     - w-component coherence parameters (e.g. "10.0
0.3e-3" ...
default         CohExp      - Coherence exponent (or "default")

-----Coherent Turbulence Scaling Parameters-----

```

```
"M:\coh_events\eventdata" CTEventPath - Name of the path where event data files are loc...
"Random" CTEventFile - Type of event files ("LES", "DNS", or "RANDOM")
true Randomize - Randomize the disturbance scale and locations? (true/f...
1.0 DistScl - Disturbance scale (ratio of wave height to rotor disk)...
0.5 CTLy - Fractional location of tower centerline from right (lo...
0.5 CTLz - Fractional location of hub height from the bottom of t...
30.0 CTStartTime - Minimum start time for coherent structures in RootName...
```

```
=====
NOTE: Do not add or remove any lines in this file!
=====
```

Listing 3.2: NRELOffshrBslne5MW_Offshore.fst

```

----- FAST INPUT FILE -----
NREL 5.0 MW Baseline Wind Turbine for Use in Offshore Analysis.
Properties from Dutch Offshore Wind Energy Converter (DOWEC) 6MW Pre-Design (10046_009.pdf) ...
----- SIMULATION CONTROL -----
False      Echo          - Echo input data to "echo.out" (flag)
1          ADAMSPrp    - ADAMS preprocessor mode {1: Run FAST, 2: use FAST as a preprocesso...
1          AnalMode  - Analysis mode {1: Run a time-marching simulation, 2: create a peri...
3          NumBl     - Number of blades (-)
700.0     TMax       - Total run time (s)
0.02     DT        - Integration time step (s)
----- TURBINE CONTROL -----
0          YCMode    - Yaw control mode {0: none, 1: user-defined from routine UserYawCon...
0.0       TYCon     - Time to enable active yaw control (s) [unused when YCMode=0]
1          PCMode    - Pitch control mode {0: none, 1: user-defined from routine PitchCnt...
0.0       TPCOn     - Time to enable active pitch control (s) [unused when PCMode=0]
2          VSContrl  - Variable-speed control mode {0: none, 1: simple VS, 2: user-define...
9999.9   VS_RtGnSp  - Rated generator speed for simple variable-speed generator control ...
9999.9   VS_RtTq    - Rated generator torque/constant generator torque in Region 3 for s...
9999.9   VS_Rgn2K   - Generator torque constant in Region 2 for simple variable-speed ge...
9999.9   VS_SlPc    - Rated generator slip percentage in Region 2 1/2 for simple variabl...
2          GenModel  - Generator model {1: simple, 2: Thevenin, 3: user-defined from rout...
True     GenTiStr   - Method to start the generator {T: timed using TimGenOn, F: generat...
True     GenTiStp  - Method to stop the generator {T: timed using TimGenOf, F: when gen...
9999.9   SpdGenOn  - Generator speed to turn on the generator for a startup (HSS speed)...
0.0      TimGenOn  - Time to turn on the generator for a startup (s) [used only when Ge...
9999.9   TimGenOf  - Time to turn off the generator (s) [used only when GenTiStp=True]
2          HSSBrMode - HSS brake model {1: simple, 2: user-defined from routine UserHSSBr...
0.0      THSSBrDp  - Time to initiate deployment of the HSS brake (s)
9999.9   TiDynBrk  - Time to initiate deployment of the dynamic generator brake [CURREN...
9999.9   TTPBrDp(1) - Time to initiate deployment of tip brake 1 (s)
9999.9   TTPBrDp(2) - Time to initiate deployment of tip brake 2 (s)
9999.9   TTPBrDp(3) - Time to initiate deployment of tip brake 3 (s) [unused for 2 blade...
9999.9   TBDepISp(1) - Deployment-initiation speed for the tip brake on blade 1 (rpm)
9999.9   TBDepISp(2) - Deployment-initiation speed for the tip brake on blade 2 (rpm)
9999.9   TBDepISp(3) - Deployment-initiation speed for the tip brake on blade 3 (rpm) [un...
9999.9   TYawManS  - Time to start override yaw maneuver and end standard yaw control (...
9999.9   TYawManE  - Time at which override yaw maneuver reaches final yaw angle (s)
0.0      NacYawF   - Final yaw angle for yaw maneuvers (degrees)
9999.9   TPitManS(1) - Time to start override pitch maneuver for blade 1 and end standard...
9999.9   TPitManS(2) - Time to start override pitch maneuver for blade 2 and end standard...
9999.9   TPitManS(3) - Time to start override pitch maneuver for blade 3 and end standard...
9999.9   TPitManE(1) - Time at which override pitch maneuver for blade 1 reaches final pi...
9999.9   TPitManE(2) - Time at which override pitch maneuver for blade 2 reaches final pi...
9999.9   TPitManE(3) - Time at which override pitch maneuver for blade 3 reaches final pi...
0.0      BlPitch(1) - Blade 1 initial pitch (degrees)
0.0      BlPitch(2) - Blade 2 initial pitch (degrees)
0.0      BlPitch(3) - Blade 3 initial pitch (degrees) [unused for 2 blades]
0.0      BlPitchF(1) - Blade 1 final pitch for pitch maneuvers (degrees)
0.0      BlPitchF(2) - Blade 2 final pitch for pitch maneuvers (degrees)
0.0      BlPitchF(3) - Blade 3 final pitch for pitch maneuvers (degrees) [unused for 2 bl...
----- ENVIRONMENTAL CONDITIONS -----
9.80665  Gravity   - Gravitational acceleration (m/s^2)
----- FEATURE FLAGS -----
True     FlapDOF1   - First flapwise blade mode DOF (flag)
True     FlapDOF2   - Second flapwise blade mode DOF (flag)
True     EdgeDOF    - First edgewise blade mode DOF (flag)
False    TeetDOF    - Rotor-teeter DOF (flag) [unused for 3 blades]
True     DrTrDOF    - Drivetrain rotational-flexibility DOF (flag)
True     GenDOF     - Generator DOF (flag)
True     YawDOF     - Yaw DOF (flag)
True     TwFADOF1   - First fore-aft tower bending-mode DOF (flag)
True     TwFADOF2   - Second fore-aft tower bending-mode DOF (flag)

```

```

True      TwSSDOF1  - First side-to-side tower bending-mode DOF (flag)
True      TwSSDOF2  - Second side-to-side tower bending-mode DOF (flag)
True      CompAero  - Compute aerodynamic forces (flag)
False     CompNoise - Compute aerodynamic noise (flag)
-----
0.0       OoPDefl   - Initial out-of-plane blade-tip displacement (meters)
0.0       IPDefl   - Initial in-plane blade-tip deflection (meters)
0.0       TeetDefl  - Initial or fixed teeter angle (degrees) [unused for 3 ...
0.0       Azimuth  - Initial azimuth angle for blade 1 (degrees)
9.0       RotSpeed  - Initial or fixed rotor speed (rpm)
PARAM_YAW_ANGLE NacYaw    - Initial or fixed nacelle-yaw angle (degrees)
0.0       TTDspFA   - Initial fore-aft tower-top displacement (meters)
0.0       TTDspSS   - Initial side-to-side tower-top displacement (meters)
-----
TURBINE CONFIGURATION -----
63.0     TipRad     - The distance from the rotor apex to the blade tip (meters)
1.5      HubRad     - The distance from the rotor apex to the blade root (meters)
1        PSpnELN    - Number of the innermost blade element which is still part of the p...
0.0     UndSling   - Undersling length [distance from teeter pin to the rotor apex] (me...
0.0     HubCM      - Distance from rotor apex to hub mass [positive downwind] (meters)
-5.01910 OverHang   - Distance from yaw axis to rotor apex [3 blades] or teeter pin [2 b...
1.9     NacCMxn    - Downwind distance from the tower-top to the nacelle CM (meters)
0.0     NacCMyn    - Lateral distance from the tower-top to the nacelle CM (meters)
1.75    NacCMzn    - Vertical distance from the tower-top to the nacelle CM (meters)
87.6    TowerHt    - Height of tower above ground level [onshore] or MSL [offshore] (me...
1.96256 Twr2Shft    - Vertical distance from the tower-top to the rotor shaft (meters)
0.0     TwrRBHt    - Tower rigid base height (meters)
-5.0    ShftTilt   - Rotor shaft tilt angle (degrees)
0.0     Delta3     - Delta-3 angle for teetering rotors (degrees) [unused for 3 blades]
-2.5    PreCone(1) - Blade 1 cone angle (degrees)
-2.5    PreCone(2) - Blade 2 cone angle (degrees)
-2.5    PreCone(3) - Blade 3 cone angle (degrees) [unused for 2 blades]
0.0     AzimBlUp   - Azimuth value to use for I/O when blade 1 points up (degrees)
-----
MASS AND INERTIA -----
0.0     YawBrMass  - Yaw bearing mass (kg)
240.00E3 NacMass    - Nacelle mass (kg)
56.78E3  HubMass    - Hub mass (kg)
0.0     TipMass(1) - Tip-brake mass, blade 1 (kg)
0.0     TipMass(2) - Tip-brake mass, blade 2 (kg)
0.0     TipMass(3) - Tip-brake mass, blade 3 (kg) [unused for 2 blades]
2607.89E3 NacYIner    - Nacelle inertia about yaw axis (kg m^2)
534.116  GenIner    - Generator inertia about HSS (kg m^2)
115.926E3 HubIner    - Hub inertia about rotor axis [3 blades] or teeter axis [2 blades] ...
-----
DRIVETRAIN -----
100.0    GBoxEff    - Gearbox efficiency (%)
94.4     GenEff     - Generator efficiency [ignored by the Thevenin and user-defined gen...
97.0     GBRatio    - Gearbox ratio (-)
False    GBRevers   - Gearbox reversal {T: if rotor and generator rotate in opposite dir...
28.1162E3 HSSBrTqF    - Fully deployed HSS-brake torque (N-m)
0.6      HSSBrDT     - Time for HSS-brake to reach full deployment once initiated (sec) [...
"Dummy"  DynBrkFi    - File containing a mech-gen-torque vs HSS-speed curve for a dynamic...
867.637E6 DTTorSpr   - Drivetrain torsional spring (N-m/rad)
6.215E6  DTTorDmp    - Drivetrain torsional damper (N-m/(rad/s))
-----
SIMPLE INDUCTION GENERATOR -----
9999.9   SIG_SlPc    - Rated generator slip percentage (%) [used only when VSContrl=0 and...
9999.9   SIG_SySp    - Synchronous (zero-torque) generator speed (rpm) [used only when VS...
9999.9   SIG_RtTq    - Rated torque (N-m) [used only when VSContrl=0 and GenModel=1]
9999.9   SIG_PORT    - Pull-out ratio (Tpullout/Trated) (-) [used only when VSContrl=0 an...
-----
THEVENIN-EQUIVALENT INDUCTION GENERATOR -----
9999.9   TEC_Freq    - Line frequency [50 or 60] (Hz) [used only when VSContrl=0 and GenM...
9998     TEC_NPol    - Number of poles [even integer > 0] (-) [used only when VSContrl=0 ...
9999.9   TEC_SRes    - Stator resistance (ohms) [used only when VSContrl=0 and GenModel=2]
9999.9   TEC_RRes    - Rotor resistance (ohms) [used only when VSContrl=0 and GenModel=2]
9999.9   TEC_VLL     - Line-to-line RMS voltage (volts) [used only when VSContrl=0 and Ge...
9999.9   TEC_SLR     - Stator leakage reactance (ohms) [used only when VSContrl=0 and Gen...
9999.9   TEC_RLR     - Rotor leakage reactance (ohms) [used only when VSContrl=0 and GenM...

```

```

9999.9      TEC_MR      - Magnetizing reactance (ohms) [used only when VSContrl=0 and GenMod...
-----
0          PtfmModel  - Platform model {0: none, 1: onshore, 2: fixed bottom offshore, 3: ...
"Dummy"    PtfmFile    - Name of file containing platform properties (quoted string) [unuse...
-----
20         TwrNodes   - Number of tower nodes used for analysis (-)
"../NRELOffshrBslne5MW_Tower_Onshore.dat"      TwrFile
- Name of file containing to...
-----
9028.32E6  YawSpr     - Nacelle-yaw spring constant (N-m/rad)
19.16E6    YawDamp    - Nacelle-yaw damping constant (N-m/(rad/s))
0.0        YawNeut   - Neutral yaw position--yaw spring force is zero at this yaw (degree...
-----
False      Furling      - Read in additional model properties for furling turbine (flag)
"Dummy"    FurlFile    - Name of file containing furling properties (quoted string) [unused...
-----
0          TeetMod    - Rotor-teeter spring/damper model {0: none, 1: standard, 2: user-de...
0.0        TeetDmpP   - Rotor-teeter damper position (degrees) [used only for 2 blades and...
0.0        TeetDmp    - Rotor-teeter damping constant (N-m/(rad/s)) [used only for 2 blade...
0.0        TeetCDmp   - Rotor-teeter rate-independent Coulomb-damping moment (N-m) [used o...
0.0        TeetSStP   - Rotor-teeter soft-stop position (degrees) [used only for 2 blades ...
0.0        TeetHStP   - Rotor-teeter hard-stop position (degrees) [used only for 2 blades ...
0.0        TeetSSSp   - Rotor-teeter soft-stop linear-spring constant (N-m/rad) [used only...
0.0        TeetHSSp   - Rotor-teeter hard-stop linear-spring constant (N-m/rad) [used only...
-----
0.0        TBDrConN   - Tip-brake drag constant during normal operation, Cd*Area (m^2)
0.0        TBDrConD   - Tip-brake drag constant during fully-deployed operation, Cd*Area (...
0.0        TpBrDT     - Time for tip-brake to reach full deployment once released (sec)
-----
"../NRELOffshrBslne5MW_Blade.dat"              BldFile(1)
- Name of file containing pr...
"../NRELOffshrBslne5MW_Blade.dat"              BldFile(2)
- Name of file containing pr...
"../NRELOffshrBslne5MW_Blade.dat"              BldFile(3)
- Name of file containing pr...
-----
"../NRELOffshrBslne5MW_AeroDyn.ipt"            ADFile
- Name of file containing Aer...
-----
"Dummy"    NoiseFile   - Name of file containing aerodynamic noise input parameters (quoted...
-----
"../NRELOffshrBslne5MW_ADAMSSpecific.dat"      ADAMSFile
- Name of file containing AD...
-----
"../NRELOffshrBslne5MW_Linear.dat"             LinFile
- Name of file containing FA...
-----
True       SumPrint   - Print summary data to "<RootName>.fsm" (flag)
1          OutFileFmt  - Format for tabular (time-marching) output file(s) (1: text file [<...
True       TabDelim    - Generate a tab-delimited tabular output file. (flag)
"ES10.3E2" OutFmt     - Format used for tabular output except time.
Resulting field shoul...
0.0        TStart     - Time to begin tabular output (s)
1          DecFact    - Decimation factor for tabular output {1: output every time step} (...
1.0        SttsTime   - Amount of time between screen status messages (sec)
-3.09528  NcIMUxn         - Downwind distance from the tower-top to the nacelle IMU (meters)
0.0        NcIMUyn         - Lateral distance from the tower-top to the nacelle IMU (meters)
2.23336   NcIMUzn         - Vertical distance from the tower-top to the nacelle IMU (meters)
1.912     ShftGagL     - Distance from rotor apex [3 blades] or teeter pin [2 blades] to sh...
0         NTwGages     - Number of tower nodes that have strain gages for output [0 to 9] (...
          TwrGagNd     - List of tower nodes that have strain gages [1 to TwrNodes] (-) [un...
3         NBlGages     - Number of blade nodes that have strain gages for output [0 to 9] (...
5,9,13    BldGagNd         - List of blade nodes that have strain gages [1 to BldNodes] (-) [un...
          OutList     - The next line(s) contains a list of output parameters.
See OutLis...

```



```

"WindVxi , WindVyi , WindVzi" - Longitudinal, lateral, and vertical wind speeds
"GenPwr , GenTq" - Electrical generator power and torque
"RotThrust, RotTorq, RotPwr"
"RotCq, RotCp, RotCt"
"BldPitch1" - Blade 1 pitch angle
"Azimuth , YawPos" - Blade 1 azimuth angle
"RotSpeed , GenSpeed , TSR" - Low-speed shaft and high-speed shaft speeds
"OoPDefl1 , IPDefl1 , TwstDefl1" - Blade 1 out-of-plane and in-plane deflections and ...
"TTDspFA , TTDspSS , TTDspTwst" - Tower fore-aft and side-to-side displacements and t...
"Spn2MLxb1, Spn2MLyb1" - Blade 1 local edgewise and flapwise bending moment...
"RootFxc1 , RootFyc1 , RootFzc1" - Out-of-plane shear, in-plane shear, and axial forc...
"RootMxc1 , RootMyc1 , RootMzc1" - In-plane bending, out-of-plane bending, and pitchi...
"RootMxb1 , RootMyb1" - Blade 1 edgewise and flapwise root bending moments
"RotTorq , LSSGagMya, LSSGagMza" - Rotor torque and low-speed shaft 0- and 90-bending...
"LSSGagMys, LSSGagMzs" - Nonrotating low-speed shaft 0- and 90-bending mome...
"YawBrFxp , YawBrFyp , YawBrFzp" - Fore-aft shear, side-to-side shear, and vertical f...
"YawBrMxp , YawBrMyp , YawBrMzp" - Side-to-side bending, fore-aft bending, and yaw mo...
"YawBrMxn , YawBrMyn , YawBrMzn" - Rotating (with nacelle) side-to-side bending, fore...
"TwrBsFxt , TwrBsFyt , TwrBsFzt" - Fore-aft shear, side-to-side shear, and vertical f...
"TwrBsMxt , TwrBsMyt , TwrBsMzt" - Side-to-side bending, fore-aft bending, and yaw mo...
END of FAST input file (the word "END" must appear in the first 3 columns of this last line).
-----

```

Listing 3.3: NRELOffshrBslne5MW_AeroDyn.ipt

```

NREL 5.0 MW offshore baseline aerodynamic input properties; Compatible with AeroDyn v12.58.
SI          SysUnits   - System of units for used for input and output [must be SI for FAST...
BEDDOES    StallMod   - Dynamic stall included [BEDDOES or STEADY] (unquoted string)
USE_CM     UseCm       - Use aerodynamic pitching moment model? [USE_CM or NO_CM] (unquoted...
EQUIL      InfModel   - Inflow model [DYNIN or EQUIL] (unquoted string)
SWIRL      IndModel   - Induction-factor model [NONE or WAKE or SWIRL] (unquoted string)
          0.005      AToler   - Induction-factor tolerance (convergence criteria) (-)
PRANDtl    TLModel   - Tip-loss model (EQUIL only) [PRANDtl, GTECH, or NONE] (unquoted st...
PRANDtl    HLModel   - Hub-loss model (EQUIL only) [PRANDtl or NONE] (unquoted string)
"PARAM_WND_FILE"      WindFile   - Name of file containing wind data...
          90.0      HH         - Wind reference (hub) height [TowerHt+Twr2Shft+OverHang*SIN(ShftTil...
          0.0      TwrShad   - Tower-shadow velocity deficit (-)
9999.9     ShadHWid   - Tower-shadow half width (m)
9999.9     T_Shad_Refpt - Tower-shadow reference point (m)
          1.225     AirDens   - Air density (kg/m^3)
          1.464E-5  KinVisc   - Kinematic air viscosity [CURRENTLY IGNORED] (m^2/sec)
          0.0125    DTAero    - Time interval for aerodynamic calculations (sec)
          8         NumFoil   - Number of airfoil files (-)
"../AeroData/NREL5M/Cylinder1.dat"      FoilNm
- Names of the airfoi...
"../AeroData/NREL5M/Cylinder2.dat"
"../AeroData/NREL5M/DU40_A17.dat"
"../AeroData/NREL5M/DU35_A17.dat"
"../AeroData/NREL5M/DU30_A17.dat"
"../AeroData/NREL5M/DU25_A17.dat"
"../AeroData/NREL5M/DU21_A17.dat"
"../AeroData/NREL5M/NACA64_A17.dat"
          62         BldNodes - Number of blade nodes used for analysis (-)
RNodes   AeroTwst DRNodes Chord  Nfoil PrnElm
2.000000 13.308000 1.000000 3.542000 1 NOPRINT
3.000000 13.308000 1.000000 3.557216 1 NOPRINT
4.000000 13.308000 1.000000 3.671364 1 NOPRINT
5.000000 13.308000 1.000000 3.785511 1 NOPRINT
6.000000 13.308000 1.000000 3.899805 1 NOPRINT
7.000000 13.308000 1.000000 4.014319 1 NOPRINT
8.000000 13.308000 1.000000 4.128833 1 NOPRINT
9.000000 13.308000 1.000000 4.243101 2 NOPRINT
10.000000 13.308000 1.000000 4.357246 2 NOPRINT
11.000000 13.308000 1.000000 4.471391 2 NOPRINT
12.000000 13.196537 1.000000 4.562793 3 NOPRINT
13.000000 12.750683 1.000000 4.585963 3 NOPRINT
14.000000 12.304829 1.000000 4.609134 3 NOPRINT
15.000000 11.858976 1.000000 4.632305 3 NOPRINT
16.000000 11.431780 1.000000 4.644902 4 NOPRINT
17.000000 11.110317 1.000000 4.597585 4 NOPRINT
18.000000 10.788854 1.000000 4.550268 4 NOPRINT
19.000000 10.467390 1.000000 4.502951 4 NOPRINT
20.000000 10.147963 1.000000 4.455451 4 NOPRINT
21.000000 9.867232 1.000000 4.404476 4 NOPRINT
22.000000 9.586500 1.000000 4.353500 4 NOPRINT
23.000000 9.305768 1.000000 4.302524 4 NOPRINT
24.000000 9.025037 1.000000 4.251549 4 NOPRINT
25.000000 8.729244 1.000000 4.192927 5 NOPRINT
26.000000 8.432659 1.000000 4.133902 5 NOPRINT
27.000000 8.136073 1.000000 4.074878 5 NOPRINT
28.000000 7.839488 1.000000 4.015854 5 NOPRINT
29.000000 7.535646 1.000000 3.953305 6 NOPRINT
30.000000 7.230524 1.000000 3.890134 6 NOPRINT
31.000000 6.925402 1.000000 3.826963 6 NOPRINT
32.000000 6.620280 1.000000 3.763793 6 NOPRINT
33.000000 6.327598 1.000000 3.703000 6 NOPRINT
34.000000 6.039061 1.000000 3.643000 6 NOPRINT
35.000000 5.750524 1.000000 3.583000 6 NOPRINT

```

```
36.000000 5.461988 1.000000 3.523000 6 NOPRINT
37.000000 5.175037 1.000000 3.463000 7 NOPRINT
38.000000 4.888939 1.000000 3.403000 7 NOPRINT
39.000000 4.602841 1.000000 3.343000 7 NOPRINT
40.000000 4.316744 1.000000 3.283000 7 NOPRINT
41.000000 4.045402 1.000000 3.223000 7 NOPRINT
42.000000 3.786134 1.000000 3.163000 7 NOPRINT
43.000000 3.526866 1.000000 3.103000 7 NOPRINT
44.000000 3.267598 1.000000 3.043000 7 NOPRINT
45.000000 3.036537 1.000000 2.983000 8 NOPRINT
46.000000 2.839951 1.000000 2.923000 8 NOPRINT
47.000000 2.643366 1.000000 2.863000 8 NOPRINT
48.000000 2.446780 1.000000 2.803000 8 NOPRINT
49.000000 2.251305 1.000000 2.743000 8 NOPRINT
50.000000 2.057890 1.000000 2.683000 8 NOPRINT
51.000000 1.864476 1.000000 2.623000 8 NOPRINT
52.000000 1.671061 1.000000 2.563000 8 NOPRINT
53.000000 1.477488 1.000000 2.503000 8 NOPRINT
54.000000 1.283441 1.000000 2.443001 8 NOPRINT
55.000000 1.089395 1.000000 2.383001 8 NOPRINT
56.000000 0.895348 1.000000 2.323002 8 NOPRINT
57.000000 0.712699 1.000000 2.243795 8 NOPRINT
58.000000 0.532331 1.000000 2.160745 8 NOPRINT
59.000000 0.360341 1.000000 2.061597 8 NOPRINT
60.000000 0.263755 1.000000 1.817570 8 NOPRINT
61.000000 0.167168 1.000000 1.573543 8 NOPRINT
62.000000 0.077559 1.000000 1.038267 8 NOPRINT
62.750000 0.019390 0.500000 0.259567 8 NOPRINT
```

3.B Appendix B - Normalised load maps (normal operation)

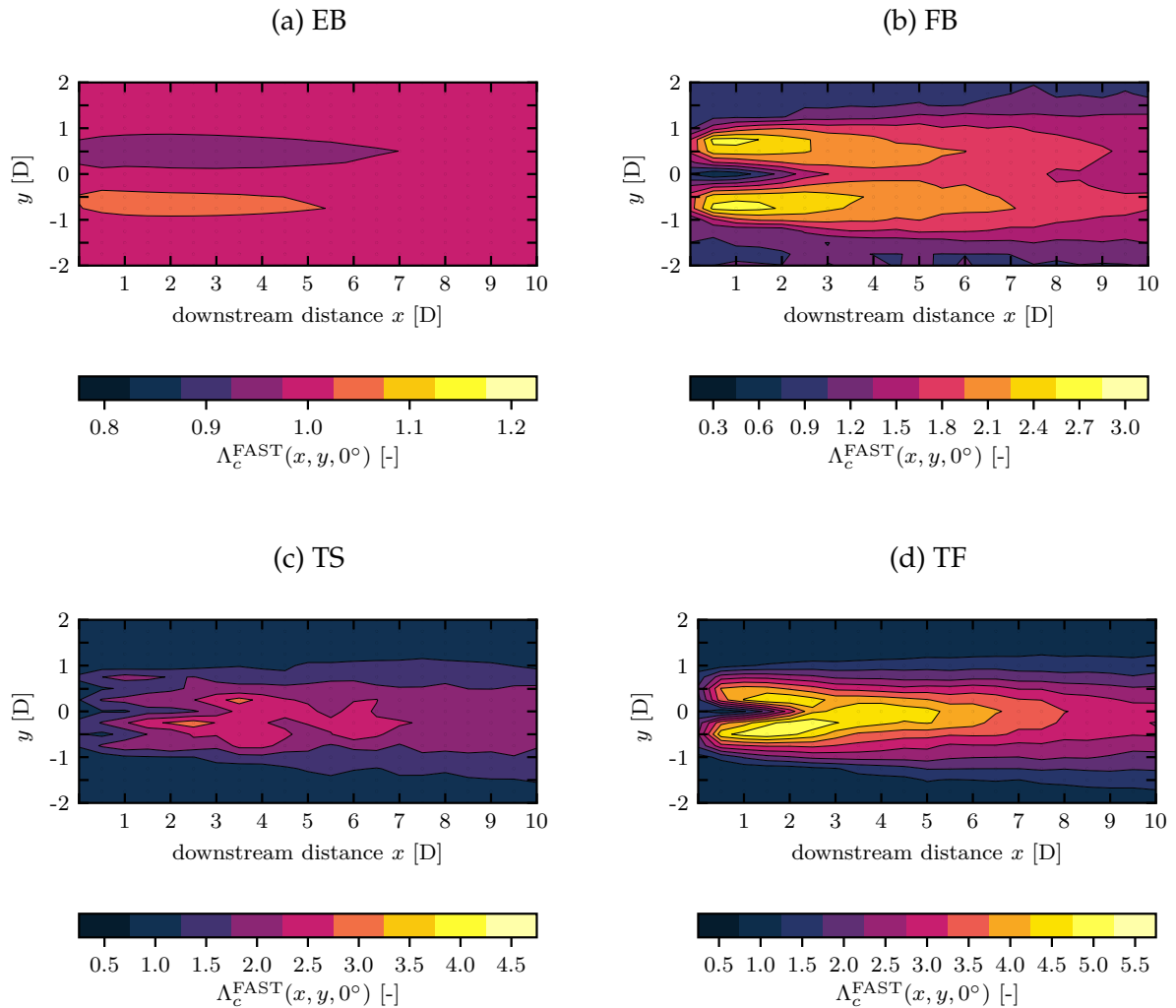


Figure 3.25: Normalised load maps $\Lambda_c^{\text{FAST}}(x, y, 0^\circ)$ for the reference wind field *N06* and the load sensors (a) edgewise blade root bending moment, (b) flapwise blade root bending moment, (c) tower base side-to-side moment and (d) tower base fore-aft moment.

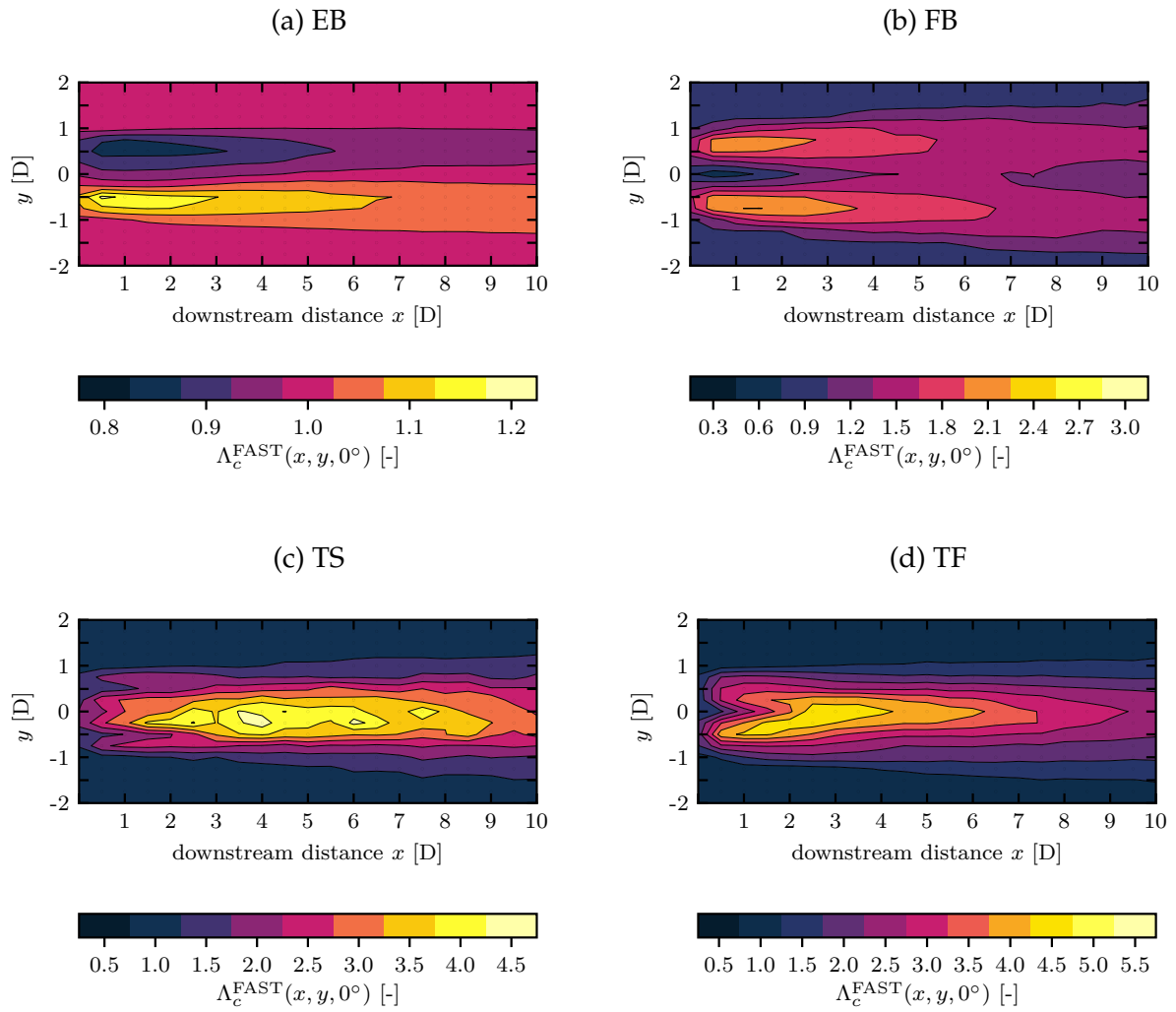


Figure 3.26: Normalised load maps $\Lambda_c^{\text{FAST}}(x, y, 0^\circ)$ for the reference wind field *N10* and the load sensors (a) edgewise blade root bending moment, (b) flapwise blade root bending moment, (c) tower base side-to-side moment and (d) tower base fore-aft moment.

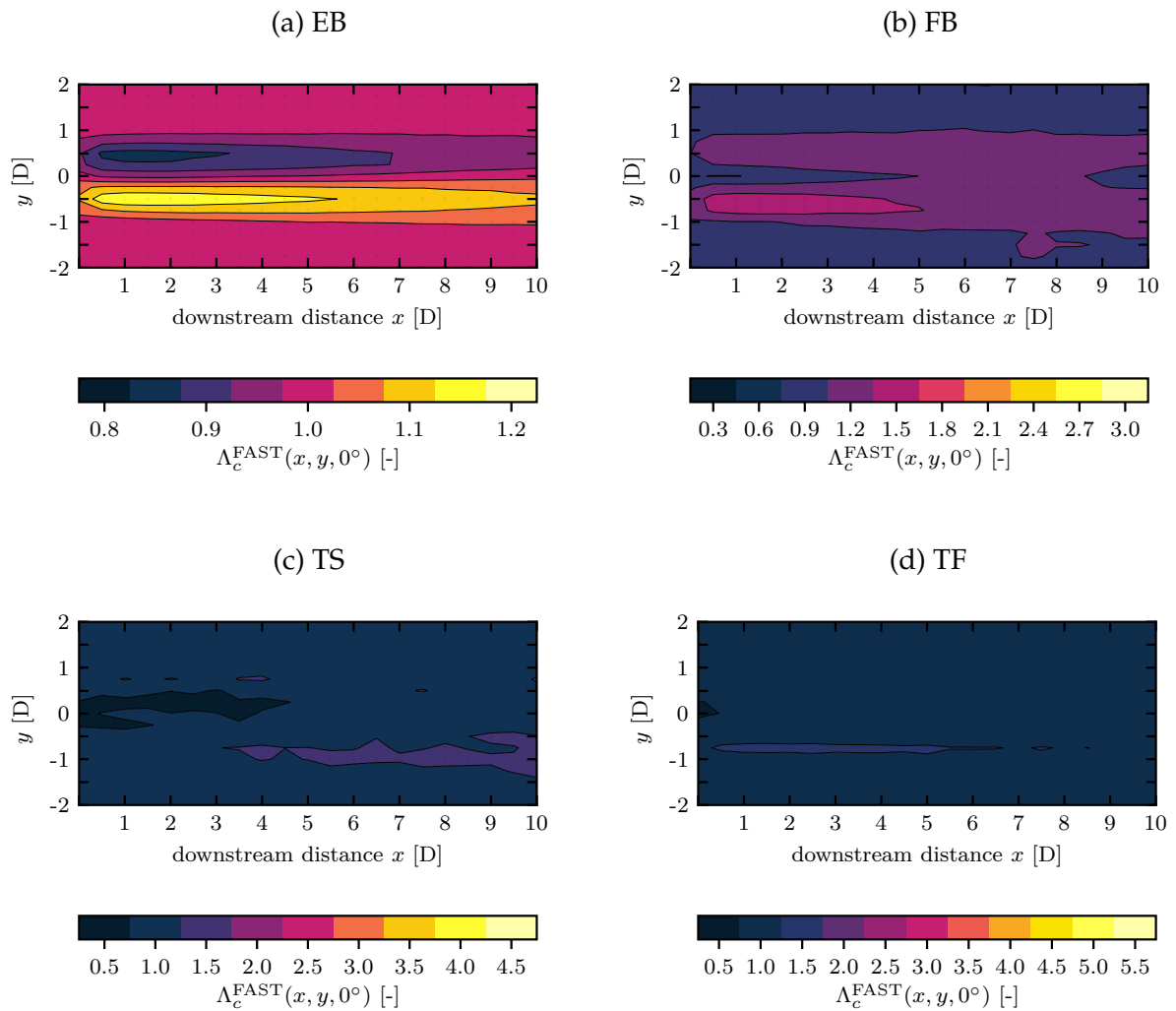


Figure 3.27: Normalised load maps $\Lambda_c^{\text{FAST}}(x, y, 0^\circ)$ for the reference wind field *N12* and the load sensors (a) edgewise blade root bending moment, (b) flapwise blade root bending moment, (c) tower base side-to-side moment and (d) tower base fore-aft moment.

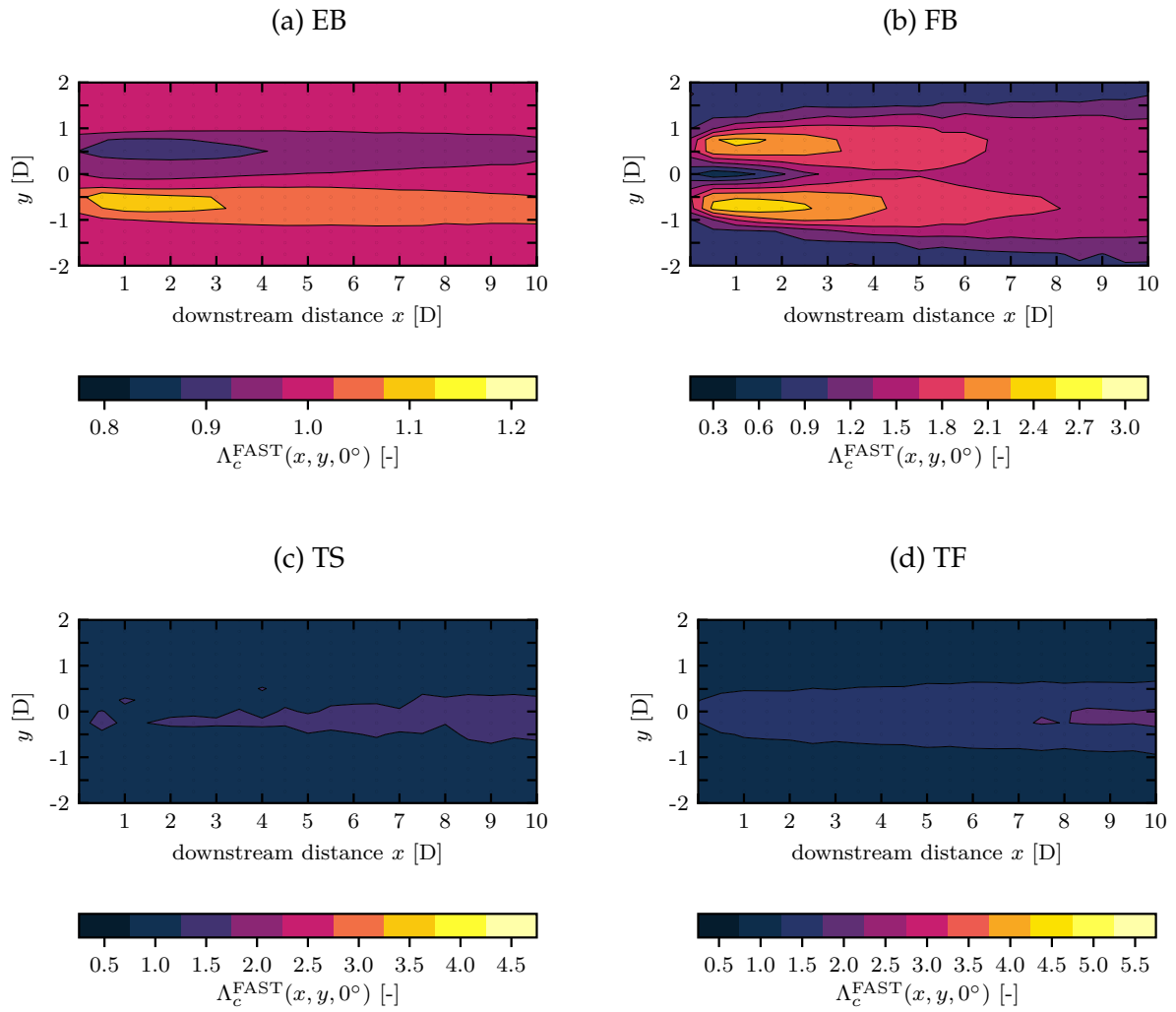


Figure 3.28: Normalised load maps $\Lambda_c^{\text{FAST}}(x, y, 0^\circ)$ for the reference wind field *N14* and the load sensors (a) edgewise blade root bending moment, (b) flapwise blade root bending moment, (c) tower base side-to-side moment and (d) tower base fore-aft moment.

3.C Appendix C - Normalised load maps (yaw misalignment)

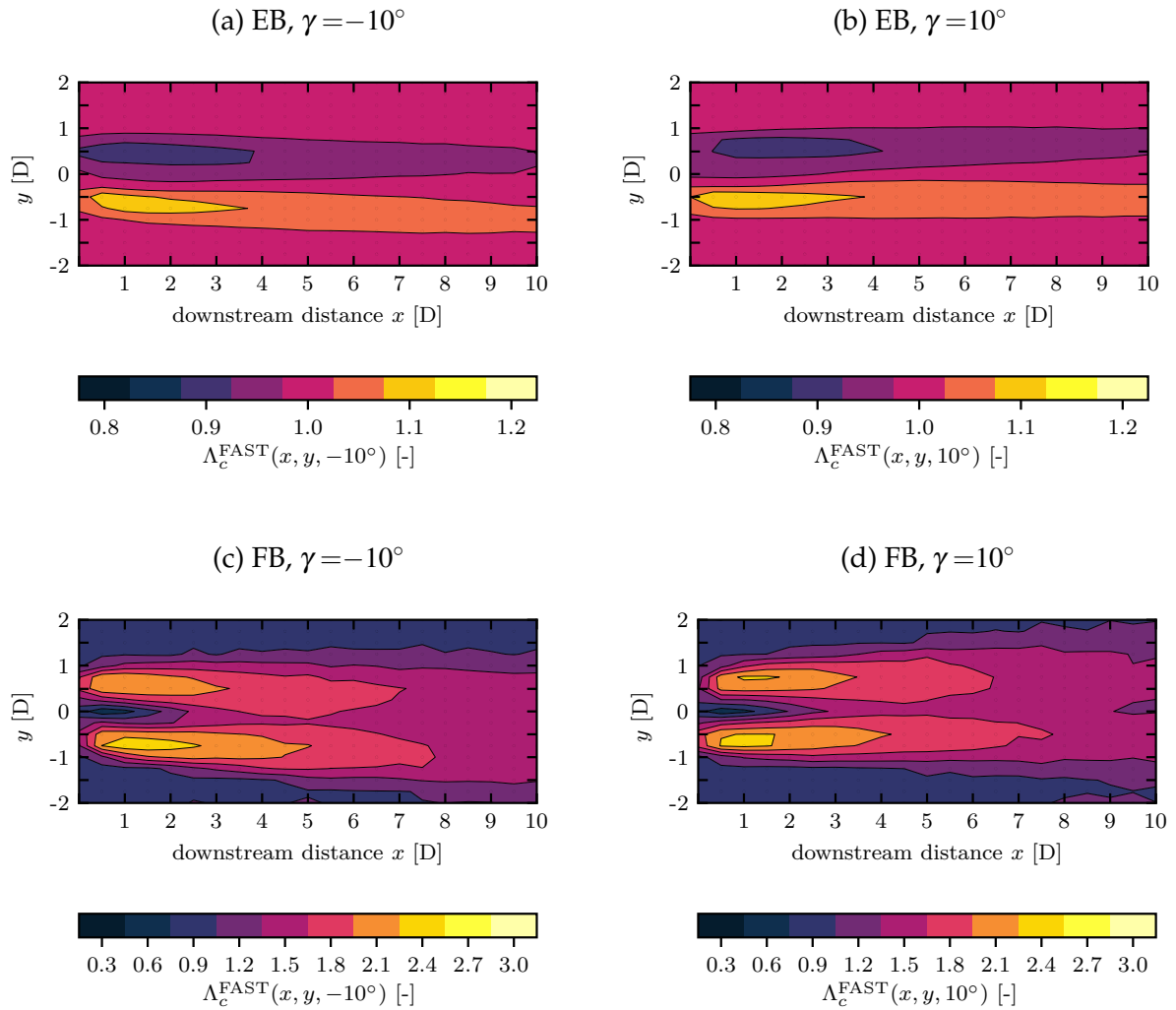


Figure 3.29: Normalised load maps $\Lambda_c^{\text{FAST}}(x, y, \gamma)$ for the reference wind field *N08* with yaw misalignments γ of the upstream turbine of -10° and 10° and the load sensors for the edgewise and flapwise blade root bending moments.

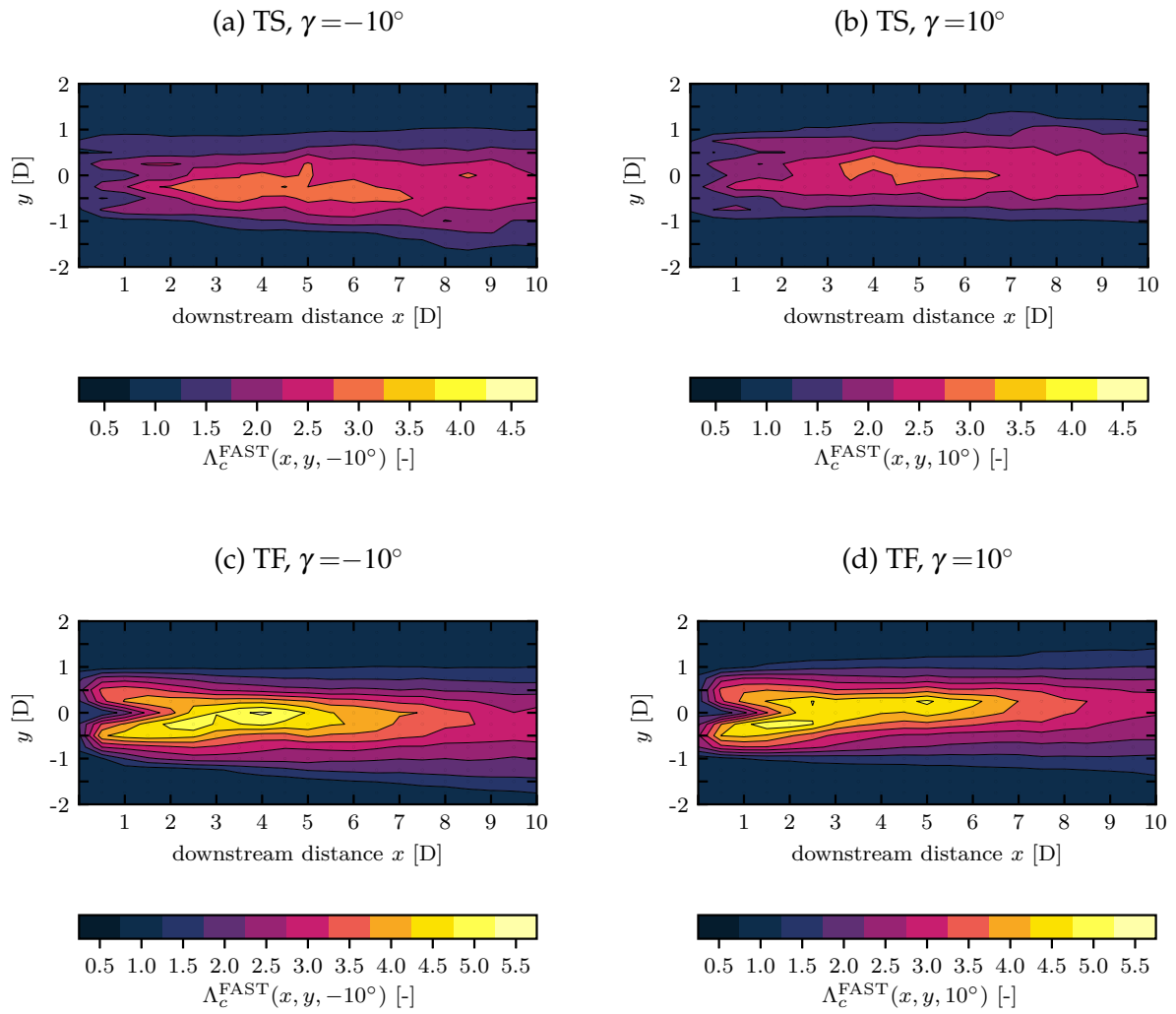


Figure 3.30: Normalised load maps $\Lambda_c^{\text{FAST}}(x, y, \gamma)$ for the reference wind field *N08* with yaw misalignments γ of the upstream turbine of -10° and 10° and the load sensors for the tower base side-to-side moment and tower base fore-aft moment.

Chapter 4

Numerical investigation of wind turbine wake development in directionally sheared inflow

The content of this chapter is identical to the journal article *Bromm et al. (2017c)*: Bromm, M., Vollmer, L. and Kühn, M. (2017c). 'Numerical investigation of wind turbine wake development in directionally sheared inflow.' In: *Wind Energy* 20, pp. 381–395. DOI: 10.1002/we.2010 Copyright ©2016 John Wiley & Sons, Ltd. (used with permission).

Abstract

Turbines in wind farms are subject to complex mutual aerodynamic interactions, which in detail depend upon the characteristics of the atmospheric boundary layer. Our two objectives with this paper were to investigate the impact of directionally sheared inflow on the wake development behind a single wind turbine and to analyse the impact of the wakes on the energy yield and loading of a downstream turbine, which is exposed to partial and full wake conditions. We performed simulations with a framework based on a coupled approach of large-eddy simulation and an actuator line representation of an aeroelastic turbine model. Our results show that directionally sheared inflow leads to a non-symmetrical wake development, which transfers to distinct differences in the energy yield and loading of downstream turbines of equal lateral offsets in opposite direction. Therefore, the assumption of wakes being axisymmetrical could lead to notable deviations in the prediction of wake behaviour and their impact on downstream turbines for atmospheric inflow conditions, which include directional shear.

Keywords

ACL, atmospheric inflow, Coriolis, LES, shear, wind veer

Content not included due to copyright restrictions. Please refer to the original article in *Wind Energy*.

Bromm et al. (2017c): Bromm, M., Vollmer, L. and Kühn, M. (2017c). 'Numerical investigation of wind turbine wake development in directionally sheared inflow.' In: *Wind Energy* 20, pp. 381–395. DOI: 10.1002/we.2010.

Content not included due to copyright restrictions. Please refer to the original article in *Wind Energy*.

Bromm et al. (2017c): Bromm, M., Vollmer, L. and Kühn, M. (2017c). 'Numerical investigation of wind turbine wake development in directionally sheared inflow.' In: *Wind Energy* 20, pp. 381–395. DOI: 10.1002/we.2010.

Content not included due to copyright restrictions. Please refer to the original article in *Wind Energy*.

Bromm et al. (2017c): Bromm, M., Vollmer, L. and Kühn, M. (2017c). 'Numerical investigation of wind turbine wake development in directionally sheared inflow.' In: *Wind Energy* 20, pp. 381–395. DOI: 10.1002/we.2010.

Content not included due to copyright restrictions. Please refer to the original article in *Wind Energy*.

Bromm et al. (2017c): Bromm, M., Vollmer, L. and Kühn, M. (2017c). 'Numerical investigation of wind turbine wake development in directionally sheared inflow.' In: *Wind Energy* 20, pp. 381–395. DOI: 10.1002/we.2010.

Content not included due to copyright restrictions. Please refer to the original article in *Wind Energy*.

Bromm et al. (2017c): Bromm, M., Vollmer, L. and Kühn, M. (2017c). 'Numerical investigation of wind turbine wake development in directionally sheared inflow.' In: *Wind Energy* 20, pp. 381–395. DOI: 10.1002/we.2010.

Content not included due to copyright restrictions. Please refer to the original article in *Wind Energy*.

Bromm et al. (2017c): Bromm, M., Vollmer, L. and Kühn, M. (2017c). 'Numerical investigation of wind turbine wake development in directionally sheared inflow.' In: *Wind Energy* 20, pp. 381–395. DOI: 10.1002/we.2010.

Content not included due to copyright restrictions. Please refer to the original article in *Wind Energy*.

Bromm et al. (2017c): Bromm, M., Vollmer, L. and Kühn, M. (2017c). 'Numerical investigation of wind turbine wake development in directionally sheared inflow.' In: *Wind Energy* 20, pp. 381–395. DOI: 10.1002/we.2010.

Content not included due to copyright restrictions. Please refer to the original article in *Wind Energy*.

Bromm et al. (2017c): Bromm, M., Vollmer, L. and Kühn, M. (2017c). 'Numerical investigation of wind turbine wake development in directionally sheared inflow.' In: *Wind Energy* 20, pp. 381–395. DOI: 10.1002/we.2010.

Content not included due to copyright restrictions. Please refer to the original article in *Wind Energy*.

Bromm et al. (2017c): Bromm, M., Vollmer, L. and Kühn, M. (2017c). 'Numerical investigation of wind turbine wake development in directionally sheared inflow.' In: *Wind Energy* 20, pp. 381–395. DOI: 10.1002/we.2010.

Content not included due to copyright restrictions. Please refer to the original article in *Wind Energy*.

Bromm et al. (2017c): Bromm, M., Vollmer, L. and Kühn, M. (2017c). 'Numerical investigation of wind turbine wake development in directionally sheared inflow.' In: *Wind Energy* 20, pp. 381–395. DOI: 10.1002/we.2010.

Content not included due to copyright restrictions. Please refer to the original article in *Wind Energy*.

Bromm et al. (2017c): Bromm, M., Vollmer, L. and Kühn, M. (2017c). 'Numerical investigation of wind turbine wake development in directionally sheared inflow.' In: *Wind Energy* 20, pp. 381–395. DOI: 10.1002/we.2010.

Content not included due to copyright restrictions. Please refer to the original article in *Wind Energy*.

Bromm et al. (2017c): Bromm, M., Vollmer, L. and Kühn, M. (2017c). 'Numerical investigation of wind turbine wake development in directionally sheared inflow.' In: *Wind Energy* 20, pp. 381–395. DOI: 10.1002/we.2010.

Content not included due to copyright restrictions. Please refer to the original article in *Wind Energy*.

Bromm et al. (2017c): Bromm, M., Vollmer, L. and Kühn, M. (2017c). 'Numerical investigation of wind turbine wake development in directionally sheared inflow.' In: *Wind Energy* 20, pp. 381–395. DOI: 10.1002/we.2010.

Content not included due to copyright restrictions. Please refer to the original article in *Wind Energy*.

Bromm et al. (2017c): Bromm, M., Vollmer, L. and Kühn, M. (2017c). 'Numerical investigation of wind turbine wake development in directionally sheared inflow.' In: *Wind Energy* 20, pp. 381–395. DOI: 10.1002/we.2010.

Content not included due to copyright restrictions. Please refer to the original article in *Wind Energy*.

Bromm et al. (2017c): Bromm, M., Vollmer, L. and Kühn, M. (2017c). 'Numerical investigation of wind turbine wake development in directionally sheared inflow.' In: *Wind Energy* 20, pp. 381–395. DOI: 10.1002/we.2010.

Content not included due to copyright restrictions. Please refer to the original article in *Wind Energy*.

Bromm et al. (2017c): Bromm, M., Vollmer, L. and Kühn, M. (2017c). 'Numerical investigation of wind turbine wake development in directionally sheared inflow.' In: *Wind Energy* 20, pp. 381–395. DOI: 10.1002/we.2010.

Content not included due to copyright restrictions. Please refer to the original article in *Wind Energy*.

Bromm et al. (2017c): Bromm, M., Vollmer, L. and Kühn, M. (2017c). 'Numerical investigation of wind turbine wake development in directionally sheared inflow.' In: *Wind Energy* 20, pp. 381–395. DOI: 10.1002/we.2010.

Content not included due to copyright restrictions. Please refer to the original article in *Wind Energy*.

Bromm et al. (2017c): Bromm, M., Vollmer, L. and Kühn, M. (2017c). 'Numerical investigation of wind turbine wake development in directionally sheared inflow.' In: *Wind Energy* 20, pp. 381–395. DOI: 10.1002/we.2010.

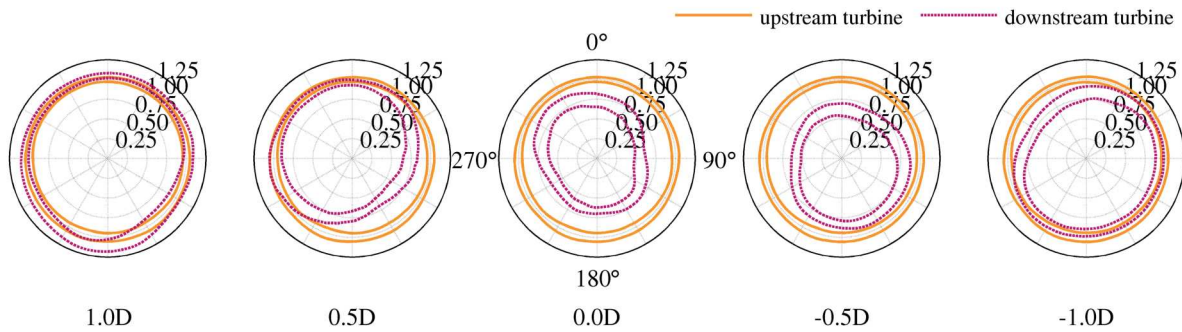


Figure 4.16: Sigma interval ($\mu \pm \sigma$) of the 600 s averaged flapwise moment at the blade root shown for the upstream and downstream turbine in turbulent S-H inflow conditions for different lateral offsets and a downstream distance of 6D. The moments were determined for 5° azimuth intervals and normalized with the mean value of the upstream turbine in this interval. An angle of 0° corresponds to a straight upward blade orientation.

4.4 Conclusion

A framework consisting of the large-eddy code PALM and the aeroelastic code FAST was used for investigating the wake development in directionally sheared inflow conditions and the impact of the wake on the power generation and loading of a downstream turbine.

It was shown that the directional shear of the inflow, which is attributed to the force balance between friction, pressure gradient and Coriolis force, results in a strong non-symmetrical skewed wake development with an ellipse-like cross section. As the turbines in the simulations were positioned at a latitude of 54° north, a clockwise rotation of the inflow direction with height was obtained, resulting in a rotation of the ellipse-like wake cross section towards the right-hand side. In the same direction, a more far-reaching expansion of the deficit was observed, whereas the expansion towards the left was rather limited with the focus being close to the ground. An investigation of the propagation of the deficit at different heights confirmed the relationship of inflow direction and wake propagation.

Because the wake development in directionally sheared inflow is non-symmetrical, a corresponding behaviour was also found with respect to power and loading of downstream turbines for equal lateral offsets in opposite directions. Downstream turbines, which are positioned towards the left, when viewed from upstream, experience a significant higher power output compared with turbines on the right-hand side with a lateral offset of equal magnitude. However, the rotor of turbines located on the left-

hand side is subject to stronger load imbalances during each revolution as it is exposed to unfavourable partial wake conditions with high-velocity gradients.

Furthermore, a slight increase in the generated power of the downstream turbines compared with the upstream turbines was observed for positive offsets in the range of one to one and a half rotor diameters. This effect might be limited to smaller tower heights as it is based on an interaction of wake flow and ground.

Despite the shown significance of directional shear on the wake development of wind turbines, its impact has been investigated only very limited in the past, especially with the focus being on turbine interaction.

We conclude that the assumption of wakes being axisymmetrical could lead to notable deviations in the prediction of wake behaviour and their impact on downstream turbines for atmospheric inflow conditions, which include directional shear. In addition, other fields of wind energy research as, for example, the implementation of turbine and wind farm control strategies as well as the optimisation of wind farm layouts could be affected by the presented findings.

Acknowledgements

This work was partially funded by the German Federal Ministry for Economic Affairs and Energy (BMWi) in the scope of the CompactWind project (FKZ 0325492B). Computer resources have been provided by the North German Supercomputing Alliance (HLRN) and the HPC Cluster FLOW (Facility for Large-Scale Computations in Wind Energy Research), located at the University of Oldenburg (Germany), and funded by the Federal Ministry for the Environment, Nature Conservation and Nuclear Safety (BMU) under grant number 0325220. Furthermore, we thank our colleague Gerald Steinfeld for his scientific feedback and his valuable comments during the preparation of the manuscript.

Chapter 5

Conclusions and Outlook

5.1 Conclusions

Wake deflection through yaw misalignment is one method of wind farm control that has proven its potential in wind tunnel tests and simulations. It is based on introducing an offset between inflow direction and wind turbine orientation to alter the trajectory of its wake for more favourable inflow conditions at downstream turbines and an improved overall wind farm performance. The goal of this thesis was to further improve the understanding of this technique and to identify requirements for successfully putting it into practice.

The main focus of the work was to demonstrate that wakes could be deflected through yaw misalignment at a utility-scale wind turbine in the field. Fortunately, the test was successful and wake displacement was observed at hub height level for yaw misaligned turbine operation and the evaluated neutrally stratified conditions. However, it turned out that even with current state-of-the-art equipment, a complex measurement setup was required and many details had to be considered to obtain reliable results.

In addition to the field testing, simulations were performed to investigate the wake development in directionally sheared inflow and to estimate the power yield and loading of turbines in a wind farm with and without the application of wake deflection. These aspects are important to assess to which extent the application of wake deflection can be beneficial for a wind farm with a certain layout and given inflow conditions. Large-eddy simulations were used for these investigations as they can best represent the atmospheric characteristics of the inflow, which have a strong impact on the wake development.

In the following, the most important results of the research, with respect to the three

research questions that were raised in the introduction, are summarized:

1. A field campaign was conducted to investigate whether wake deflection can be systematically performed at multi-megawatt turbines in the field (Chapter 2):
 - It was demonstrated that the 10-min-averaged wake trajectory of a yaw misaligned wind turbine deviates in neutrally stratified boundary layers from the overall hub height inflow direction. For positive yaw offsets of the turbine, a lateral offset of the wake trajectory toward the downstream left-hand side of the turbine was observed. In the cases of negative yaw offsets, the wake trajectory was shifted toward the downstream right-hand side. Furthermore, larger absolute yaw offsets corresponded to larger lateral wake offsets in the investigated yaw offset range of $\pm 20^\circ$. The wake flows were recorded with a nacelle-based long-range lidar device and the wake trajectories were determined based on the minimum of the power-based rotor equivalent wind speed at each downstream distance. This approach focuses on the impact of the wake flow on downstream wind turbines and is less dependent on the specific wake characteristics than methods that describe a wake by curve fitting or by tracking the maximum deficit. In the case of deflected wakes, this is of particular importance due to their asymmetric cross sections.
 - The investigation and characterization of the wake development of full-scale turbines is challenging due to the complex and dynamically changing ambient conditions and the often limited campaign durations. In order to prove the successful application of wake deflection, the inflow direction and the direction of the wake propagation had to be compared. For this a complex measuring setup with state-of-the-art equipment was necessary, which among other things included GPS devices for determining the nacelle orientation with high accuracy and two lidar devices for the upstream and downstream flow measurements.
 - In the course of the investigations several issues concerning the practical implementation were identified which had to be considered for the experiment. The main reason for this was again the high level of accuracy required. So it turned out, for example, that the accuracy of the standard SCADA output for the yaw alignment did not provide reliable absolute orientations. Furthermore, lidar measurements from the nacelle of a turbine into the wake

can be affected by misalignment of the device itself and by the changing tilt of the nacelle during turbine operation, especially, for measurements with long-range devices at great downstream distances. If a high spatial accuracy is required, this has to be considered and maybe even compensated with suitable mounting or during post processing.

- The additional use of large-eddy simulations as part of the campaign has proven to be very valuable in the evaluation of the measurement data and enabled us to develop a more profound understanding of the complex conditions in the field.
 - Despite the complexity of current field campaigns, at present, almost no recommended practices or suggestions on how to perform such campaigns (e.g. setup of lidar devices, obtaining the yaw orientation of the turbine) and the corresponding post-processing of the measurement data (e.g. wake tracking, filtering of measurement data) do exist. However, different methods and insufficient documentation tend to reduce the comparability of the data and make it difficult to assess its quality. The author is convinced that closer cooperation between researchers and a critical assessment of the current state-of-the-art approach would help to better exploit the full potential of field measurements in the future.
2. A sequential approach of large-eddy simulations and aeroelastic simulations was used to investigate how the power yields and the loads of both the upstream and downstream turbine are affected if wake deflection is used at the upstream turbine (Chapter 3). The following results were obtained for turbines operating in partial load within a neutrally stratified boundary layer:
- Large-eddy simulations are increasingly popular in wind energy research as they enable realistically reproducing the flow in the atmospheric boundary layer. Unfortunately, the spatial resolution of large-eddy simulations is limited, as the grid spacing cannot be reduced arbitrarily due to the increasing computational demand. However, coarser grid spacing leads to a reduced frequency range of the wind fields that affects the obtained loads. We generated stochastic wind fields with similar average statistical characteristics (e.g. mean wind speed, turbulence intensity) as the wind fields that were extracted from the undisturbed inflow of the large-eddy simulations. From these stochastic wind fields, several wind fields with a reduced frequency

range (decimation with low-pass filtering) were derived and used in simulations. For the given conditions, the tower sensors were more sensitive to a reduction of the frequency range in comparison to the blade sensors.

- A comparison of the loads obtained with the stochastic baseline wind fields and the ones of the large-eddy wind fields showed a good agreement despite the different properties of the wind fields in terms of frequency resolution and representation of the physical characteristics.
- Despite a long initialization phase, inhomogeneities were identified in the large-eddy wind fields. The power yields of wind turbines at different location within the wind fields therefore differ. Deviations in the power yield of up to 8 % from the mean power yield of several positions within the domain of a simulation were observed. This variability must be taken into account when comparing results and drawing conclusions from only a small number of simulations.
- Various test scenarios were developed to assess how the overall wind farm power yield and the individual turbine loading is affected by the application of wake deflection. In each case, the goal was to maximize the combined power yield of the wind turbines involved. The considered yaw angles were 0° , $\pm 10^\circ$ and $\pm 20^\circ$ to limit the number of simulations and to assess situations that could also be implemented in the field with current equipment. Considering all inflow directions equally, 1.23 % and 0.90 % more power is yielded for the two test wind farms in relation to the the combined power of the wind turbines in the wind farms and undisturbed inflow. For individual inflow directions, power yield gains of approximately 4.7 % were achieved. If only inflow directions were considered for which wake deflection was used at least at one of the turbines, overall gains of 1.98 % and 1.44 % were obtained.

All results serve as indicators only, as they depend especially on the wind farm layout and the chosen inflow wind speeds and directions.

- The particular implementation of the reference wind turbine and the inflow conditions chosen for the investigation, unfortunately, led to an excitation of the natural frequency of the tower by the 2P frequency of the rotor. This is a reason for the very high resulting tower loads. In further investigations, a different operating point should be chosen in order to be able to draw more comprehensive conclusions about the tower loads.

Concerning the loading in general, no uniform picture emerged. On the one hand, the loads on the waked wind turbine decreased when the upstream turbine applied wake deflection. On the other hand, the loads on the yaw misaligned turbine increased in parallel in almost all cases. Depending on the magnitude of both changes, an overall increase (e.g. tower base side-to-side DELs) or decrease (e.g. tower base fore-aft DELs) was observed. For the blade loads, virtually no change was observed. Due to the different characteristics of the load sensors, an optimised wind farm operation with regard to the total loads of all sensors does therefore not seem feasible according to our current state of knowledge.

3. A framework that consists of the aeroelastic code *FAST* and the large-eddy code *PALM* was developed and used to determine how directionally sheared inflow influences the wake development of a wind turbine (Chapter 4). Furthermore, the impact on the energy yield and the loading of a downstream turbine was assessed for different lateral positions. Directional shear usually occurs most strongly in stably stratified conditions. According to the current state of research, under these conditions, the use of the wake deflection is also most promising due to strong, persistent wakes and a low directional variability of the inflow (Rott et al. (2018) and Vollmer et al. (2016)):

- Directionally sheared inflow does result in a strong non-symmetrical skewed wake development with an ellipse-like cross section.
- Because of this non-symmetrical wake development, a corresponding asymmetry is also found with respect to the power yield and the structural loading of two waked wind turbines that are located at the same downstream distance but that have lateral offsets of equal magnitude in opposite directions.
- For the sake of simplicity, wakes have been considered rotationally symmetrical in almost all engineering wake models so far. However, for certain ambient conditions, it may be necessary to consider a potential wake asymmetry in order to achieve meaningful results.

5.2 Suggestions for future research

Over the past few years, wind farm control has become an increasingly important topic in wind energy research and has drawn a significant interest among manufacturers and

wind farm operators. Due to technical developments and new research results, a more detailed understanding of the complex mutual influences of turbines in wind farms was gained. By optimising the operation of the wind farm as a whole, one attempts to minimise the negative effects of the interactions between turbines and to positively influence power yield and lower structural loading.

Through the author's research on wake deflection by means of simulations and campaigns in the field, it was possible to obtain a comprehensive understanding of current challenges in research and development. Despite all the achievements, there are still a number of challenges to overcome.

At the end of this work, the author would like to stress the importance of extensive field campaigns for validation and demonstration purposes. Overall, newly developed wind farm control concepts need to prove their value in real applications in utility-scale wind farms. Despite the indisputable possibilities of simulations, even with the currently most sophisticated ones, certain characteristics cannot be adequately represented with reasonable effort and simplified assumptions have to be made. On the other hand, in simulations there are extensive possibilities to determine data with the desired spatial and temporal resolution. However, in the field, the possibilities are limited and measurements are subject to inherent uncertainties. Even supposedly basic measurements, like determining the atmospheric stability at a site, still can be challenging tasks. Thus field experiments are essential to evaluate the transferability of the results and finally, to assess the economic viability.

Due to new technical developments, such as scanning lidar devices, there was a certain euphoria, which led to more and more complex campaigns. However, the first scientific results were sometimes dissatisfying with regard to the effort involved. From the author's point of view, it was important to take a step back and establish a solid foundation and to repeat measurements on such a base. It was required to put the focus even more on high-quality measurement campaigns that are comprehensively documented in order to make the data accessible to others and allow a critical analysis of the methods used. Furthermore, in the author's experience it is necessary to concentrate on long-term campaigns in order to obtain a comprehensive database for different ambient conditions and operating conditions with an identical measurement setup. In this way, the existing gap between research and industrial application could be reduced which is important for the further deployment of wind energy and for increasing its contribution to the global electricity generation.

References

- Abkar, M. and Porté-Agel, F. (2015). 'Influence of atmospheric stability on wind-turbine wakes: A large-eddy simulation study'. In: *Physics of Fluids* 27(3), p. 035104. DOI: 10.1063/1.4913695.
- Abkar, M. and Porté-Agel, F. (2016). 'Influence of the Coriolis force on the structure and evolution of wind turbine wakes.' In: *PhysRev Fluids* 1, pp. 1–14. DOI: 10.1103/PhysRevFluids.1.063701.
- Abkar, M., Sharifi, A. and Porté-Agel, F. (2016). 'Wake flow in a wind farm during a diurnal cycle.' In: *J Turbul* 17(4), pp. 420–441. DOI: 10.1080/14685248.2015.1127379.
- Abkar, M., Sørensen, J. N. and Porté-Agel, F. (2018). 'An Analytical Model for the Effect of Vertical Wind Veer on Wind Turbine Wakes'. In: *Energies* 11(7). DOI: 10.3390/en11071838.
- Adaramola, M. and Krogstad, P.-R. (2011). 'Experimental investigation of wake effects on wind turbine performance.' In: *Renew Energy* 36, pp. 2078–2086. DOI: 10.1016/j.renene.2011.01.024.
- Ahrens, R., Bockholt, S., Bottasso, C. L., Bromm, M., Campagnolo, F., Heinemann, D., Voß, S. and Kühn, M. (2016). *Erhöhung des Flächenenergieertrags in Windparks durch avancierte Anlagen- und Parkregelung (CompactWind)*. Abschlussbericht des Verbund-Forschungsprojekts. Renningen: Robert Bosch GmbH, Zentralbereich Forschung und Voraentwicklung (CR/AEI). DOI: 10.2314/gbv:894297163.
- Aitken, M. L. and Lundquist, J. K. (2014). 'Utility-scale wind turbine wake characterization using nacelle-based long-range scanning lidar.' In: *J Atmos Oceanic Tech* 31(7), pp. 1529–1539. DOI: 10.1175/JTECH-D-13-00218.1.
- Allaerts, D. and Meyers, J. (2015). 'Large eddy simulation of a large wind-turbine array in a conventionally neutral atmospheric boundary layer'. In: *Physics of Fluids* 27(6), p. 065108. DOI: 10.1063/1.4922339.
- Angelou, N., Mikkelsen, T., Hansen, K. H., Sjöholm, M. and Harris, M. (2010). *LIDAR wind speed measurements from a rotating spinner (SpinnerEx 2009)*. Tech. rep. Risø-

- R-1741(EN). Roskilde, Denmark: Risø DTU - National Laboratory for Sustainable Energy.
- Annoni, J., Gebraad, P. M. O., Scholbrock, A. K., Fleming, P. A. and van Wingerden, J. W. (2016). 'Analysis of axial-induction-based wind plant control using an engineering and a high-order wind plant model'. In: *Wind Energy* 19(6), pp. 1135–1150. DOI: 10.1002/we.1891.
- Arya, P. S. and Holton, J. R. (2001). *Introduction to Micrometeorology*. International Geophysics. Elsevier Science. ISBN: 9780120593545.
- ASTM E 1049-85 (2011). *Standard Practices for Cycle Counting in Fatigue Analysis*. Tech. rep. ASTM. DOI: 10.1520/E1049-85R17.
- Bartl, J. and Sætran, L. (2017). 'Blind test comparison of the performance and wake flow between two in-line wind turbines exposed to different turbulent inflow conditions'. In: *Wind Energy Science* 2(1), pp. 55–76. DOI: 10.5194/wes-2-55-2017.
- Bartl, J., Mühle, F. and Sætran, L. (2018). 'Wind tunnel study on power output and yaw moments for two yaw-controlled model wind turbines'. In: *Wind Energy Science* 3(2), pp. 489–502. DOI: 10.5194/wes-3-489-2018.
- Bastankhah, M. and Porté-Agel, F. (2016). 'Experimental and theoretical study of wind turbine wakes in yawed conditions.' In: *J Fluid Mech* 806, pp. 506–541. DOI: 10.1017/jfm.2016.595.
- Bastine, D. (2017). 'Stochastic Analysis and Modeling of Wind Turbine Wakes'. PhD thesis. ForWind - University of Oldenburg.
- Beare, R. J. and Macvean, M. K. (2004). 'Resolution sensitivity and scaling of large-eddy simulations of the stable boundary layer'. In: *Boundary-Layer Meteorology* 112(2), pp. 257–281.
- Beck, H. and Kühn, M. (2017). 'Dynamic data filtering of long-range Doppler LiDAR wind speed measurements.' In: *Remote Sens.* 9(6), p. 561. DOI: 10.3390/rs9060561.
- Berg, J., Bryant, J., LeBlanc, B., Maniaci, D. C., Naughton, B., Paquette, J. A., Resor, B. R., White, J. and Kroeker, D. (2014). 'Scaled Wind Farm Technology Facility Overview'. In: *32nd ASME Wind Energy Symposium*. DOI: 10.2514/6.2014-1088.
- Bhaganagar, K. and Debnath, M. (2014). 'Implications of Stably Stratified Atmospheric Boundary Layer Turbulence on the Near-Wake Structure of Wind Turbines'. In: *Energies* 7(9), pp. 5740–5763. DOI: 10.3390/en7095740.
- Bingöl, F., Trujillo, J. J., Mann, J. and Larsen, G. C. (2008). 'Fast wake measurements with LiDAR at Risø test field'. In: *IOP Conference Series: Earth and Environmental Science* 1(1), p. 012022.

- Bodini, N., Zardi, D. and Lundquist, J. K. (2017). 'Three-dimensional structure of wind turbine wakes as measured by scanning lidar.' In: *Atmos Meas Tech* 10(8), pp. 2881–2896. DOI: 10.5194/amt-10-2881-2017.
- Boersma, S., Doekemeijer, B., Vali, M., Meyers, J. and van Wingerden, J. W. (2018). 'A control-oriented dynamic wind farm model: WFSim'. In: *Wind Energy Science* 3(1), pp. 75–95. DOI: 10.5194/wes-3-75-2018.
- Breton, S.-P., Sumner, J., Sørensen, J. N., Hansen, K. S., Sarmast, S. and Ivanell, S. (2017). 'A survey of modelling methods for high-fidelity wind farm simulations using large eddy simulation.' In: *Philosophical transactions. Series A, Mathematical, physical, and engineering sciences* 375 2091.
- Bromm, M. and Kühn, M. (2014). 'Investigation of the interaction between wind turbines and atmospheric flow - Coupling of the aeroelastic code FAST and the LES code PALM.' 10th EAWE PhD Seminar on Wind Energy in Europe. Orléans, France.
- Bromm, M. and Kühn, M. (2017). 'Challenges in recording high quality wake flow measurements of a wind turbine in field experiments.' WindTech2017. Boulder, Colorado, USA.
- Bromm, M., Vollmer, L. and Kühn, M. (2015). 'Numerical investigation of wake development in a stable atmospheric boundary layer.' DEWEK 2015 - 12th German Wind Energy Conference. Bremen, Germany.
- Bromm, M., Rott, A., Beck, H., Vollmer, L., Steinfeld, G. and Kühn, M. (2017a). 'Field investigation on the influence of yaw misalignment and wind veer on the propagation of a wind turbine wake.' Wind Energy Science Conference 2017. Lyngby, Denmark.
- Bromm, M., Rott, A., Beck, H., Vollmer, L., Steinfeld, G. and Kühn, M. (2017b). 'Freifeldversuche zur Nachlaufablenkung'. ForWind Symposium 2017. Oldenburg, Germany.
- Bromm, M., Vollmer, L. and Kühn, M. (2017c). 'Numerical investigation of wind turbine wake development in directionally sheared inflow.' In: *Wind Energy* 20, pp. 381–395. DOI: 10.1002/we.2010.
- Bromm, M., Rott, A., Beck, H., Vollmer, L., Steinfeld, G. and Kühn, M. (2018). 'Field investigation on the influence of yaw misalignment on the propagation of wind turbine wakes.' In: *Wind Energy*, pp. 1–18. DOI: 10.1002/we.2210.
- Calaf, M., Meneveau, C. and Meyers, J. (2010). 'Large eddy simulation study of fully developed wind-turbine array boundary layers.' In: *Physics of Fluids* 22(015110).
- Campagnolo, F., Petrović, V., Schreiber, J., Nanos, E. M., Croce, A. and Bottasso, C. (2016). 'Wind tunnel testing of a closed-loop wake deflection controller for wind

- farm power maximization.' In: *J Phys Conf Ser* 753(032006). DOI: 10.1088/1742-6596/753/3/032006.
- Campbell Scientific, Inc. (2016). *Instruction Manual - EASYFLUX DL*. 8/2016. Available at <https://s.campbellsci.com/documents/eu/manuals/easyflux-dl.pdf>.
- Campbell Scientific, Inc. (2017). *Instruction Manual - IRGASON[®] Integrated CO₂/H₂O Open-Path Gas Analyzer and 3D Sonic Anemometer*. 3/2017. Available at <https://s.campbellsci.com/documents/eu/manuals/irgason.pdf>.
- Christiansen, M. B. and Hasager, C. B. (2005). 'Wake effects of large offshore wind farms identified from satellite SAR'. In: *Remote Sensing of Environment* 98(2), pp. 251–268. DOI: 10.1016/j.rse.2005.07.009.
- Christiansen, M. B. and Hasager, C. B. (2006). 'Using airborne and satellite SAR for wake mapping offshore'. In: *Wind Energy* 9(5), pp. 437–455.
- Churchfield, M., Lee, S., Michalakes, J. and Moriarty, P. (2012). 'A numerical study of the effects of atmospheric and wake turbulence on wind turbine dynamics.' In: *Invited Paper: Journal of Turbulence 2012* 13(14), pp. 1–32.
- Clayton, B. R. and Filby, P. (1982). 'Measurements effects of oblique flows and change in blade pitch angle on performance and wake development of model wind turbines.' In: *Proc. 4th BWEA Wind Energy Conference*. Cranfield Institute of Technology, Cranfield, UK, pp. 469–484.
- Connell, J. R. (1981). *The Spectrum of Wind Speed Fluctuations Encountered by a Rotating Blade of a Wind Energy Conversion System: Observations and Theory*. Abschlussbericht des Verbund-Forschungsprojekts PNL-4083. Richland, Washington, USA: Pacific Northwest Laboratory (PNL).
- Corten, G. P. and Schaak, P. (2003a). 'Heat and Flux'. Pat. WO2004111446.
- Corten, G. P. and Schaak, P. (2003b). 'Heat and Flux: Increase of Wind Farm Production by Reduction of the Axial Induction'. In: *European Wind Energy Conference*. Madrid, Spain.
- Courant, R., Friedrichs, K. and Lewy, H. (1928). 'Über die partiellen Differenzgleichungen der mathematischen Physik'. In: *Mathematische Annalen* 100, pp. 32–74. DOI: 10.1007/BF01448839.
- Crespo, A., Hernández, J. and Frandsen, S. (1999). 'Survey of modelling methods for wind turbine wakes and wind farms.' In: *Wind Energy* 2(1), pp. 1–75.
- Dahlberg, J. R. and Medici, D. (2003). 'Potential improvement of wind turbine array efficiency by active wake control (AWC)'. In: *Proc. European Wind Energy Conference*. Madrid, Spain, pp. 65–84.

- Damiani, R., Dana, S., Annoni, J., Fleming, P., Roadman, J., van Dam, J. and Dykes, K. (2018). 'Assessment of wind turbine component loads under yaw-offset conditions'. In: *Wind Energy Science* 1, pp. 173–189. DOI: 10.5194/wes-3-173-2018.
- Deardorff, J. (1980). 'Stratocumulus-capped mixed layers derived from a three-dimensional model.' In: *Boundary-Layer Meteorology* 18, pp. 495–527.
- Dörenkämper, M., Tambke, J., Steinfeld, G., Heinemann, D. and Kühn, M. (2014). 'Atmospheric Impacts on Power Curves of Multi-Megawatt Offshore Wind Turbines'. In: *Journal of Physics: Conference Series* 555(1), p. 012029.
- Dörenkämper, M., Kühn, M., Hut., V. D. and Emeis, S. (2015a). *An investigation of the atmospheric influence on spatial and temporal power fluctuations in offshore wind farms*. Energy meteorology. Verlag Dr. Hut. ISBN: 9783843923736.
- Dörenkämper, M., Optis, M., Monahan, A. and Steinfeld, G. (2015b). 'On the offshore advection of boundary-layer structures and the influence on offshore wind conditions.' In: *Boundary-Layer Meteorology* 155, pp. 459–482.
- Dörenkämper, M., Witha, B., Steinfeld, G., Heinemann, D. and Kühn, M. (2015c). 'The impact of stable atmospheric boundary layers on wind-turbine wakes within offshore wind farms.' In: *J. Wind Eng. Ind. Aerodyn.* 144(146153). DOI: 10.1016/j.jweia.2014.12.011, 2015b.
- Doubrawa, P., Moriarty, P., Debnath, M., Branlard, E., Herges, T., Naughton, B., Maniaci, D. and Kelley, C. (2018). *The SWiFT Benchmarks*.
- DTU (2018). *Østerild - National test centre for large wind turbines*. Roskilde, Denmark.
- Ennis, B. L. (2017). *SWiFT V27 Wake Steering Loads Analysis*. Tech. rep. SAND2017-0099R. Albuquerque, New Mexico, USA: Sandia National Laboratory (SNL-NM). DOI: 10.2172/1338891.
- Ennis, B. L., White, J. R. and Paquette, J. A. (2018). 'Wind turbine blade load characterization under yaw offset at the SWiFT facility'. In: *Journal of Physics: Conference Series* 1037(5), p. 052001.
- Etling, D. (2008). *Theoretische Meteorologie - Eine Einführung 3rd ed.* Springer: Berlin Heidelberg New York, pp. 325–326.
- Farhat, C., van der Zee, K. G. and Geuzaine, P. (2006). 'Provably second-order time-accurate loosely-coupled solution algorithms for transient nonlinear computational aeroelasticity.' In: *Computer Methods in Applied Mechanics and Engineering* 195, pp. 1973–2001. DOI: 10.1016/j.cma.2004.11.031.
- Felippa, C. A., Park, K. C. and Farhat, C. (2001). 'Partitioned analysis of coupled mechanical systems.' In: *Computer Methods in Applied Mechanics and Engineering* 190(24-25), pp. 3247–3270. DOI: 10.1016/S0045-7825(00)00391-1.

- Fleming, P., Gebraad, P. M. O., Churchfield, M., Lee, S., Johnson, K., Michalakes, J., van Wingerden, J. W. and Moriarty, P. (2013a). *SOWFA + Super Controller Users Manual*. Tech. rep. NREL/TP-5000-59197. Golden, Colorado, USA: National Renewable Energy Laboratory (NREL).
- Fleming, P., Gebraad, P. M. O., Lee, S., van Wingerden, J. W., Johnson, K., Churchfield, M., Michalakes, J., Spalart, P. and Moriarty, P. (2014). 'Evaluating techniques for redirecting turbine wakes using SOWFA'. In: *Renewable Energy* 70, pp. 211–218. DOI: 10.1016/j.renene.2014.02.015.
- Fleming, P., Gebraad, P. M. O., Lee, S., van Wingerden, J. W., Johnson, K., Churchfield, M., Michalakes, J., Spalart, P. and Moriarty, P. (2015). 'Simulation comparison of wake mitigation control strategies for a two-turbine case.' In: *J Phys Conf Ser* 18(12), pp. 2135–2143. DOI: 10.1002/we.1810.
- Fleming, P., Churchfield, M., Scholbrock, A., Clifton, A., Schreck, S., Johnson, K., Wright, A., Gebraad, P., Annoni, J., Naughton, B. and Berg, J. (2016). 'Detailed field test of yaw-based wake steering.' In: *J Phys Conf Ser* 753(052003). DOI: 10.1088/1742-6596/753/5/052003.
- Fleming, P., Annoni, J., Shah, J. J., Wang, L., Ananthan, S., Zhang, Z., Hutchings, K., Wang, P., Chen, W. and Chen, L. (2017a). 'Field test of wake steering at an offshore wind farm.' In: *Wind Energy Science* 2(1), pp. 229–239. DOI: 10.5194/wes-2-229-2017.
- Fleming, P., Annoni, J., Scholbrock, A., Quon, E., Dana, S., Schreck, S., Raach, S., Haizmann, F. and Schlipf, D. (2017b). 'Full-scale field test of wake steering.' In: *J Phys Conf Ser* 854, pp. 173–189. DOI: 10.1088/1742-6596/854/1/012013.
- Fleming, P. M., Gebraad, P. M. O., van Wingerden, J. W., Lee, S. W., Churchfield, M., Scholbrock, A. K., Michalakes, J., Johnson, K. and Moriarty, P. J. (2013b). 'The SOWFA Super-Controller : A High-Fidelity Tool for Evaluating Wind Plant Control Approaches'. In: *Proceedings of the EWEA 2013*. European Wind Energy Association (EWEA), Vienna, Austria.
- Foken, T. (2008). *Micrometeorology*. Springer-Verlag: Berlin Heidelberg, p. 106. DOI: 10.1007/978-3-540-74666-9.
- Frandsen, S. and Thøgersen, M. L. (1999). 'Integrated fatigue loading for wind turbines in wind farms by combining ambient turbulence and wakes.' In: *Wind Engineering* 23(6), pp. 327–339.
- Friedrich, K., Lundquist, J. K., Aitken, M., Kalina, E. A. and Marshall, R. F. (2012). 'Stability and turbulence in the atmospheric boundary layer: A comparison of re-

- mote sensing and tower observations'. In: *Geophysical Research Letters* 39(3). DOI: 10.1029/2011GL050413.
- Froude, R. E. (1889). 'On the part played in propulsion by difference in pressure.' In: *Transaction of the Institute of Naval Architects*, pp. 390–423.
- Gebraad, P. M. O. (2014). 'Data-driven wind plant control.' PhD thesis. Delft University of Technology.
- Gebraad, P. M. O., Teeuwisse, F. W., van Wingerden, J. W., Fleming, P. A., Ruben, S. D., Marden, J. R. and Pao, L. Y (2014). 'A data-driven model for wind plant power optimization by yaw control.' In: *American Control Conference (ACC)*, pp. 3128–3134. DOI: 10.1109/ACC.2014.6859118.
- Gebraad, P. M. O., Teeuwisse, F. W., van Wingerden, J. W., Fleming, P. A., Ruben, S. D., Marden, J. R. and Pao, L. Y (2016). 'Wind plant power optimization through yaw control using a parametric model for wake effects - a CFD simulation study.' In: *Wind Energy* 19(1), pp. 95–114. DOI: 10.1002/we.1822.
- Gebraad, P. M. O., Thomas, J. J., Ning, A., Fleming, P. and Dykes, K. (2017). 'Maximization of the annual energy production of wind power plants by optimization of layout and yaw-based wake control'. In: *Wind Energy* 20(1), pp. 97–107. DOI: 10.1002/we.1993.
- Grant, I. and Parkin, P. (2000). 'A DPIV study of the trailing vortex elements from the blades of a horizontal axis wind turbine in yaw.' In: *Exp Fluids* 28, pp. 368–376.
- Grant, I., Parkin, P. and Wang, X. (1997). 'Optical vortex tracking studies of a horizontal axis wind turbine in yaw using laser-sheet flow visualisation.' In: *Exp Fluids* 23, pp. 513–519.
- Guntur, S., Troldborg, N. and Gaunaa, M. (2012). 'Application of engineering models to predict wake deflection due to a tilted wind turbine.' In: *Proceeding of EWEA 2012 - European Wind Energy Conference & Exhibition*. European Wind Energy Association (EWEA), Copenhagen, Denmark.
- GWEC (2018). *Annual Global Wind Report*. Tech. rep. Brussels, Belgium: Global Wind Energy Council.
- Hansen, K. S., Barthelmie, R. J., Jensen, L. E. and Sommer, A. (2012). 'The impact of turbulence intensity and atmospheric stability on power deficits due to wind turbine wakes at Horns Rev wind farm'. In: *Wind Energy* 15(1), pp. 183–196. DOI: 10.1002/we.512.
- Hardesty, R. M. and Weber, B. F. (1987). 'Lidar Measurement of Turbulence Encountered by Horizontal-Axis Wind Turbines'. In: *Journal of Atmospheric and Oceanic Tech-*

- nology* 4(1), pp. 191–203. DOI: 10.1175/1520-0426(1987)004<0191:LMOTEB>2.0.CO;2.
- Hertwig, D. (2013). ‘On Aspects of Large-Eddy Simulation Validation for Near-Surface Atmospheric Flows’. PhD thesis. University of Hamburg.
- Hirth, B. D., Schroeder, J. L., Gunter, W. S. and Guynes, J. G. (2012). ‘Measuring a Utility-Scale Turbine Wake Using the TTUKa Mobile Research Radars’. In: *Journal of Atmospheric and Oceanic Technology* 29(6), pp. 765–771. DOI: 10.1175/JTECH-D-12-00039.1.
- Hirth, B. D., Schroeder, J. L., Gunter, W. S. and Guynes, J. G. (2014). ‘Coupling Doppler radar-derived wind maps with operational turbine data to document wind farm complex flows’. In: *Wind Energy* 18(3), pp. 529–540. DOI: 10.1002/we.1701.
- Hirth, B. D., Schroeder, J. L., Irons, Z. and Walter, K. (2015). ‘Dual-Doppler measurements of a wind ramp event at an Oklahoma wind plant’. In: *Wind Energy* 19(5), pp. 953–962. DOI: 10.1002/we.1867.
- IEC (2005). *Wind turbines - Part 1: Design Requirements*. Tech. rep. IEC-61400-1:2015, 3rd ed. Geneva, Switzerland, International Electrotechnical Commission.
- IEC (2015). *Wind turbines - Part 13: Measurement of mechanical loads*. Tech. rep. IEC 61400-13-1:2015. Geneva, Switzerland: International Electrotechnical Commission.
- IEC (2017). *Wind turbines - Part 12-1: Power Performance Measurement of Electricity Producing Wind Turbines*. Tech. rep. IEC 61400-12-1:2017. Geneva, Switzerland: International Electrotechnical Commission.
- IEEE Acoustics, Speech, and Signal Processing Society. Digital Signal Processing Committee (1979). *Programs for Digital Signal Processing*. New York: IEEE Press.
- Iungo, G. and Porté-Agel, F. (2014). ‘Volumetric lidar scanning of wind turbine wakes under convective and neutral atmospheric stability regimes.’ In: *J Atmos Oceanic Tech* 31, pp. 2035–2048. DOI: 10.1175/JTECH-D-13-00252.1.
- Jiménez, A., Crespo, A., Migoya, E. and Garcia, J. (2007). ‘Advances in large-eddy simulation of a wind turbine wake.’ In: *Journal of Physics: Conference Series* 75(012041).
- Jiménez, A., Crespo, A., Migoya, E. and Garcia, J. (2008). ‘Large-eddy simulation of spectral coherence in a wind turbine wake’. In: *Environmental Research Letters* 3(1), p. 015004. DOI: 10.1088/1748-9326/3/1/015004.
- Jiménez, A., Crespo, A. and Migoya, E. (2010). ‘Application of a LES technique to characterize the wake deflection of a wind turbine in yaw.’ In: *Wind Energy* 13, pp. 559–572.
- Jonkman, B. J. (2009). *TurbSim User’s Guide*. Tech. rep. NREL/TP-500-38060. Golden, Colorado, USA: National Renewable Energy Laboratory (NREL).

- Jonkman, J., Butterfield, S., Musial, W. and Scott, G. (2009). *Definition of a 5-MW reference wind turbine for offshore system development*. Tech. rep. NREL/TP-500-46198. Golden, Colorado, USA: National Renewable Energy Laboratory (NREL).
- Jonkman, J. M. and Buhl, Jr., M. L. (2005). *FAST User's Guide*. Tech. rep. NREL/EL-500-38230. Golden, Colorado, USA: National Renewable Energy Laboratory (NREL).
- Kaimal, J. C., Wyngaard, J. C., Izumi, Y. and Coté, O. R. (1972). 'Spectral characteristics of surface-layer turbulence.' In: *Q. J. R. Meteorol. Soc.* 98, pp. 563–589.
- Kapp, S. and Kühn, M. (2014). 'A five-parameter wind field estimation method based on spherical upwind LiDAR measurements.' In: *J Phys Conf Ser* 555(012112). DOI: 10.1088/1742-6596/555/1/012112.
- Käsler, Y., Rahm, S., Simmet, R. and Kühn, M. (2010). 'Wake Measurements of a Multi-MW Wind Turbine with Coherent Long-Range Pulsed Doppler Wind Lidar'. In: *Journal of Atmospheric and Oceanic Technology* 27(9), pp. 1529–1532. DOI: 10.1175/2010JTECHA1483.1.
- Lee, S., Churchfield, M., Moriarty, P. and Michalakes, J. (2012). 'Atmospheric and Wake Turbulence Impacts on Wind Turbine Fatigue Loadings'. In: *Proceedings of 50th AIAA Aerospace Sciences Meeting*. Nashville, Tennessee, USA. DOI: 10.2514/6.2012-540.
- Lu, H. and Porté-Agel, F. (2011). 'Large-eddy simulation of a very large wind farm in a stable atmospheric boundary layer.' In: *Phys Fluids* 23(065101). DOI: 10.1063/1.3589857.
- Lund, T. S., Wu, X. and Squires, K. D. (1998). 'Generation of turbulent inflow data for spatially-developing boundary layer simulations.' In: *Journal of Computational Physics* 140(2), pp. 233–258. DOI: 10.1006/jcph.1998.5882.
- Lundquist, J., Churchfield, M., Lee, S. and Clifton, A. (2015). 'Quantifying error of lidar and sodar Doppler beam swinging measurements of wind turbine wakes using computational fluid dynamics.' In: *Atmos Meas Tech* 8, pp. 907–920. DOI: 10.5194/amt-8-907-2015.
- Machefaux, E., Larsen, G. C., Koblitz, T., Troldborg, N., Kelly, M. C., Chougule, A., Hansen, K. S. and Rodrigo, J. S. (2016). 'An experimental and numerical study of the atmospheric stability impact on wind turbine wakes.' In: *Wind Energy* 19, pp. 1785–1805. DOI: 10.1002/we.1950.
- Machielse, L. A. H., Barth, S., Bot, E. T. G., Hendriks, H. B. and Schepers, G. J. (2008). *Evaluation of "Heat and Flux" Farm Control*. Tech. rep. ECN-E-07-105. Energy research Centre of the Netherlands (ECN).

- Magnusson, M. and Smedman, A. S. (1994). 'Influence of Atmospheric Stability on Wind Turbine Wakes'. In: *Wind Engineering* 18(3), pp. 139–152.
- Mann, J., Cariou, J.-P., Courtney, M. S., Parmentier, R., Mikkelsen, T., Wagner, R., Lindelöw, P., Sjöholm, M. and Enevoldsen, K. (2008). 'Comparison of 3D turbulence measurements using three staring wind lidars and a sonic anemometer'. In: *IOP Conference Series: Earth and Environmental Science* 1(1), p. 012012.
- Marathe, N., Swift, A., Hirth, B., Walker, R. and Schroeder, J. (2015). 'Characterizing power performance and wake of a wind turbine under yaw and blade pitch'. In: *Wind Energy* 19(5), pp. 963–978. DOI: 10.1002/we.1875.
- Maronga, B., Gryschka, M., Heinze, R., Hoffmann, F., Kanani-Sühring, F., Keck, M., Ketelsen, K., Letzel, M. O., Sühring, M. and Raasch, S. (2015). 'The Parallelized large-eddy simulation model (PALM) version 4.0 for atmospheric and oceanic flows: model formulation, recent developments and future perspectives.' In: *Geoscientific Model Development Discussions* 8, pp. 1539–1637.
- Martínez-Tossas, L. A., Churchfield, M. J. and Leonardi, S. (2015). 'Large eddy simulations of the flow past wind turbines: actuator line and disk modeling'. In: *Wind Energy* 18(6), pp. 1047–1060. DOI: 10.1002/we.1747.
- Martínez-Tossas, L. A., Churchfield, M. J., Yilmaz, A. E., Sarlak, H., Johnson, P. L., Sørensen, J. N., Meyers, J. and Meneveau, C. (2018). 'Comparison of four large-eddy simulation research codes and effects of model coefficient and inflow turbulence in actuator-line-based wind turbine modeling'. In: *Journal of Renewable and Sustainable Energy* 10(3), p. 033301. DOI: 10.1063/1.5004710.
- Mehta, D., van Zuijlen, A. H., Koren, B., Holierhoek, J. G. and Bijl, H. (2014). 'Large Eddy Simulation of wind farm aerodynamics: A review'. In: *Journal of Wind Engineering and Industrial Aerodynamics* 133, pp. 1–17. DOI: 10.1016/j.jweia.2014.07.002.
- Mikkelsen, R. F. and Sørensen, J. N. (Jan. 2004). 'Actuator Disc Methods Applied to Wind Turbines'. English. PhD thesis.
- Mikkelsen, T., Angelou, N., Hansen, K., Sjöholm, M., Harris, M., Slinger, C., Hadley, P., Scullion, R., Ellis, G. and Vives, G. (2013). 'A spinner-integrated wind lidar for enhanced wind turbine control.' In: *Wind Energy* 16, pp. 625–643.
- Mirocha, J. D., Rajewski, D. A., Marjanovic, N., Lundquist, J. K., Kosović, B., Draxl, C. and Churchfield, M. J. (2015). 'Investigating wind turbine impacts on near-wake flow using profiling lidar data and large-eddy simulations with an actuator disk model'. In: *J. Renewable Sustainable Energy* 7(043143). DOI: 10.1063/1.4928873.

- Mittelmeier, N. and Kühn, M. (2018). 'Determination of optimal wind turbine alignment into the wind and detection of alignment changes with SCADA data'. In: *Wind Energy Science* 3(1), 395—408. DOI: 10.5194/wes-3-395-2018.
- Monin, A. and Obukhov, A. (1954). 'Osnovnye zakonomernosti turbulentnogo peremeshivaniya v prizemnom sloe atmosfery (basic laws of turbulent mixing in the atmosphere near the ground).' In: *Tr. Akad. Nauk SSSR Geophys. Inst.* 24, pp. 163–187.
- Naughton, B. (2017). *Scaled Wind Farm Technology (SWiFT) Facility Wake Steering Experiment Instrumentation and Data Processing*. Tech. rep. SAND2017-3252 O. Lubbock, Texas, USA: Sandia National Laboratories - SWiFT facility.
- NREL (2015). *Field Testing Research at the NWTC*. Tech. rep. NREL/FS-5000-63355. Golden, Colorado, USA: National Renewable Energy Laboratory (NREL).
- Nygaard, N. G. and Newcombe, A. C. (2018). 'Wake behind an offshore wind farm observed with dual-Doppler radars'. In: *Journal of Physics: Conference Series* 1037(7), p. 072008.
- Obukhov, A. M. (1971). 'Turbulence in an atmosphere with a non-uniform temperature.' In: *Boundary-Layer Meteorol* 2, pp. 7–29. DOI: 10.1007/BF00718085.
- Parkin, P., Holm, R. and Medici, D. (2001). 'The application of PIV to the wake of a wind turbine in yaw.' In: *Proceedings of the 4th International Symposium on Particle Image Velocimetry*. Göttingen, Germany, pp. 155–162.
- Porté-Agel, F., Wu, Y.-T., Lu, H. and Conzemius, R. J. (2011). 'Large-Eddy simulation of atmospheric boundary layer flow through wind turbines and wind farms.' In: *Journal of Wind Engineering and Industrial Aerodynamics* 99, pp. 154–168.
- Porté-Agel, F., Wu, Y.-T. and Chen, C.-H. (2013). 'A Numerical Study of the Effects of Wind Direction on Turbine Wakes and Power Losses in a Large Wind Farm.' In: *Energies* 6, pp. 5297–5313.
- Raasch, S. and Schröter, M. (2011). 'PALM - A large-eddy simulation model performing on massively parallel computers.' In: *Meteorologische Zeitschrift* 10, pp. 363–372.
- Rebmann, C., Kolke, O., Heinesch, B., Queck, R., Ibrom, A. and Aubinet, M. (2012). 'Data Acquisition and Flux Calculations'. In: *Eddy Covariance*. Ed. by M. Aubinet, T. Vesala and D Papale. Springer, Dordrecht, pp. 59–83. DOI: 10.1007/978-94-007-2351-1_3.
- Roache, P. J. (1985). *Computational fluid dynamics*. Albuquerque, New Mexico, USA: Hermosa Publishers, p. 446.
- Rott, A., Doekemeijer, B., Seifert, J., van Wingerden, J. W. and Kühn, M. (2017). 'Accounting for wind direction variability and uncertainty by robust active wake de-

- flection control in wind farms'. In: *Proc. WindTech - International Conference on Future Technologies in Wind Energy*. Boulder, Colorado, USA.
- Rott, A., Doekemeijer, B., Seifert, J., van Wingerden, J. W. and Kühn, M. (2018). 'Robust active wake control in consideration of wind direction variability and uncertainty'. In: *Wind Energy Science*. DOI: 10.5194/wes-2018-50.
- Sanderse, B. (2009). *Aerodynamics of wind turbine wakes*. Tech. rep. ECN-E-09-016. Petten, North Holland, Netherlands: Energy research Centre of the Netherlands (ECN).
- Sathe, A., Mann, J., Gottschall, J. and Courtney, M. S. (2011). 'Can Wind Lidars Measure Turbulence?' In: *Journal of Atmospheric and Oceanic Technology* 28(7), pp. 853–868. DOI: 10.1175/JTECH-D-10-05004.1.
- Schlipf, D., Trabucchi, D., Bischoff, O., Hofsäß, M., Mann, J., Mikkelsen, T., Rettenmeier, A., Trujillo, J. J. and Kühn, M. (2010). 'Testing of Frozen Turbulence Hypothesis for Wind Turbine Applications with a Scanning LIDAR System'. In: *15th International Symposium for the Advancement of Boundary Layer Remote Sensing (ISARS)*. DOI: 10.18419/opus-3915.
- Schlipf, D., Schlipf, D. J. and Kühn, M. (2013). 'Nonlinear model predictive control of wind turbines using LIDAR.' In: *Wind Energy* 16, pp. 1107–1129. DOI: 10.1002/we.1533.
- Sim, C., Basu, S. and Manuel, L. (2012). 'On Space-Time Resolution of Inflow Representations for Wind Turbine Loads Analysis'. In: *Energies* 5(7), pp. 2071–2092. DOI: 10.3390/en5072071.
- Sørensen, J. N. and Kock, C. W. (1995). 'A model for unsteady rotor aerodynamics'. In: *Journal of Wind Engineering and Industrial Aerodynamics* 58(3), pp. 259–275. DOI: 10.1016/0167-6105(95)00027-5.
- Sørensen, J. N. and Shen, W. Z. (2002). 'Numerical modelling of wind turbine wakes.' In: *Journal of Fluids Engineering* 124(2), pp. 393–399.
- Sørensen, J. N., Shen, W. Z. and Munduate, X. (1998). 'Analysis of wake-states by a full-field actuator disc model.' In: *Wind Energy* 1, pp. 73–88.
- Stevens, R. J.A. M., Martínez-Tossas, L. A. and Meneveau, C. (2018). 'Comparison of wind farm large eddy simulations using actuator disk and actuator line models with wind tunnel experiments'. In: *Renewable Energy* 116, pp. 470–478. DOI: 10.1016/j.renene.2017.08.072.
- Storey, R. C., Norris, S. E., Stol, K. A. and Cater, J. E. (2013). 'Large eddy simulation of dynamically controlled wind turbines in an offshore environment'. In: *Wind Energy* 16(6), pp. 845–864. DOI: 10.1002/we.1525.

- Storey, R. C., E., N. S. and Cater, J. E. (2015). 'An actuator sector method for efficient transient wind turbine simulation.' In: *Wind Energy* 18, pp. 699–711. DOI: 10.1002/we.1722.
- Sturge, D., Sobotta, D., Howell, R., While, A. and Lou, J. (2015). 'A hybrid actuator disc - Full rotor CFD methodology for modelling the effects of wind turbine wake interactions on performance.' In: *Renewable Energy* 80, pp. 525–537. DOI: 10.1016/j.renene.2015.02.053.
- Thomson, D. J. (1982). 'Spectrum estimation and harmonic analysis'. In: *Proceedings of the IEEE* 70(9), pp. 1055–1096. DOI: 10.1109/PROC.1982.12433.
- Trabucchi, D., Trujillo, J. J., Schneemann, J., Bitter, M. and Kühn, M. (2015). 'Application of staring lidars to study the dynamics of wind turbine wakes.' In: *Meteorologische Zeitschrift* 24(6), pp. 557–564. DOI: 10.1127/metz/2014/0610.
- Troldborg, N., Sørensen, J. N. and Mikkelsen, R. (2007). 'Actuator line simulation of wake of wind turbine operating in turbulent inflow.' In: *Journal of Physics: Conference Series* 75(012063).
- Troldborg, N., Larsen, G. C., Madsen, H. A., Hansen, K. S., Sørensen, J. N. and Mikkelsen, R. (2011). 'Numerical simulations of wake interaction between two wind turbines at various inflow conditions'. In: *Wind Energy* 14(7), pp. 859–876. DOI: 10.1002/we.433.
- Troldborg, N., Zahle, F., Réthoré, P.-E. and Sørensen, N. N. (2015). 'Comparison of wind turbine wake properties in non-sheared inflow predicted by different computational fluid dynamics rotor models'. In: *Wind Energy* 18(7), pp. 1239–1250. DOI: 10.1002/we.1757.
- Trujillo, J. J. (2018). 'Large scale dynamics of wind turbine wakes - Measurement and modelling in the full field'. PhD thesis. ForWind - University of Oldenburg.
- Trujillo, J. J., Seifert, J. K., Würth, I., Schlipf, D. and Kühn, M. (2016). 'Full-field assessment of wind turbine near-wake deviation in relation to yaw misalignment.' In: *Wind Energy* 1, pp. 41–53. DOI: 10.5194/wes-1-41-2016.
- Vasiljević, N., Palma, L. M., Angelou, J. M., Carlos Matos, N., Menke, R., Lea, G., Mann, J., Courtney, M., Frölen Ribeiro, L. and M. G. C. Gomes, V. M. (2017). 'Perdigão 2015: methodology for atmospheric multi-Doppler lidar experiments'. In: *Atmospheric Measurement Techniques* 10(9), pp. 3463–3483. DOI: 10.5194/amt-10-3463-2017.
- Verbruggen, T. W. (2009). *Load monitoring for wind turbines; Fibre optic sensing and data processing*. Tech. rep. ECN-E-09-071. Petten, North Holland, Netherlands: Energy research Centre of the Netherlands (ECN).

- Vermeer, L., Sørensen, J. and Crespo, A. (2003). 'Wind turbine wake aerodynamics'. In: *Prog Aerosp Sci* 39, pp. 467–510.
- Vijayakumar, G., Brasseur, J. G., Lavelly, A., Jayaraman, B. and Craven, B. C. (2016). 'Interaction of atmospheric turbulence with blade boundary layer dynamics on a 5MW wind turbine using blade-boundary-layer-resolved CFD with hybrid URANS-LES.' In: *34th Wind Energy Symposium AIAA SciTech*. San Diego, California, USA. DOI: 10.2514/6.2016-0521.
- Vollmer, L., Steinfeld, G., Heinemann, D. and Kühn, M. (2016). 'Estimating the wake deflection downstream of a wind turbine in different atmospheric stabilities: an LES study'. In: *Wind Energy Science* 1, pp. 129–141. DOI: 10.5194/wes-1-129-2016.
- Wagenaar, J. W. and Schepers, J. G. (2012). 'Wake Measurements in ECN's Scaled Wind Farm'. In: *Journal of Physics: Conference Series* 555(1), p. 012105.
- Weitkamp, C. (2005). *Doppler wind lidar-range-resolved optical remote sensing of the atmosphere*. Springer: Singapore, 354p. DOI: 10.1007/b106786.
- Wharton, S. and Lundquist, J. K. (2010). *Atmospheric stability impacts on power curves of tall wind turbines - an analysis of a West Coast North American wind farm*. Tech. rep. LLNL-TR-424425. Livermore, California, USA: Lawrence Livermore National Laboratory (LLNL).
- Wicker, L. and Skamarock, W. (2002). 'Time-splitting methods for elastic models using forward time schemes.' In: *Monthly Weather Review* 130, pp. 2088–2097.
- Wilczak, J. M., Onley, S. P. and Stage, S. A. (2001). 'Sonic anemometer tilt correction algorithms.' In: *Bound-Layer Meteorol* 99, pp. 127–150. DOI: 10.1023/A:1018966204465.
- Witha, B., Steinfeld, G. and Heinemann, D. (2014a). 'High-resolution offshore wake simulations with the LES model PALM, wind energy-impact of turbulence.' In: *Wind Energy - Impact of Turbulence. Research Topics in Wind Energy, Vol 2*. Ed. by M. Hölling, J. Peinke and S Ivanell. Springer, Berlin, Heidelberg, pp. 175–181. DOI: 10.1007/978-3-642-54696-9_26.
- Witha, B., Steinfeld, G., Dörenkämper, M. and Heinemann, D. (2014b). 'Large-eddy simulation of multiple wakes in offshore wind farms.' In: *Journal of Physics: Conference Series* 555(012108). DOI: 10.1088/1742-6596/555/1/012108.
- World Meteorological Organization (2008). *WMO Guide to Meteorological Instruments and Methods of Observation. - WMO No. 8 (7th edition 2008)*. Tech. rep. Geneva, Switzerland: World Meteorological Organization.

- Wu, Y.-T. and Porté-Agel, F. (2011). 'Large-Eddy Simulation of Wind-Turbine Wakes: Evaluation of Turbine Parametrisations'. In: *Boundary-Layer Meteorology* 138(3), pp. 345–366. DOI: 10.1007/s10546-010-9569-x.
- Yilmaz, A. E. and Meyers, J. (2018). 'Optimal dynamic induction control of a pair of inline wind turbines'. In: *Physics of Fluids* 30(8), p. 085106. DOI: 10.1063/1.5038600.
- Zahle, F., Sørensen, N. and Aagaard, H. M. (2008). *The influence of wind shear and tower presence on rotor and wake aerodynamics using CFD*. Tech. rep. Risø-R-1649(EN). Roskilde, Denmark: Risø DTU - National Laboratory for Sustainable Energy.

List of publications

Journal peer-reviewed publications on which this thesis is based

- Bromm, M., Vollmer, L. and Kühn, M. (2017c). 'Numerical investigation of wind turbine wake development in directionally sheared inflow.' In: *Wind Energy* 20, pp. 381–395. DOI: 10.1002/we.2010

M. Bromm performed the simulations, carried out the scientific analysis and wrote the manuscript. L. Vollmer provided the large-eddy wind fields. M. Kühn had a supervising function. The article is included as Chapter 4 in this thesis.

- Bromm, M., Rott, A., Beck, H., Vollmer, L., Steinfeld, G. and Kühn, M. (2018). 'Field investigation on the influence of yaw misalignment on the propagation of wind turbine wakes.' In: *Wind Energy*, pp. 1–18. DOI: 10.1002/we.2210

M. Bromm coordinated and supervised the measurement campaign, carried out the scientific analysis and wrote the manuscript. A. Rott supported the analysis and validation of the measurement data. H. Beck processed the lidar data and provided the 10-minute-averaged wake scans. L. Vollmer and G. Steinfeld supervised the atmospheric measurements and provided the Obukhov length. Furthermore, G. Steinfeld and M. Kühn had a supervising function. The article is included as Chapter 2 in this thesis.

Conference presentations

- Bromm, M. and Kühn, M. (2014). 'Investigation of the interaction between wind turbines and atmospheric flow - Coupling of the aeroelastic code FAST and the LES code PALM.'. 10th EAWC PhD Seminar on Wind Energy in Europe. Orléans, France (poster presentation)
- Bromm, M., Vollmer, L. and Kühn, M. (2015). 'Numerical investigation of wake development in a stable atmospheric boundary layer.' DEWEK 2015 - 12th German Wind Energy Conference. Bremen, Germany (oral presentation)
- Bromm, M., Rott, A., Beck, H., Vollmer, L., Steinfeld, G. and Kühn, M. (2017a). 'Field investigation on the influence of yaw misalignment and wind veer on the propagation of a wind turbine wake.' Wind Energy Science Conference 2017. Lyngby, Denmark (oral presentation)

- Bromm, M. and Kühn, M. (2017). 'Challenges in recording high quality wake flow measurements of a wind turbine in field experiments.' WindTech2017. Boulder, Colorado, USA (oral presentation)
- Bromm, M., Rott, A., Beck, H., Vollmer, L., Steinfeld, G. and Kühn, M. (2017b). 'Freifeldversuche zur Nachlaufablenkung'. ForWind Symposium 2017. Oldenburg, Germany (oral presentation)

Additional publication

- Ahrens, R., Bockholt, S., Bottasso, C. L., Bromm, M., Campagnolo, F., Heinemann, D., Voß, S. and Kühn, M. (2016). *Erhöhung des Flächenenergieertrags in Windparks durch avancierte Anlagen- und Parkregelung (CompactWind)*. Abschlussbericht des Verbund-Forschungsprojekts. Renningen: Robert Bosch GmbH, Zentralbereich Forschung und Vorausentwicklung (CR/AEI). DOI: 10.2314/gbv:894297163

Acknowledgements

First of all, I would like to express my sincere gratitude to my supervisor Prof. Dr. Martin Kühn for giving me the opportunity to pursue my PhD studies in his research group Wind Energy Systems of ForWind - University of Oldenburg. Moreover, I would like to thank him for the excellent opportunities and resources, which allowed me to address innovative research questions.

I also express particular gratitude to Dr. Gerald Steinfeld of the Energy Meteorology group of ForWind Oldenburg for his support throughout my PhD and his always extensive, detailed, substantiated and valuable feedback. Thank you very much!

I thank Prof. Lucy Y. Pao, Ph.D., of the University of Colorado Boulder who accepted to review my thesis and to be part of the examination committee. Further thanks goes to Prof. Dr. Alexander K. Hartmann of the University of Oldenburg who was the third member of the examination committee.

My sincere thanks also goes to all my colleagues of the Wind Energy Systems group and the members of ForWind Oldenburg for fruitful discussions, outstanding Kohlfahrten, interesting conference visits and a very pleasant time throughout my time in Oldenburg.

In particular, I am grateful to my colleagues Frederik Berger, Stephan Voß and Andreas Rott. I thank Frederik because as the wind tunnel specialist in our team he was able to enlighten me with his expertise and experience from a research field that I have carelessly ignored with my focus being on simulations and field experiments. Apart from his scientific expertise, his ribs and pulled pork preparation skills need to be highlighted!

I am grateful to Stephan who always ensured a smooth operation of even the most complex and daring field campaigns. In addition, he is a renowned Simpsons expert and often his contributions were all that was needed to save my day. I would even join you for another Brusow campaign!

Andreas is simply the best colleagues you can imagine. I even slowed down the progress on my PhD by 3-4 years just for sharing an office with him for some extra

time! Unfortunately, eventually I had to turn my thesis in and now it is time for you Andreas to get going as well! Just do it. You earned it.

Furthermore, I thank Kathleen Poland for her commitment in the field of teaching by taking care of all organisational matters and allowing us research assistants to concentrate on the content-related work with the students. I thank Dr. Lukas Vollmer for fulfilling my demands for even the most specific large-eddy wind fields. Additionally, I would like to thank the two old wise men Dr. Luis Vera-Tudela and Bernd Kuhnle. Both were already part of the group when I joined and were always ready to share their experiences.

In addition to my time at university, I must have spent 20+ hours per day climbing at local gyms or outdoors. Climbing is such a big part of my life and I would like to thank everyone who shared this passion with me in the last years, especially mentioning Rüdiger, Sascha, Janina, Simon, Nick, Maddin, Mareike, Matthias, Andreas, Andi and Björn. Get ready for even more intense sessions now that I have all that extra time! Last but not least, I thank all the funding organisations and project partners that supported my work. The work presented in this thesis was only possible due to the funding of the national research projects 'CompactWind' (FKZ 0325492B - German Federal Ministry for Economic Affairs and Energy (BMWi)), 'DFWind - Phase 1', (FKZ 0325936C - German Federal Ministry for Economic Affairs and Energy (BMWi)), 'WIMS-CLuster' (FKZ 0324005 - German Federal Ministry for Economic Affairs and Energy (BMWi)), 'ventus efficiens' (ZN3092 - 'Niedersächsisches Vorab', Ministry for Science and Culture of Lower Saxony) and ForWind - Carl von Ossietzky University Oldenburg.

My thanks also go out to the Robert Bosch GmbH and the eno energy systems GmbH, our two partners from industry and the Technical University of Munich, our academic partner in the 'CompactWind' research project. I greatly appreciate the support received by all involved. In particular, I would like to thank Stefan Bockholt and Robin Ahrens from eno for their commitment and for granting us access to utility-scale wind turbines, which allowed us to perform so far unique experiments.

Computer resources for the computationally demanding large-eddy simulations have been provided by the North German Supercomputing Alliance (HLRN) and the HPC Cluster FLOW (Facility for Large-Scale Computations in Wind Energy Research), located at the University of Oldenburg, and funded by the Federal Ministry for the Environment, Nature Conservation and Nuclear Safety (BMU) under grant number 0325220. In addition, two conference visits were promoted by the German Academic Exchange Service and funded by the Federal Ministry of Education and Research.

Curriculum vitae

Personal:

Name Marc Bromm
Place of birth Cottbus, Germany

Education:

08/2011 – 12/2012 M.Sc. Mechanical Engineering (Energy Technology) at the Brandenburg University of Technology, Cottbus, Germany

Master thesis: 'Validation and further development of the coupling of FLEX5 with ANSYS AQWA for the simulation of floating wind turbines' (REpower Systems SE)

09/2011 – 01/2012 Studying abroad, Santa Clara University, Santa Clara, California, USA

10/2007 – 07/2011 B.Sc. Mechanical Engineering (Energy-Installation-Construction) at the Brandenburg University of Technology, Cottbus, Germany

Bachelor thesis: 'Optimisation and validation of a wake model for wind turbines based on measurement in a wind farm' (REpower Systems SE)

Experience:

10/2018 – Current Graduate Trainee, Research & Security Center EMEA at ASSA ABLOY Deutschland GmbH

04/2013 – 06/2018 Researcher at ForWind - University of Oldenburg

Eidesstattliche Erklärung

Hiermit versichere ich, die vorliegende Arbeit selbstständig verfasst, keine anderen als die angegebenen Quellen und Hilfsmittel verwendet und die Leitlinien guter wissenschaftlicher Praxis der Carl von Ossietzky Universität Oldenburg befolgt zu haben.

Die Arbeit hat weder in ihrer Gesamtheit noch in Teilen einer anderen Hochschule zur Begutachtung in einem Promotionsverfahren vorgelegen und im Zusammenhang mit dem Promotionsvorhaben wurden keine kommerziellen Vermittlungs- oder Beratungsdienste in Anspruch genommen.

Teile der Arbeit sind bereits veröffentlicht.

Oldenburg, den 10.05.2019

.....
Marc Bromm

